DRA

(NASA-CR-157630) PLANETARY ASTRONOMY PROGRAM Final Report, 26 Oct. 1977 - 25 Oct. 1978 (Planetary Science Inst., Tucson, Ariz.) 146 p HC A07/MF A01 CSCL 03A

N79-13958

Unclas
G3/89 15311

PLANETARY SCIENCE INSTITUTE

NASW-3134

PLANETARY ASTRONOMY PROGRAM

FINAL REPORT

OCTOBER 1978

Submitted by
The Planetary Science Institute
2030 East Speedway, Suite 201
Tucson, Arizona 85719

TASK 1: OBSERVATIONS AND ANALYSES OF ASTEROIDS, TROJANS AND COMETARY NUCLEI

Task 1.1: Spectrophotometric Observations and Analysis of Asteroids and Cometary Nuclei

Principal Investigator: Clark R. Chapman
Co-Investigator: William K. Hartmann

Spectrophotometric Observations of Asteroids.

Successful observations were obtained in one autumn observing run and in one spring observing run. They have been described in earlier quarterly reports. The reduced data are discussed below.

Spectrophotometry of the Nucleus of Comet P/Arend-Rigaux.

Successful observations were obtained during the autumn 1977 observing run, as described in an earlier quarterly report. Unfortunately, visual inspection revealed that the comet was active and not simply a stellar nucleus as had been hoped. The data have now been reduced in preliminary form and the resulting spectral reflectance curve is exhibited as Figure 1. There is evidence of emission in some appropriate bands; the reflected sunlight dominates the spectrum, but it has not yet been interpreted.

Interpretive Analyses of Asteroid Spectrophotometry

Figures 2 and 3 represent the first attempt at synthesizing

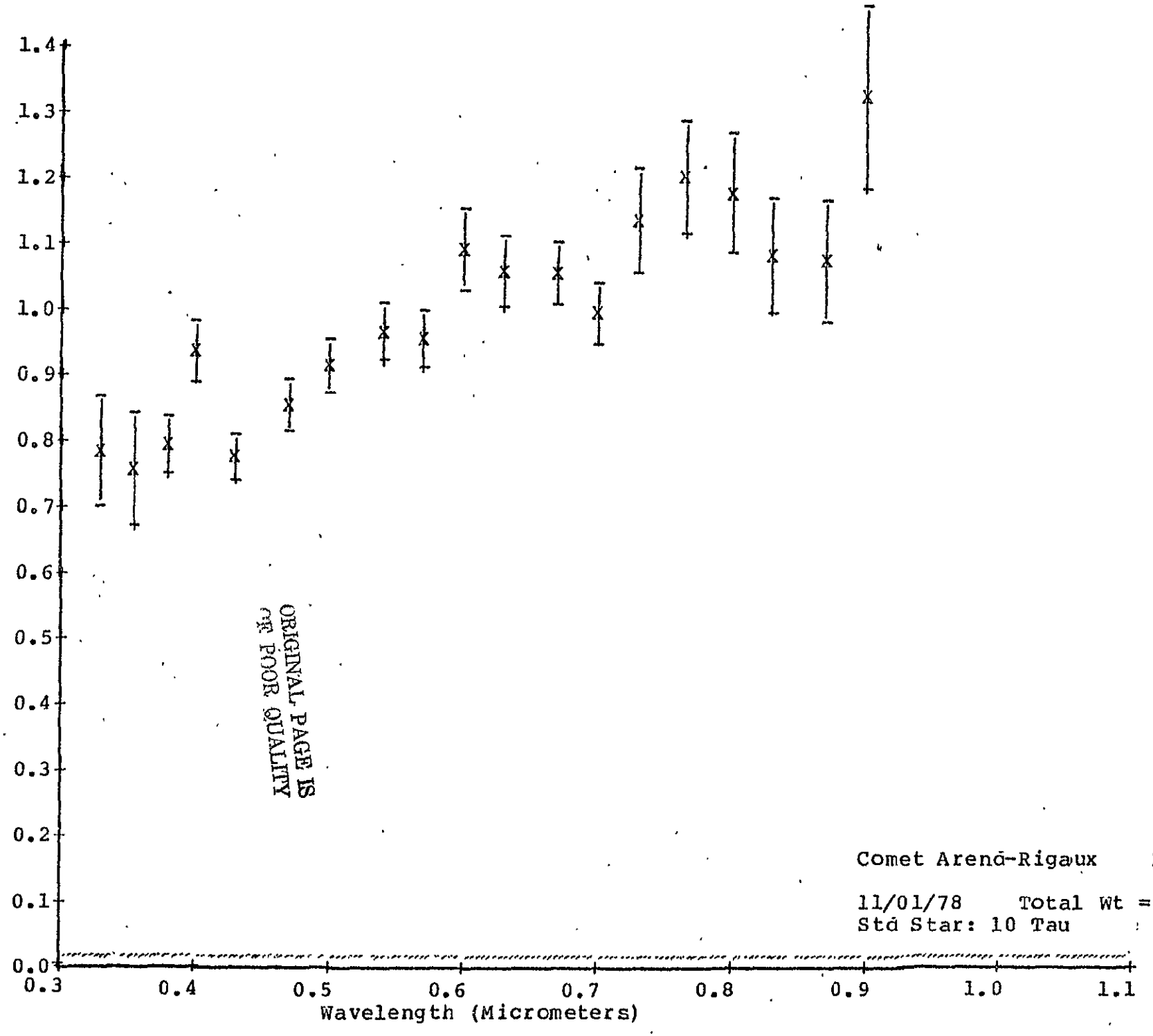

FIGURE 1

FIGURE 2

ORIGINAL PAGE IS
OF POOR QUALITY

FIGURE 3

the 150 new asteroid spectra. Figure 2 shows the spectra plotted as a function of semi-major axis and eccentricity, revealing important variations - especially with a - in the traits of the spectra. Trojans and other asteroids at great solar distances show a variety of spectra, many of them quite red despite the low measured albedoes for many of these asteroids. Figure 3 illustrates many of the asteroid spectra grouped according to diameter and taxonomic class, as reported in Bowell et al. (1978). The latter paper, written during the present contract year, is also a major interpretive effort and is here included as Appendix I.

Preliminary Reduction of Past Data

Besides the 98 spectra published previously by Chapman, McCord, and their associates, new data have been obtained for nearly 200 additional asteroids. To date, data have been reduced for approximately 150 of the new asteroids, plus supplementary data on some of the asteroids previously published. Best available average spectra for all 250 asteroids are here included as Appendix II.

The availability of these spectra marks a major advance in available asteroid data, based on observations spanning four years. The remaining fifty asteroids will be reduced by the end of the year and will be make available in the TRIAD data file. Major interpretive efforts based on this data base will be done for presentation at the Tucson Asteroid Conference

being organized by T. Gehrels for March 1979.

Continued Study of Hektor and the Trojan Asteroids

The publication resulting from our Hektor observations and analyses, "The Nature of Trojan Asteroid Hektor," will be in the journal, Icarus. The galleys arrived in early November (see Appendix III). Shortly after the closing of the contract period, Dr. Hartmann gave a verbal presentation of the results at the annual DPS meeting (Division of Planetary Science of the American Astronomical Society), November 3, 1978.

Dr. Hartmann and Dr. Cruikshank are planning future observations of Hektor in Spring, 1979, to test further the model developed from the work accomplished during this contract period.

Task 1.2: Search for Further Asteroid Close Encounters Suitable for Mass Determination

Principal Investigator: Donald R. Davis

The objective of this task is to search for close encounters between one of the ten largest asteroids and another of the numbered asteroids that would produce observable perturbations in the smaller asteroid's orbit. Analysis of observation would determine whether or not it would be feasible to measure the mass of the perturbing asteroid. Observations of perturbations in asteroid orbits resulting from close encounters or near-commensurabilities in the orbital motion have led to mass estimates for three asteroids, namely Ceres, Pallas and Vesta (Hertz, H.G., 1968, Science 160, 299; Schubart, J., 1975, Astron. & Astrophys. 39, 147). However, many other asteroids are now known to be much larger and presumably much more massive than previously believed, and consequently the orbital perturbation technique due to close encounters might be applicable to additional objects.

Table I lists the largest asteroids which were the target bodies in the search for close encounters with another numbered asteroid. The search program uses the given target asteroid orbit and searches a file containing the orbits of all numbered asteroids to determine whether close encounters are possible between the two orbits. If not, the search continues with the next asteroid; if encounters are possible, the program

TABLE I

10 LARGEST ASTEROIDS

1973*		1975**		1977***	
Asteroid	Diam. (km)	Asteroid	Diam. (km)	Asteroid	Diam. (km)
1 Ceres	770	1 Ceres	960	1 Ceres	1003
2 Pallas	480	2 Pallas	540	2 Pallas	608
4 Vesta	480	4 Vesta	500	4 Vesta	538
15 Eunomia	220	10 Hygiea	410	10 Hygiea	450
3 Juno	190	704 Interamnia	320	704 Interamnia	350
10 Hygiea	190	65 Cybele	295	31 Euphrosyne	334
6 Hebe	185	52 Europa	280	511 Davida	323
7 Iris	175	511 Davida	280	65 Cybele	309
16 Psyche	170	15 Eunomia	255	52 Europa	289
511 Davida	155	31 Euphrosyne	250?	451 Patientia	276
				15 Eunomia	272

* Pilcher, F., and J. Meeus, "Table of Minor Planets".

** Chapman, C.R., "Asteroids" in McGraw-Hill Encyclopedia of Science and Technology, 4th Ed. (in press).

*** Zellner, B., and E. Bowell (1977), Asteroid Compositional Types and Their Distributions, in The Interrelated Origin of Comets, Asteroids, and Meteorites, A. H. Delsemme, Editor, Univ. of Toledo Publications (in press).

computes the time history of the orbits to see if the closest approach distance is less than the desired criteria. If so, the relevant parameters of the encounter such as encounter speed, closest distance, date, etc., are stored. In this manner, all possible close encounters within a certain period of time are found. The initial search was based upon orbits listed in the Minor Planet Ephemeris, augmented by improved orbits for a few asteroids from the Minor Planet Center. A maximum separation of 0.1 AU was used for the closest approach distance and the search was for close encounters between 1970 and 1990. This search produced a number of close encounters which were potential candidates for mass determination. However, during the process of validating the close encounter orbits, it was discovered that some encounters could have been missed during the search. This resulted from the fact that orbits listed in the Minor Planet Ephemeris frequently have epochs as long as 20, 30, or even 40 years before the closest approach date, hence the effect of planetary perturbations was neglected during the interval from orbit epoch to closest approach since the search program used only two-body trajectories. The effect of planetary perturbations is illustrated by Table II, which lists the best closest encounters from the conic search along with the improved closest approach distance found by numerically integrating both orbits to the encounter date. Typically, only the closest approach distance changes significantly with the relative enounter speed showing only small differences. Some of the encounters show large changes in the closest approach distance, e.g., 52 Europa-76 Freia

TABLE II

ENCOUNTERS FROM 1970-1990 RESULTING IN

LARGEST DEFLECTIONS OF THE ENCOUNTERING BODY

Target Asteroid	Encountering Asteroid	Date	Osculating Closest Approach (AU)	Integrated Closest Approach (AU)
1 Ceres	534 Nassovia	12/75	.023	0.022
1 Ceres	1801 1963UR=52SP	11/84	.03	0.184
4 Vesta	197 Arete	1/76	.035	0.035
4 Vesta	146 Velleda	7/82	.01	0.040
4 Veata	1044 Teutonia	1/79	.05	0.119
4 Vesta	1601 Patry	4/88	.05	0.059
10 Hygiea	64 Angelina	1/90	.06	0.216
10 Hygiea	1363 Herberta	6/82	.10	0.167
15 Eunomia	1313 Berna	3/69	.06	0.056
52 Europa	76 Freia	12/82	.01	0.354
65 Cybele	609 Fulvia	3/70	.01	0.088

indicated a closest approach distance of only 0.01 AU when the ephemeris orbits were used but upon full integration, the closest approach distance is actually 0.35 AU - a value so large, that it should not have been considered under the original criteria. However, the change in closest approach distance could be negative as well as positive, and the large change between osculating and integrated results indicates that some encounters could have been missed since the osculating closest approach could be larger than the minimum criterion, whereas the integrated distance would be well within our limit.

In order to have a high probability of finding all dynamically interesting close encounters, the conic search was redone with a maximum closest approach distance of 0.35 AU. This search generated several thousand close encounters between 1970 and 1990 involving one of the largest asteroids and another numbered asteroid. This candidate list was winnowed by eliminating all encounters which resulted in a deflection of $< 0\overset{\circ}{.}05$ during the closest approach. The deflection angle, θ, was adopted as a measure of the perturbation, where

$$\theta = \pi - 2 \tan^{-1} (1 + rv^2/\mu),$$

with r = minimum encounter distance, v = relative speed of encounter and μ, the gravitational parameter of target asteroid = G * M, is calculated assuming a density of 3 gm/cm^3. θ is essentially the angle through which the asymptote of the hyperbolic approach trajectory is rotated during the close encounter.

The best encounters from the final search are listed in

Table III, divided into two parts: (A) for the first priority objects for further study and (B) for lower priority objects. Selected integrations have been done and the integrated values are indicated in parentheses. It should be noted that the computer file containing the asteroid orbits was substantially improved over the past year by D. Bender of Jet Propulsion Laboratory. He added fully integrated orbits for over 100 asteroids to a 1978 epoch, along with integrated elements at every 70 days, and improved numerous other orbits using data obtained from the Minor Planet Center at Cincinnati (prior to its relocation to Cambridge). Hence, for many cases, there should be little change between the osculating and integrated results.

The search uncovered potentially interesting encounters including several very low approach velocity encounters, particularly the 16 Psyche-1725 Crao encounter at 0.26 km/sec which is by far the lowest encounter speed yet found, lower by a factor of $\sim$20 than the mean encounter speed in the asteroid belt. It is interesting to speculate that the mechanism proposed by Hartmann and Cruikshank to explain the irregular shape of Hektor, namely a very low velocity collision between two nearly equal size objects that results in coalescence rather than fragmentation, also operates in the mainbelt and could produce objects such as 15 Eunomia or 45 Eugenia, which are large, irregular-shaped objects.

Encounters listed in Table III are being evaluated for mass information and are being considered for an astrometric

TABLE III - Best Encounters from Second Conic Search

A) First Priority

Encountering Asteroid	Date	Closest Approach (AU)	Relative Speed (km/s)	Deflection Angle (")
		Target Asteroid: 4 Vesta		
486 Cremona	11/6/72	.210	1.69	.245
" "	4/30/80	.083	1.92	.146
1393 Sofala	3/16/81	.045	1.79	.311
1914-70EV	11/15/78	.163 (.142)	1.50 (1.54)	.123
206 Hersilia	6/9/80	.153 (.208)	2.28 (2.45)	.056
1449 Virtanen	7/14/81	.248	1.77	.058
1634-1935QP	5/19/84	.112 (.113)	1.19 (1.20)	.284
2009	7/19/80	.165	1.92	.074
		Target Asteroid: 10 Hygiea		
111 Ate	4/29/78	.102	1.90	.071
1200 Imperatrix	8/22/79	.179	1.65	.054
1482 Sebastiana	6/8/78	.062 (.053)	2.31 (2.31)	.081
		Target Asteroid: 15 Eunomia		
1284 Latvia	6/13/77	.024	1.53	.104
" "	10/2/81	.039	1.42	.074
		Target Asteroid: 16 Psyche		
1542 Schalen	5/30/82	.245	0.52	.068
1725 Crao	9/16/84	.166	0.26	.403
		Target Asteroid: 65 Cybele		
1778 Alfven	1/31/72	.110	1.06	.069
		Target Asteroid: 704 Interamnia		
881 Athene	9/6/86	.036 (.046)	1.79 (1.81)	.107

TABLE III - Best Encounters from Second Conic Search

B) Second Priority

Encountering Asteroid	Date	Closest Approach (AU)	Relative Speed (km/s)	Deflection Angle (")
	Target Asteroid: 4 Vesta			
126 Velleda	7/9/82	.012	3.87	.245
460 Scandia	12/16/72	.013	3.63	.261
873 Mechthild	7/2/85	.107	1.93	.113
1549 Mikko	8/29/70	.156	2.20	.059
1966	3/6/73	.133	2.23	.068
1516 Henry	2/23/85	.088	2.02	.125
1601 Patry	3/19/88	.066	1.26	.414
1831 Nicholson	5/30/82	.211	1.60	.083
1904 Massevitch	1/20/84	.253	1.79	.055
1914	7/4/83	.112	2.41	.069
	Target Asteroid: 10 Hygiea			
382 Dodona	8/13/73	.131	1.68	.071
1273 Helma	12/22/71	.170	1.70	.054
1135 Cochlis	2/2/89	.061	2.70	.059
	Target Asteroid: 15 Eunomia			
1313 Berna	3/22/70	.039	0.91	.178
	Target Asteroid: 16 Psyche			
1122 Neith	1/25/75	.023	1.94	.052

program to be carried out in collaboration with E. Bowell of Lowell Observatory. The most useful objects for near term observations are those which have periodic close encounters, an encounter that happened several years ago so that perturbations have had a chance to manifest themselves, or those for which a good encounter is coming up shortly so that a high quality pre-encounter orbit can be obtained.

TASK 2: OUTER PLANET INVESTIGATIONS

Principal Investigator: Michael J. Price

2.1 Probing the Outer Planets with the Raman Effect

Introduction. In principle, the Raman effect provides a powerful astrophysical tool for determining the physical structure of planetary atmospheres in general. But, in practice, the Rayleigh and Raman scattering cross-sections of the predominant gas must essentially be of the same order of magnitude for the Raman effect to be readily detectable. Moreover, the atmosphere must be optically deep, aerosol particle scattering being relatively insignificant. Fortuitously, H_2 is one of the only gases for which the former condition is met. Development of the Raman probe technique is therefore directly relevant to the four outer planets. Both Uranus and Neptune are prime candidates, since the consensus of present evidence indicates that their atmospheres are deep and essentially clear above the clouds and are composed of nearly pure H_2. Their optical scattering properties at wavelengths less than about 6000Å appear to be determined almost completely by Rayleigh and Raman scattering.

The Raman effect has two important features which together make it effective in probing H_2 planetary atmospheres. First, the efficiency of both Rayleigh and Raman scattering increases essentially as the inverse fourth power of the incident wavelength. Because the optical depth (at $\lambda \lesssim 6000$Å) is directly proportional to the effective Rayleigh/Raman scattering cross-section, the mean physical depth to which photons penetrate before reflection (i.e., the integrated number of H_2 molecules

in the line of sight) varies essentially as the fourth power of the wavelength. Therefore, the Raman contribution function will move progressively deeper into the atmosphere with increasing wavelength. Second, the intensities of the Stokes and anti-Stokes lines in the optically thin case are proportional to the populations of their corresponding initial states; the intensity ratio is proportional to the population ratio in terms of the Boltzmann distribution. More generally, the intensity ratio is a function of the population ratio which is related to temperature.

During the NASA Planetary Astronomy contract NASW-2843, Price (1977) successfully demonstrated the feasibility of using the H_2 rotational Raman spectrum to investigate the physical structures of the outer planet atmospheres. By selecting distinct wavebands spaced throughout the visible spectrum for observation, a wide range in physical depth can be probed. On the basis of a semi-infinite homogeneous pure H_2 atmospheric model, computations of the strengths of the S(0) and S(1) lines were made for a wide range of physical conditions. For each characteristic wavelength the ratio of the S(0)/S(1) line strength is independent of the presence of aerosol particles. It provides a useful estimate of Boltzmann temperature. In contrast, the absolute strengths of the S(0) and S(1) lines are extremely sensitive to haze. Very small quantities of aerosol particles can be detected even at high altitudes. Initial applications of the Raman probe technique to Jupiter and Uranus were reported. For Jupiter, a weak aerosol haze appears to exist at an H_2 column density of $\lesssim$ 17 km. amagat. For Uranus, aerosol particles appear to be present at an H_2 column density of $\lesssim$ 104 km. amagat. In

addition, a significant temperature inversion may be present in the same region of the atmosphere.

In the initial PSI feasibility study, Price (1978) adopted three major simplifications in his treatment of the radiative transfer problem. First, multiple Raman shifts were not included in the computation of the so-called continuum background level in the spectrum. Second, the aerosol particles were assumed to conservatively scatter radiation. Third, the S(0) and S(1) line strengths' predictions were restricted to an integration over the entire visible hemisphere of the planet. Further development of the Raman probe technique, in which these simplifications were eliminated, is described in this report.

Theory. Our radiative transfer model consists of a semi-infinite, hazy, homogeneous, isothermal H_2 atmosphere in hydrostatic equilibrium. Temperatures in the range $0<T<150^{o}K$, relevant to outer planet atmospheres, are adopted. It is assumed that the H_2 molecules are completely thermalized so that their energy levels are populated according to the Boltzmann distribution. Table IV shows the relative populations as functions of temperature and energy level. To an excellent approximation, all H_2 molecules can be taken to be initially in their lowest vibrational state (v=0). For the temperatures of interest the population of the rotational state J=2 is negligible. Consequently, all H_2 molecules can be taken to be initially in the J=0 and J=1 states. Table V lists the relevant Raman transitions. Wavenumber shifts are taken from the adopted tabulations of Rayleigh and Raman scattering cross-sections given by Ford and Browne (1973).

Wallace (1972) has derived the equations of radiative transfer for the Raman scattering problem. Our predictions of the strengths of the S(0) and S(1) rotational Raman lines were based on his approximate solution. From Wallace (1972), we have

$$I_{i+1}(0,\mu) = \frac{q_1 q_2 \cdots q_i}{i!} \frac{\partial^i I_1(o,\mu)}{\partial \tilde{\omega}_1^i} \qquad (1)$$

TABLE IV. VARIATION WITH TEMPERATURE OF THE ROTATIONAL DISTRIBUTION OF H_2 MOLECULES

Temperature (^{o}K)	Rotational State Population*				
	J=0	J=1	J=2	J=3	J>3
0	1	0	0	0	0
50	0.77	0.23	<<0.01	<<0.01	<<0.01
100	0.37	0.61	0.01	<0.01	<<0.01
150	0.24	0.71	0.04	0.01	<<0.01

*These are fractions of the total rotational state population (v = 0).

TABLE V. H_2 RAMAN SHIFTS

TRANSITION	WAVENUMBER (cm^{-1})
v=0, J=0 → v=0, J=2	354.39
v=0, J=1 → v=0, J=3	587.07
v=0, J=0 → v=1, J=0	4162.06
v=0, J=1 → v=1, J=1	4156.15
v=0, J=0 → v=1, J=2	4498.75
v=0, J=1 → v=1, J=3	4713.83

where $I_1(o,\mu)$ is the specific intensity of radiation emerging from the atmosphere which has suffered only Rayleigh or aerosol particle scattering; I_{i+1} is the corresponding intensity of radiation which has suffered i Raman shifts. The parameter μ is the cosine of the angle of emergence with respect to the outward normal. Adopting zero phase angle, we can set the angles of incidence and emergence to be equal. Physically, the parameter $\tilde{\omega}_1$ is the probability that if a photon collides with a gas molecule or aerosol particle, it will be scattered with no change in energy. The parameter q_i is the corresponding probability that a photon will experience a change in energy relevant to a selected Raman transition.

More specific definitions of the relevant parameters are

$$\tilde{\omega}_1 = \zeta_1/(\sigma_1 + k_1 + \lambda_1) \tag{2}$$

and

$$q_1 = \lambda_1/(\sigma_1 + k_1 + \lambda_1) \tag{3}$$

The parameter σ_1 is the effective Rayleigh/aerosol particle scattering cross-section. Specifically

$$\sigma_1 = \sigma_g(1 + \eta) \tag{4}$$

where σ_g is the effective Rayleigh scattering cross-section. The parameter η is given by

$$\eta = \frac{\lambda_g}{\lambda_\varepsilon} \cdot \frac{\sigma_g^o}{\sigma_g} \tag{5}$$

where σ_g^o is the effective Rayleigh scattering cross-section at 5500Å, λ_g is the mean free path in H_2 at 5500Å, and λ_c is the mean free path in the aerosol particles. For convenience, we assume that the cross-section of the aerosol particles does

not depend on wavelength. For homogeneous atmospheres, λ_g/λ_c is constant with optical depth.

The parameter ζ_1 is given by

$$\zeta_1 = (1 + p\eta)\ \sigma_g \qquad (6)$$

where p is the single scattering albedo for an individual aerosol particle. The parameter λ_1 is the cross-section for Raman scattering from wavelength 1 to wavelength 2, weighted according to the fraction of H_2 molecules in the initial state; the cross-section is taken to be relevant either to the S(0) or S(1) transition. The parameter k_1 is the effective cross-section for Raman scattering from wavelength 1 to wavelengths other than wavelength 2. It includes all suitably weighted Raman transitions shown in Table V except that covered by λ_1. Although σ_1 and ζ_1 are dependent on the aerosol content of the atmosphere, λ_1 and k_1 are not.

Photons suffering more than two Raman shifts were not included in our treatment of the Raman scattering problem. Results published by Wallace (1972) show that neglecting high-order Raman scatterings does not lead to serious error in the determination of the continuum level of the spectrum of the atmosphere. The maximum uncertainty is less than ∿2 percent. McElroy (1971) has obtained a relevant analytical solution of the basic transfer equation for a semi-infinite homogeneous isotropically scattering planetary atmosphere. His solution, which utilizes the two-stream approximation to describe the radiation field, is eminently suitable for the computation of I_1, I_2, and I_3. It is well known that the two-stream approximation leads to uncertainties of 10-15 percent in predictions

of absolute intensity. But, since we are interested only in the detectability of the Raman "ghost" images against the background continuum, systematic errors in the corresponding predicted intensities largely cancel. This point has been discussed more fully by Price (1977).

Results. Theoretical computations of the spectral detectability of both the S(0) and S(1) rotational Raman lines were made for both clear and hazy atmospheres. In the present context, spectral detectability means the strength of the Raman "ghost" feature as a fraction of the background continuum level. Our initial computations focussed on the effect of multiple Raman shifts on predictions of spectral detectability.

Figure 4 shows the spectral detectability of the S(0) H_2 rotational Raman line as functions of both wavelength and population of the initial state. Our predictions refer to the center of the planetary disk (μ=1). A clear, semi-infinite, H_2 atmosphere was assumed, with all H_2 molecules residing in the lowest vibrational level (v=0). The parameter f indicates the fraction of H_2 molecules in the J=0 rotational state; (1-f) is the corresponding fraction in the J=1 state. Figure 5 shows the corresponding predictions for the S(1) line.

For both the S(0) and S(1) Raman lines, our calculations show that the spectral detectability is insensitive to wavelength, but nearly linearly dependent on the population of the initial state. This implies that the S(0)/S(1) line strengths' ratio should be a sensitive indicator of kinetic temperature. Our results confirm the earlier work by Price (1977). Not surprisingly,

FIG. 4: S(0) RAMAN LINE STRENGTHS: VARIATION WITH WAVELENGTH

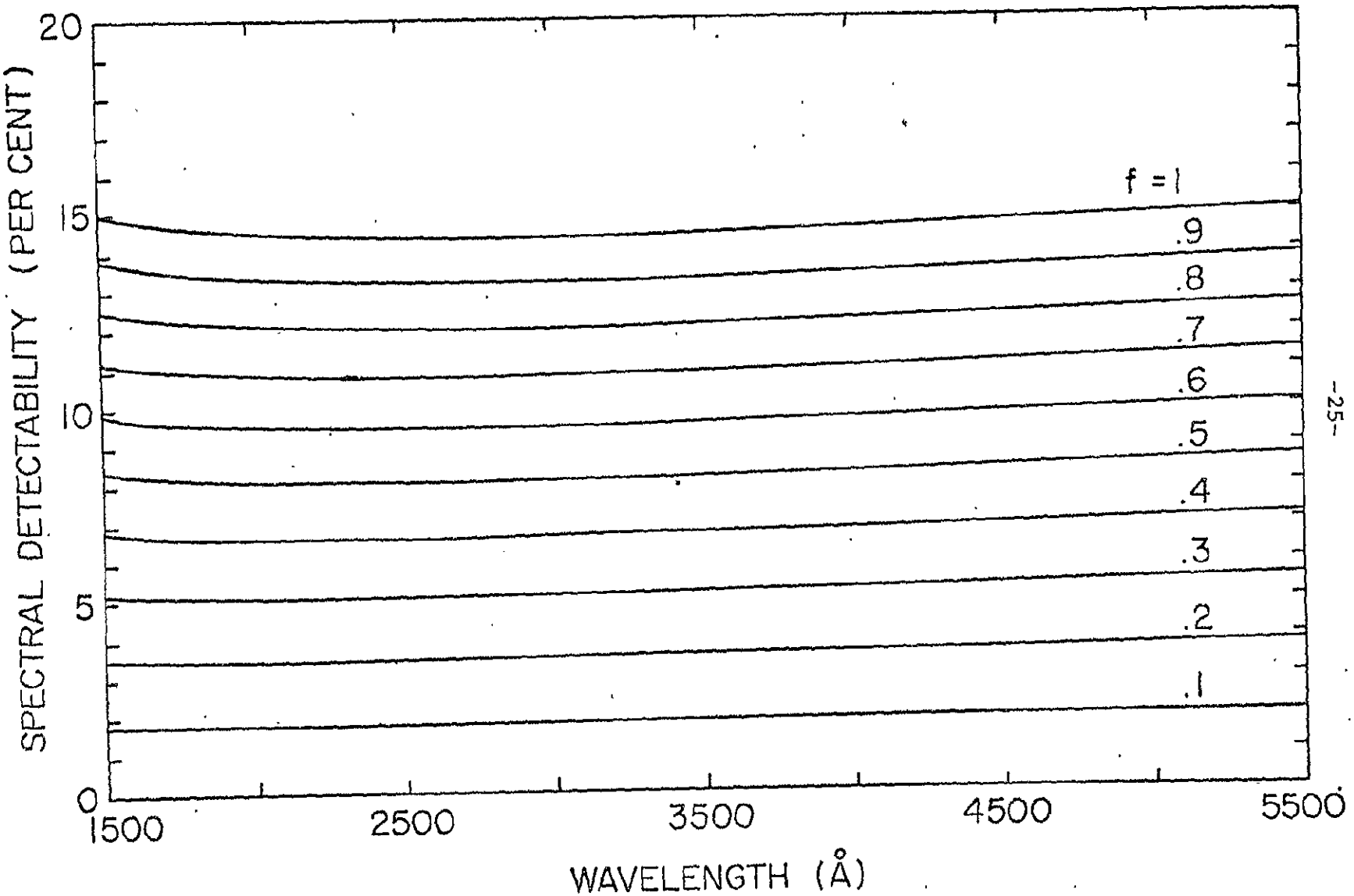

FIG. 5: S(1) RAMAN LINE STRENGTHS: VARIATION WITH WAVELENGTH

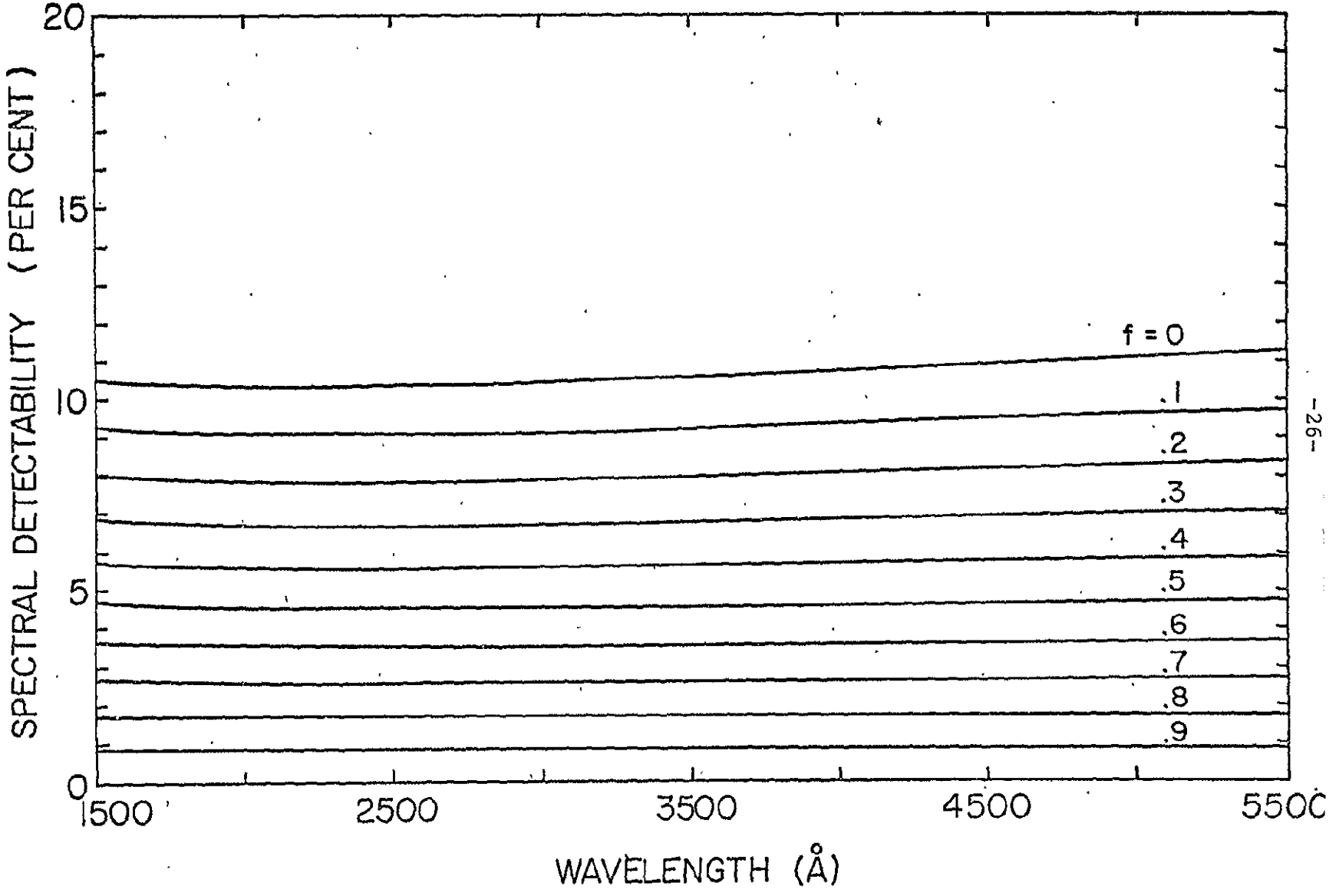

we find that spectral detectability is reduced by ∿25 percent by inclusion of multiple Raman shifts in the calculation of the continuum background. This reduction was expected to occur (Price, 1977), and it confirms the earlier investigation of Wallace (1972).

Spectral detectability of the S(0) Raman line as a function of the aerosol content of the atmosphere is shown in Figure 6. The aerosol particles are considered to be either totally absorbent (p=0) or to conservatively scatter radiation (p=1). The computations refer to the center of the planetary disk. All H_2 molecules were assumed to reside initially in the J=0 rotational state. A wavelength of 4000Å was selected. Evidently, the Raman line strength is especially sensitive to the cloud particle albedo for very tenuous hazes. Similar results were obtained for the S(1) Raman line. In that case, of course, all H_2 molecules were assumed to reside initially in the J=1 initial state. The S(1) line results are shown in Figure 7. Figures 8 and 9 compare the spectral detectabilities of the S(0) and S(1) lines as a function of the aerosol content for each choice of the cloud particle albedo. Evidently, whatever the cloud particle albedo, the S(0)/S(1) ratio of line strengths is insensitive to the aerosol content of the atmosphere. This is a major conclusion. It means that the S(0)/S(1) line strengths' ratio can be used as a reliable indicator of kinetic temperature. This result confirms the earlier investigation of Price (1977).

For both the S(0) and S(1) Raman lines, Figure 10 illustrates the variation of their spectral detectabilities across a planetary disk observed at zero phase angle. The absissa, μ, is the

FIG.6: S(0) RAMAN LINE STRENGTHS: VARIATION WITH AEROSOL CONTENT

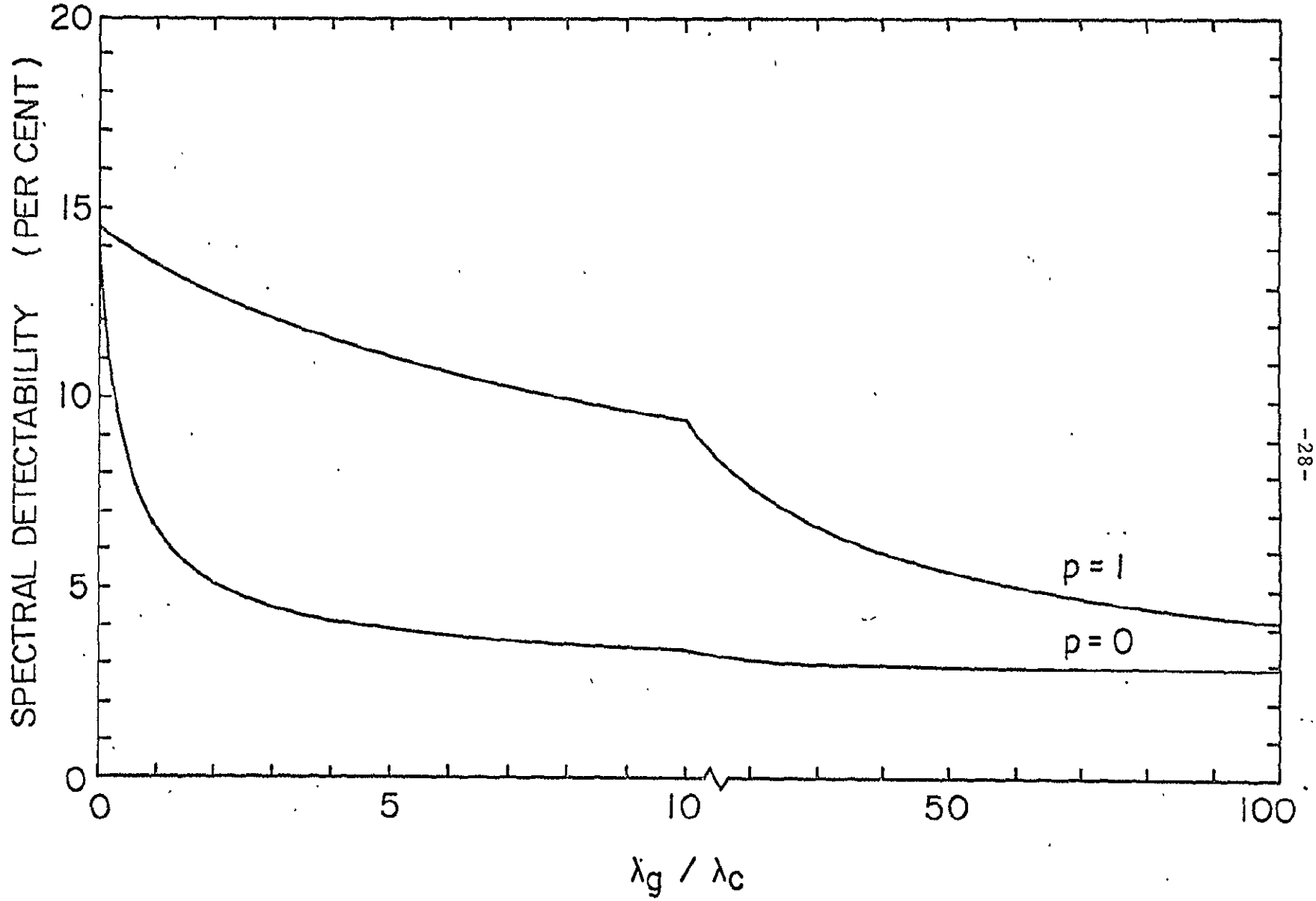

FIG. 7: S(1) RAMAN LINE STRENGTHS: VARIATION WITH AEROSOL CONTENT

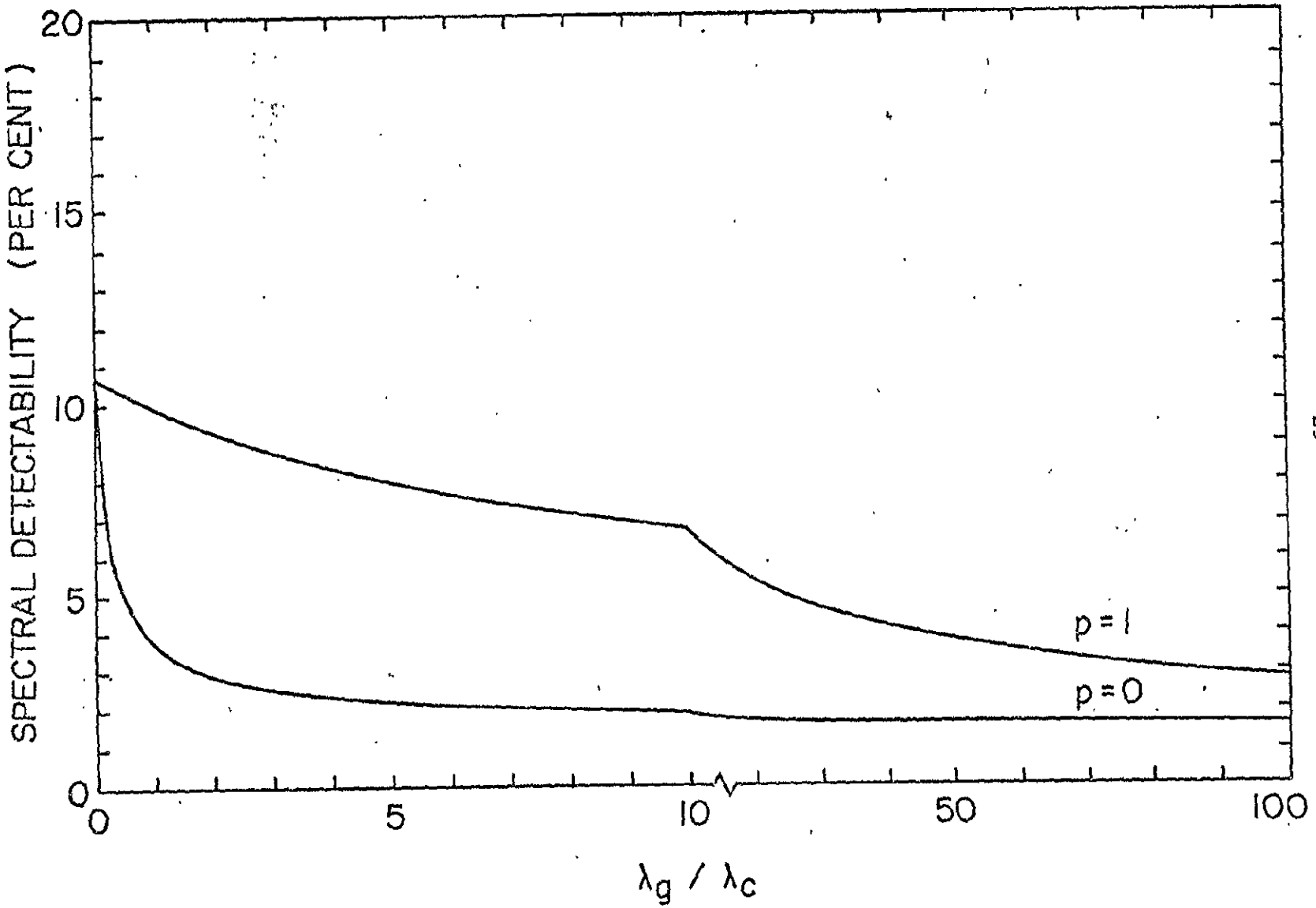

FIG. 8: ROTATIONAL RAMAN LINE STRENGTHS: VARIATION WITH AEROSOL CONTENT

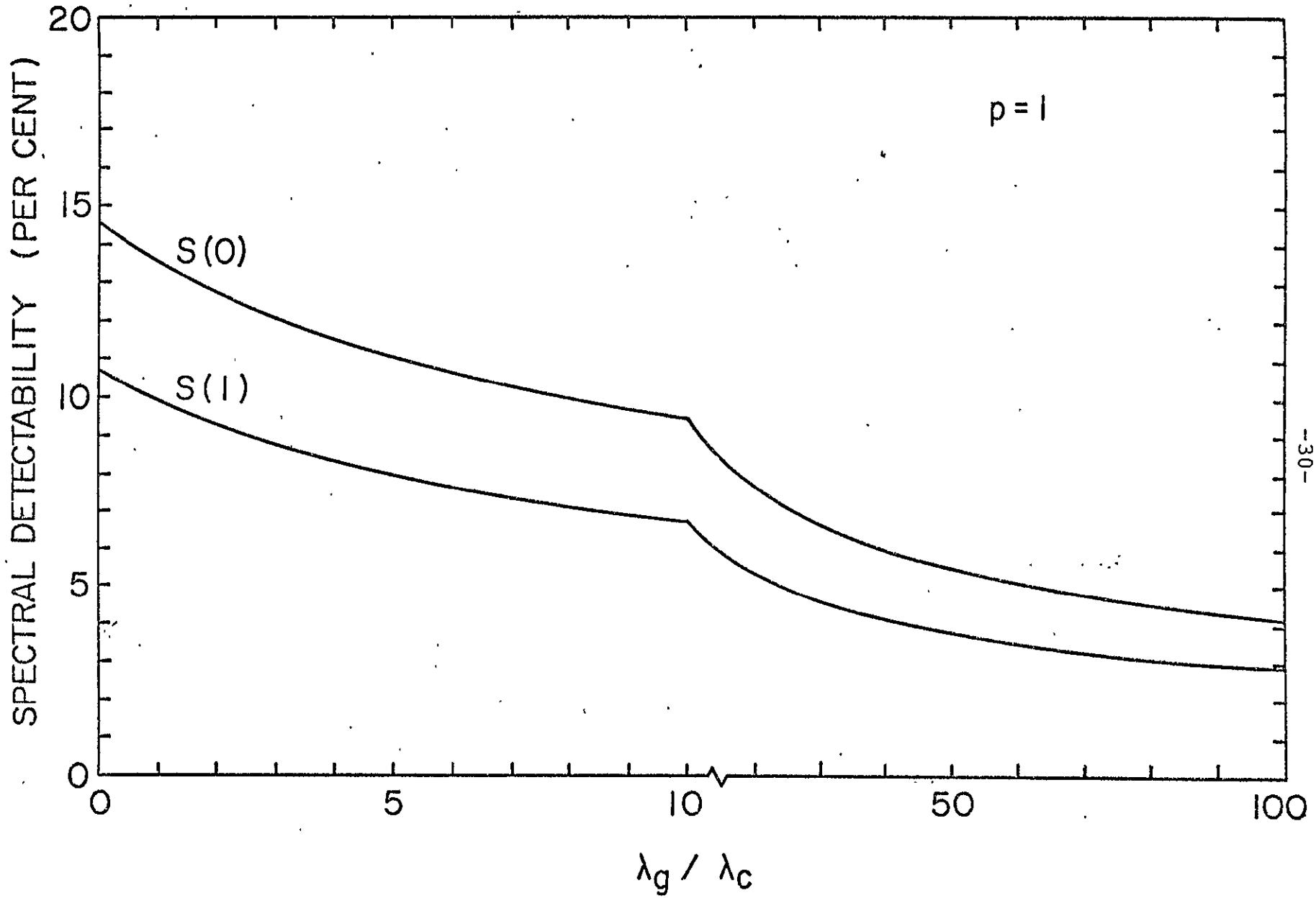

FIG.9 : ROTATIONAL RAMAN LINE STRENGTHS: VARIATION WITH AEROSOL CONTENT

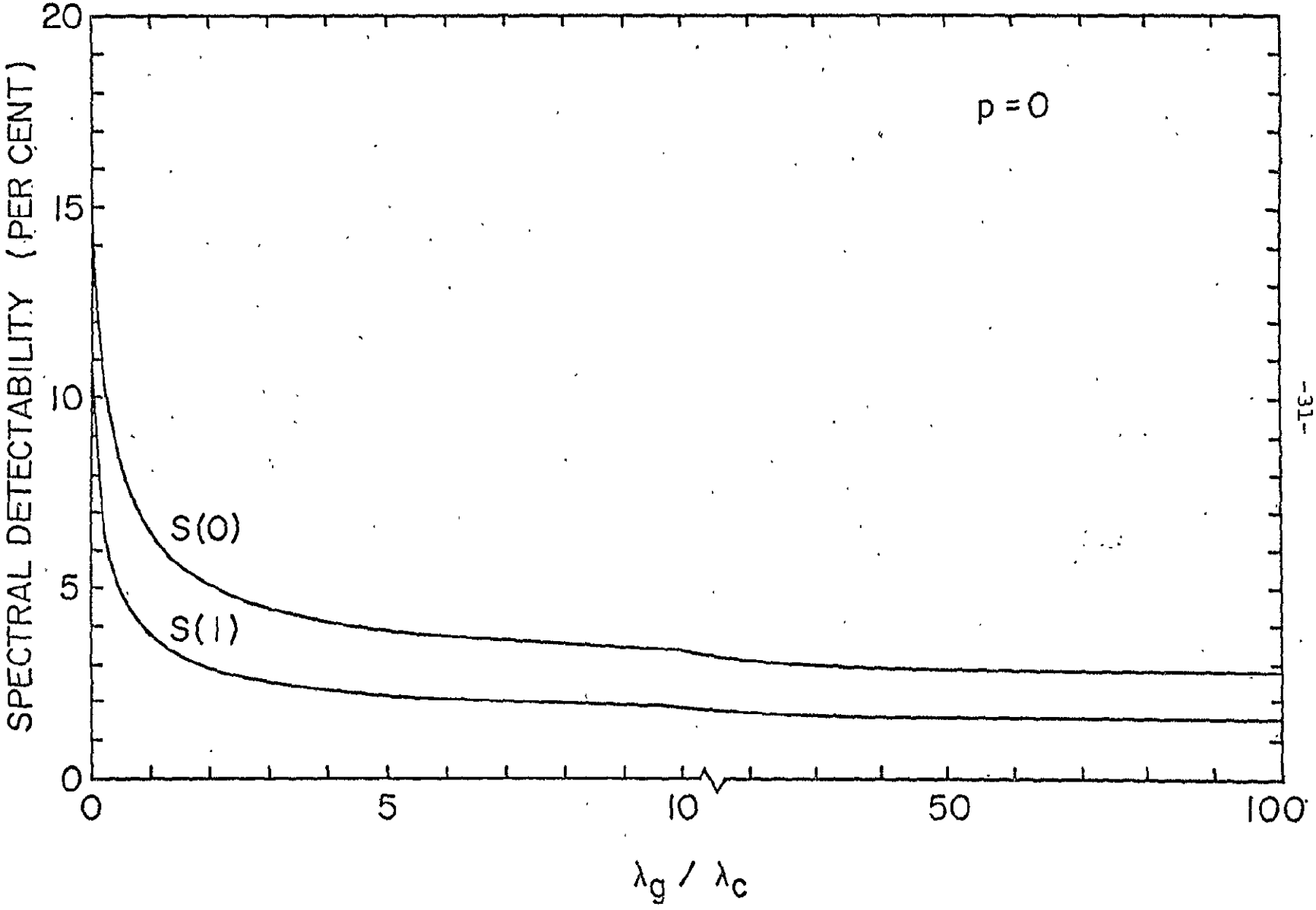

FIG. 10 ROTATIONAL RAMAN LINES: VARIATION ACROSS DISK

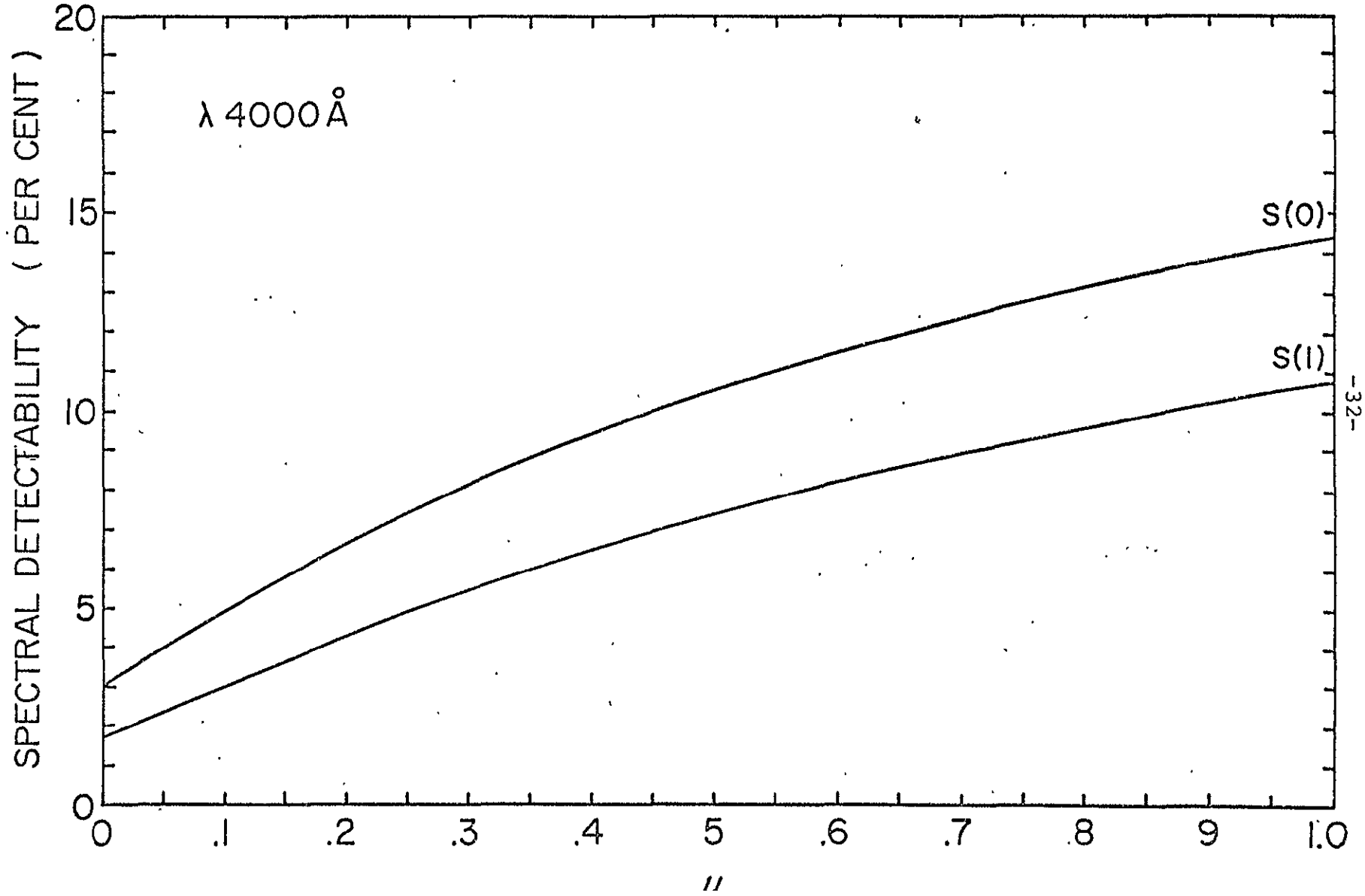

cosine of the angle of emergence with respect to the outward normal. The atmosphere was taken to be entirely clear of aerosol particles, and a wavelength of 4000Å was selected. To compute the S(0) curve, all H_2 molecules were assumed to reside initially in the J=0 state. For the S(1) curve, all molecules were placed in the J=1 state. Our results show that both Raman lines decrease in strength towards the limb, but that the ratio of their strengths is insensitive to position on the disk. These are major conclusions. They mean that the degree of lateral homogeneity of the atmosphere can be investigated by the Raman probe technique. Moreover, the kinetic temperature can be studied as a function of position on the disk.

References

Ford, A.L., and Browne, J.C. (1973). Rayleigh and Raman Cross-Sections for the Hydrogen Molecule, Atomic Data 5, 305-313.

McElroy, M.T. (1971). The Composition of Planetary Atmospheres, J. Quant. Spectrosc. Radiative Transfer 11, 813-825.

Price, M.J. (1977). On Probing the Outer Planets with the Raman Effect, Rev. of Geophys. Space Phys., 15, 227-234.

Wallace, L. (1972). Rayleigh and Raman Scattering by H_2 in a Planetary Atmosphere, Astrophys. J., 176, 249-257.

2.2 Uranus: Disk Structure

During the contract, our joint P.S.I./Lowell Observatory investigation of structure on the Uranus disk continued. Once again, the Franz area scanner was used, but this time the detector was a red-sensitive RCA type C31034B photomultiplier. By comparison with the 1976 Uranus observations, the signal-to-noise ratio was improved by a factor ∿5 throughout the wavelength range 6000 - 9000Å. On July 10, 1977, an excellent set of one-dimensional slit scans of both Uranus and the point spread function was obtained during very good seeing conditions. Data were obtained for the continuum wavebands at 6000Å, 6400Å, and 7500Å, and for the CH_4 bands at 6200Å, 7300Å, 8000Å, and 8500Å. Scans were made in both north-south and east-west directions. Throughout the observations, the slit width was held constant at 0".645 arc.

The 1977 July 10 observations have been analyzed to determine the true radial intensity distribution in each waveband. To expedite the analysis, the observed intensity distributions for Uranus and the point spread function were taken to be circularly symmetric. Fourier-Bessel inversion techniques were used to remove the slit- and point-spread functions from the Uranus data. For each waveband, the true Uranus disk profile was derived with a spatial resolution ∿0".5 arc. The nominal angular diameter of Uranus is ∿4" arc.

Results obtained from the 1977 Uranus observations confirmed earlier work. But, more important, we discovered that not all CH_4 bands exhibit limb-brightening. Significant limb-darkening was found to occur in the two CH_4 bands at

8000Å and 8500Å, most probably because the deep-dense NH_3 cloud layer becomes faintly visible in these wavebands. In the CH_4 bands at 7300Å and 8900Å, limb-brightening occurs because the integrated line-of-sight absorption is sufficiently large that the deep NH_3 cloud layer cannot be seen. Interpreting our results in terms of elementary radiative transfer models, we conclude that the mean CH_4/H_2 mixing ratio in the Uranus atmosphere, above the NH_3 cloud layer, is no greater than about three times the solar value. Such a conclusion is in direct conflict with recent theoretical models for Uranus which require a much larger CH_4/H_2 mixing ratio in the visible atmosphere. A complete discussion of our results is contained in a paper entitled, "Uranus: Narrow-Waveband Disk Profiles in the Spectral Region 6000 - 8500 Angstroms," recently submitted for publication in Icarus. A preprint was included in the Third Quarterly Report.

Further numerical work on the restoration of the Uranus image has been carried out. Special attention was given to the deep CH_4 band at 7300 angstroms in which the presence of a polar cap and significant limb-brightening is suggested even in the absence of restoration. Significant polar- and limb-brightening were confirmed to be present on the Uranus disk. A complete discussion of our results is contained in a paper entitled, "Uranus: The Disk Profile in the 7300 Angstrom Methane Band." A copy of the manuscript is given in Appendix IV.

APPENDIX I

"Taxonomy of Asteroids"

by

Edward Bowell, Clark R. Chapman, Jonathan C. Gradie,
David Morrison, and Benjamin Zellner
Icarus 35, 313-335 (1978)

ICARUS 35, 313–335 (1978)

Taxonomy of Asteroids

EDWARD BOWELL,* CLARK R. CHAPMAN,† JONATHAN C. GRADIE,‡ DAVID MORRISON,§ AND BENJAMIN ZELLNER‡

**Lowell Observatory, P.O. Box 1269, Flagstaff, Arizona 86001, †Planetary Science Inst., 2030 E. Speedway, Tucson, Arizona 85719, ‡Lunar and Planetary Lab., University of Arizona, Tucson, Arizona 85721, and §NASA Headquarters, Washington, D.C. 20546 and Institute for Astronomy, University of Hawaii, Honolulu, Hawaii 96822*

Received January 16, 1978; revised March 12, 1978

A taxonomic system was introduced by C. R Chapman, D. Morrison, and B. Zellner [*Icarus* 25, 104–130 (1975)], in which minor planets are classified according to a few readily observable optical properties, independent of specific mineralogical interpretations. That taxonomy is here augmented to five classes, now precisely defined in terms of seven parameters obtained from polarimetry, spectrophotometry, radiometry, and *UBV* photometry of 523 objects. We classify 190 asteroids as type C, 141 as type S, 13 as type M, 3 as type E, and 3 as type R; 55 objects are shown to fall outside these five classes and are designated U (unclassifiable). For the remaining 118, the data exclude two or more types but are insufficient for unambiguous classification. Reliable diameters, from radiometry or polarimetry or else from albedos adopted as typical of the types, are listed for 396 objects. We also compare our taxonomy with other ones and discuss how classification efforts are related to the interpretation of asteroid mineralogies.

I. INTRODUCTION

Physical observations of the surfaces of asteroids indicate a wide variety of compositional types. For instance, the distribution of objects with respect to both broad-band color (e.g., *B–V*) and albedo are strongly bimodal (Zellner *et al.*, 1974; Morrison, 1974, 1977a,b; Hansen, 1976). Spectrophotometry with 24 filters distinguishes about 34 distinct spectra (McCord and Chapman, 1975a,b), while a recent classification by Gaffey and McCord (1977a,b), contains 13 groups that emphasize interpretation in terms of mineralogical assemblages. The large body of observations being accumulated clearly requires some ordering as an aid to discussion and improved understanding of the physical properties of asteroids.

In this paper we discuss in detail a taxonomic system, *based on seven directly observable optical parameters* from four observational techniques, that provides a useful structure within which to fit a large number of individual observations. The classification scheme is entirely empirical and divorced from mineralogical interpretations. Our system uses a few broad groups, chiefly those rather naturally defined by bimodalities or hiatuses in one or more parameters, rather than a large number of subsets which could be distinguished from the same data for the better observed asteroids. The breadth of our classes has the advantage of permitting about a quarter of the numbered asteroids to be classified, but the disadvantage of not resolving potentially important differences within the broad classes. We hope and expect that the several classes we define here will prove useful for elucidating the nature of the asteroids. The philosophy and

0019-1035/78/0353-0313$02.00/0

history of asteroid taxonomy and the relationship to interpretation of asteroid mineralogy are discussed in Section V.

The clear separation of many of the larger asteroids into two albedo–color groups suggested the first major classification, the classes called C and S. The C objects are dark and neutral in color, apparently due to the presence of opaque compounds of carbon, and appear to be mineralogically similar to the carbonaceous chondrite meteorites (Johnson and Fanale, 1973), while the S objects appear to contain such silicates as pyroxene and olivine and perhaps are related to the stony-iron meteorites (McCord and Gaffey, 1974). Although the C and S terminology suggests an identification with meteorite types, the classes have been *defined* purely in terms of observed clumping of observational parameters. As presented by Chapman, Morrison, and Zellner (1975; hereafter CMZ), the definition was in terms of five observable quantities. These authors suggested that about 90% of the mainbelt asteroids fall into one or the other of these two broad classes.

CMZ recognized at least two additional types: one consists of the unique object 4 Vesta with its surface of pigeonitic basalt (McCord *et al.*, 1970; Larson and Fink, 1975), and the other contains the three objects 16 Psyche, 21 Lutetia, and 22 Kalliope, of intermediate albedo and with straight, reddish spectra probably due to metal, as in enstatite chondrites or nickel–iron meteorites (Chapman and Salisbury, 1973). Zellner and Gradie (1976) subsequently designated this second group the M class. In addition, Zellner (1975) noted the unique high albedo and neutral color of 44 Nysa and suggested that it has an enstatite achondritic composition, and Zellner *et al.* (1977a) subsequently identified two more objects with similar optical properties. While it remains true that the great majority of asteroids are either C or S, new observations have continued to reveal additional types.

As more and more physical observations of asteroids have been made, the data base upon which a taxonomy of asteroid optical properties can be established has rapidly expanded. Over the past year we and others have created a computer file of these data called TRIAD (Tucson Revised Index of Asteroid Data; Bender *et al.*, 1978). One of the first projects to be undertaken with this file has been the definition of a useful taxonomy based on several parameters. Further, we hope to establish the correlations among the various observational parameters in order to evaluate with what confidence reconnaissance data (such as *UBV* colors) can be used to classify an asteroid.

For those asteroids observed in sufficient detail, many different surface types may be distinguished and, indeed, each asteroid may ultimately be recognized as unique. In the taxonomic system discussed here, it should be understood that each class contains a substantial spread of mineralogical assemblages; for instance, there is a factor of 3 variation in the albedos of C asteroids, and the S asteroids encompass a wide range of pyroxene and olivine contents as indicated by the depth and position of the absorption band near 0.95 μm. The primary advantages of the classification system discussed here are: (1) it can be widely applied, since it depends upon only a few readily observed parameters; (2) it clearly distinguishes the major albedo classes, thus permitting diameters to be estimated and enabling sampling corrections to be applied for determining the unbiased distributional properties of asteroids; (3) it permits the ready identification of unusual objects from reconnaissance data; (4) it probably distinguishes objects that are geochemically differentiated from those with more primitive surface compositions (see Section V); and (5) the system requires no revision when mineralogical interpretations are

modified or improved, since it is based strictly upon observational parameters.

II. THE DATA BASE

The observations of more than 500 asteroids that now constitute the TRIAD data file have generally been made recently and are not yet all published. The number of objects that can be classified is approximately five times the number considered by CMZ three years ago. Furthermore, new data permit firm classifications of many asteroids that were classified only tentatively in CMZ.

Data from four observational techniques are incorporated into the classification scheme: *UBV* photometry; 0.3 to 1.1 μm spectrophotometry; photoelectric polarimetry; and infrared radiometry. Each of the seven observational parameters is assigned a weight or quality code ranging from 1 for data in need of confirmation to 3 for the most securely determined values.

The *UBV* photometry has been carried out primarily at the Lowell Observatory and at the University of Arizona. The principal published sources are Taylor (1971), Zellner *et al.* (1975, 1977b), and Degewij *et al.* (1978). However, the majority of the data are unpublished observations made between 1975 and 1977 by E. Bowell at Lowell. Bowell has produced the combined TRIAD *UBV* list from a synthesis of all these observations. We use the parameters $B-V$ and $U-B$ for classification.

Spectrophotometry with about two dozen filters has been reported for 98 asteroids by McCord and Chapman (1975a,b) and Pieters *et al.* (1976). Three parameters used in the classification are R/B, the ratio of spectral reflectance at 0.70 μm to that at 0.40 μm; *BEND*, a measure of the curvature of the visible part of the reflectance spectrum, and *DEPTH*, a measure of the strength of the olivine-pyroxene absorption feature near 0.95 μm. The parameters are defined precisely by McCord and Chapman (1975a). Chapman has assembled these data for the TRIAD file.

Linear polarization of reflected light as a function of phase angle constitutes the third set of classification data. The observations are all from Zellner *et al.* (1974) and Zellner and Gradie (1976 and unpublished). The parameter $P_{\min}$, the maximum depth of the negative polarization branch, is listed in TRIAD for 98 objects and is sensitive to grain opacity and hence roughly to albedo. The polarimetry also yields geometric albedos p_V more directly, from the slope of the ascending polarization branch and a recently recalibrated slope-albedo law (Zellner *et al.*, 1977c,d). For albedos ≥ 0.07, the polarimetric results are now in quite satisfactory agreement with albedos and diameters from thermal radiometry. It is now recognized, however, that previously published polarimetric albedos <0.07 are inaccurate due to saturation of the slope-albedo law, and furthermore that reliable *visual* albedos p_V cannot always be inferred from polarimetric data in *blue* light. Whereas polarimetric albedos were listed for as many as 52 objects by Zellner and Gradie (1976), the number in TRIAD is now reduced to 24. The TRIAD polarimetry file is maintained by Zellner.

The final input to the classification is a geometric visual albedo derived from 10 and 20 μm. radiometry, carried out primarily by D. Morrison and his collaborators at the University of Hawaii and at Kitt Peak and by O. Hansen at Cerro Tololo. The individual observations have been published primarily by Cruikshank and Morrison (1973), Morrison (1974, 1977a), Hansen (1976), and Morrison and Chapman (1976); all are summarized in a review by Morrison (1977b). All of the observations have been reduced uniformly with the model described by Jones and Morrison (1974) and Morrison (1977b). The alternative model by Hansen (1977) also yields consistent albedos and diameters from

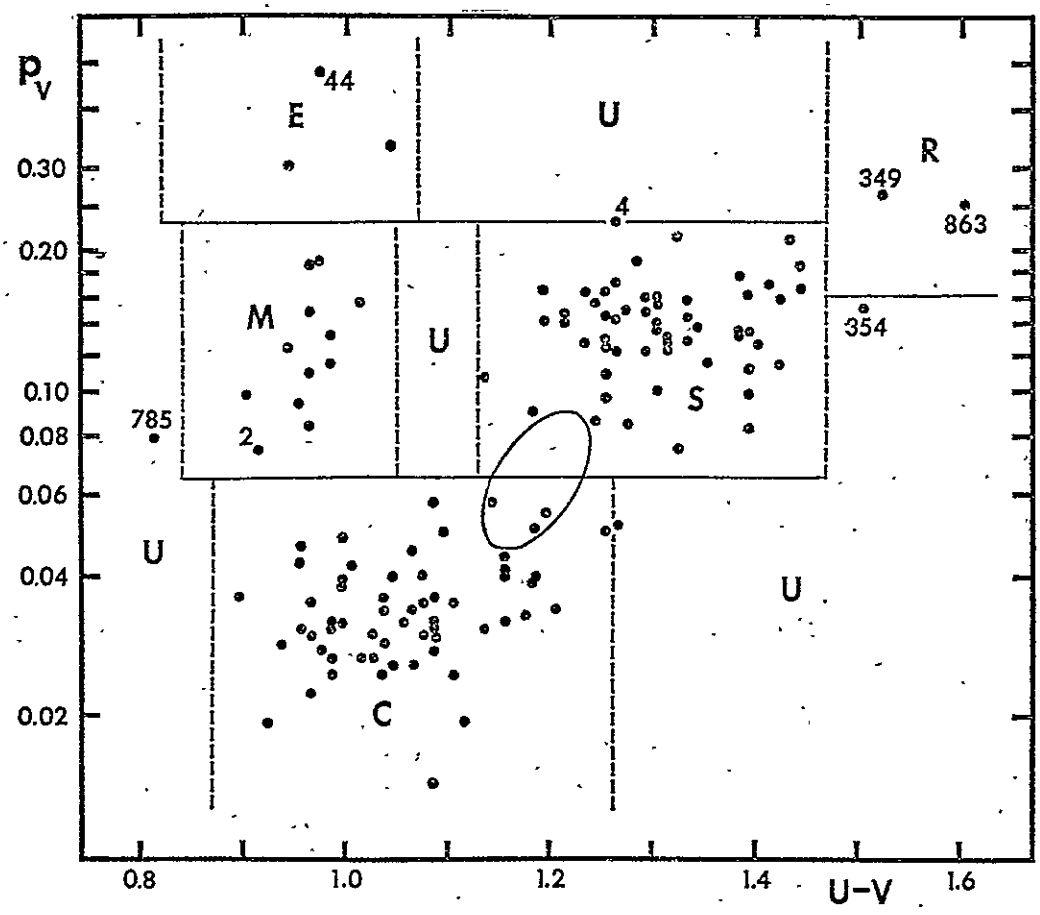

FIG. 1. Geometric albedo p_V versus $U-V$ color index for 140 minor planets with orbital semi-major axis ≤ 3.6 AU. Domains indicate allowable parameters for asteroids of types C, S, M, E, and R; objects outside these domains are unclassifiable, designated U. Albedo limits for the classes are determined from this figure, but limits in $U-V$ from Fig. 7 below. Unusual objects 2 Pallas, 4 Vesta, 44 Nysa, 349 Dembowska, 354 Eleonora, 785 Zwetana, and 863 Benkoela are indicated by number. Pallas is excluded from type M, and Vesta from type S, by other parameters not shown in this plot. Data are from the TRIAD file. The ellipse represents typical albedos and colors for objects in the Eos Hirayama family (see text).

radiometric data. Morrison maintains the TRIAD radiometry file.

To summarize, the observational parameters we employ are $B-V$ and $U-B$ color indices from the broadband photometry, the color ratio R/B and the parameters *BEND* and *DEPTH* from the spectrophotometry; the polarimetric parameter P_{min}, and the geometric albedo p_V. The albedo is taken as the weighted average of radiometric and polarimetric values where both are available.

III. DEFINITIONS OF TAXONOMIC CLASSES

The taxonomy described in this paper is based on directly observed optical parameters and, compared with other classifications, it is independent of asteroid mineralogy. We have attempted to locate discrete clusters in a series of two-parameter plots (see Figs. 1–6). Natural divisions clearly separate well-populated clusters. Of course, the boundaries between classes are not evident for each observational parameter

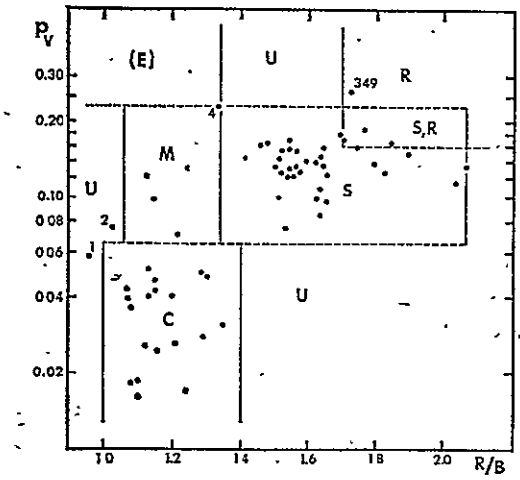

FIG. 2. Geometric albedo versus R/B color index for 65 asteroids. R/B is the ratio of the spectral reflectance at 0.7 μm to that at 0.4 μm. The unusual objects 1 Ceres, 2 Pallas, 4 Vesta, and 349 Dembowska are identified.

considered individually, but our classes are distinct from each other in several different ways. Several two-parameter plots that we have used to assign class boundaries, Figs. 1–6, may enable the reader to be convinced of the natural existence of most

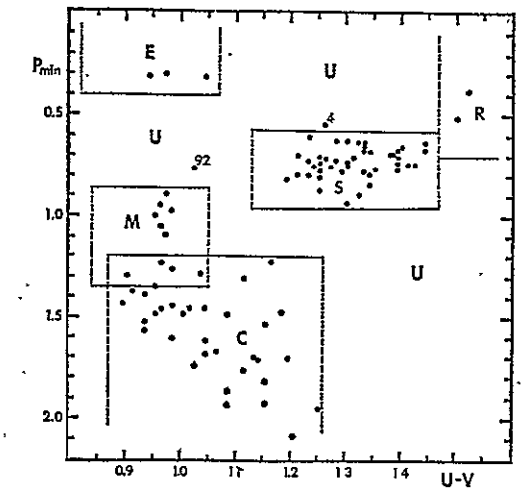

FIG. 3. Depth P_{min} of the negative polarization branch versus $U-V$ color index for 93 asteroids. Unclassifiable objects identified by number are 4 Vesta and 92 Undina. Limits in $U-V$ are defined in Fig. 7.

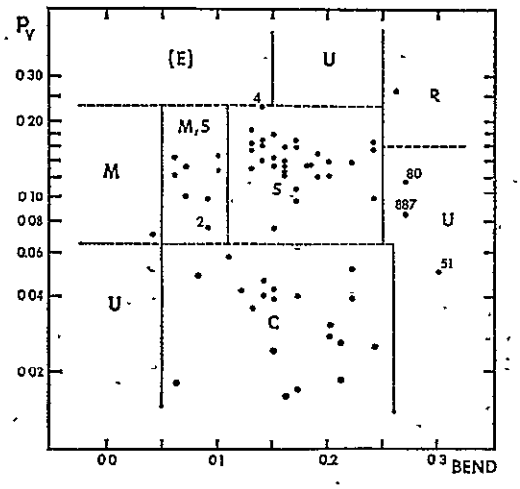

FIG. 4. Geometric albedo versus the spectrophotometric parameter *BEND* for minor planets. *BEND* is a measure of the curvature of the visible part of the reflection spectrum, as defined by McCord and Chapman (1975a). Unusual objects identified are 2 Pallas, 4 Vesta, 51 Nemausa, 80 Sappho, and 887 Alinda.

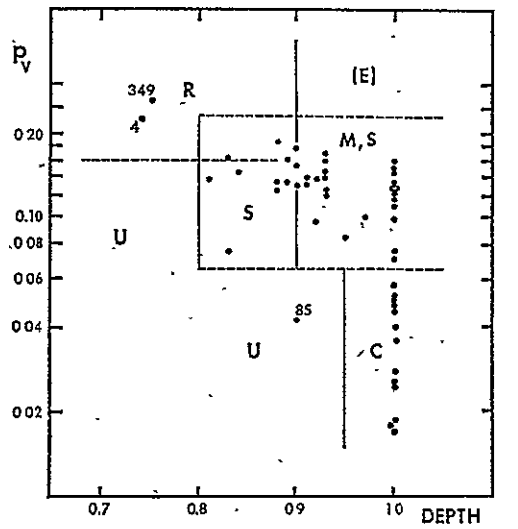

FIG. 5. Geometric albedo versus the spectrophotometric parameter *DEPTH* for minor planets. *DEPTH* is the ratio of the spectral reflectance at the bottom of the 0.95 μm absorption band (if present) to the highest reflectance at shorter wavelength. *DEPTH* cannot exceed unity by definition, and smaller values indicate a strong absorption feature. Unusual asteroids identified are 4 Vesta, 85 Io, and 349 Dembowska.

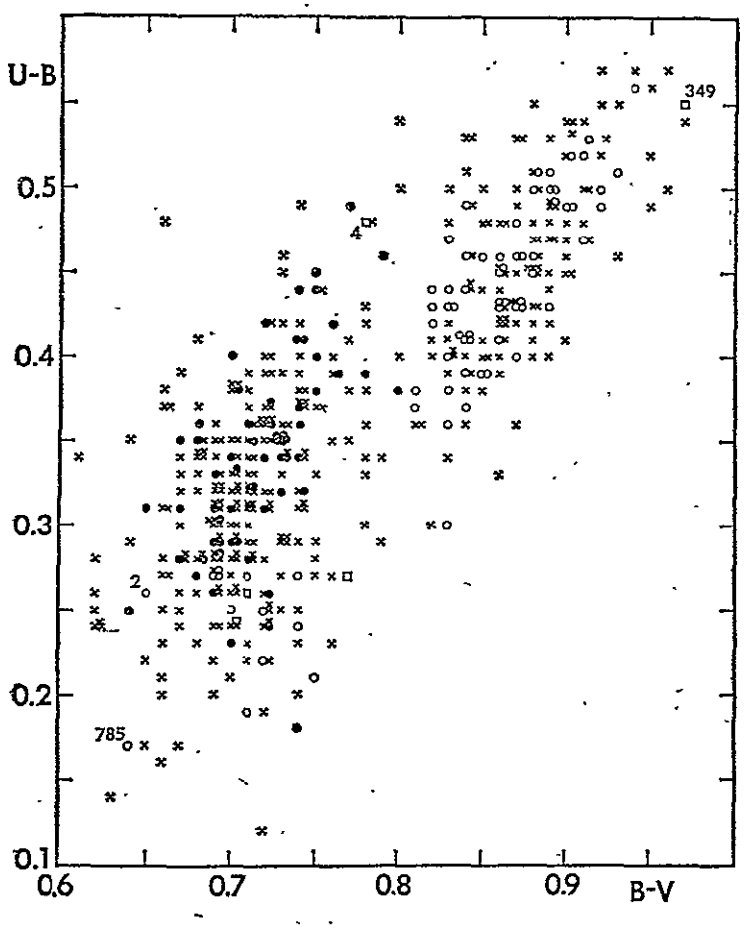

FIG. 6. $B-V$ and $U-B$ colors for 465 minor planets with orbital semimajor axis ≤ 3.6 AU. Symbols indicate geometric albedos from polarimetry or thermal radiometry, where available: (●) $p \leq 0.065$, as for C types; (○) $0.065 < p \leq 0.23$, as for S and M types; (□) $p > 0.23$, as for types E and R; and (×) no albedo information available. The R object 863 Benkoela ($p = 0.245$) is off scale at $B-V = 1.06$, $U-B = 0.56$, and 1658 Innes is off scale at $B-V = 0.96$, $U-B = 0.61$. Solar colors, representing neutral spectral reflectance, are at $B-V = 0.63$, $U-B = 0.10$. The unusual objects 2 Pallas, 4 Vesta, 349 Dembowska, and 785 Zwetana are indicated by number.

of our classes. The plotted data are all taken from the TRIAD file.

Since recent, specially targeted observations of the distant Trojan and Hilda-group asteroids (McCord and Chapman, 1975b; Degewij *et al.*, 1978) suggest that these objects constitute a different population not entirely typical of any main-belt class, we do not include in the plots any asteroids with semimajor axis greater than 3.6 AU, beyond the main belt. Although these asteroids were not used for defining the classes, we later provide the results of attempting to apply the main-belt taxonomy to them.

Five classes are defined below. Following previous usage, the first four of these are called C, S, M, and E. In addition to our more precise definitions of previously discussed classes, we adopt a new designation—class R—for the objects with reddest *UBV* colors, with high-spectral-contrast

visible and near-infrared spectra, and with moderately high albedos.[1] Finally, we employ a designation U (for "unclassifiable") for those objects that are not in classes C, S, M, E, or R. We emphasize that U does not simply indicate lack of information or noisy data, but refers to objects that are known to be intrinsically outside the domains of the other five classes. They are either unique, or else belong to types yet to be described.

In assigning boundaries between classes for each parameter, we have been guided by the desire to *minimize the number of misclassifications*. That is, where there is serious doubt as to correct classification of an individual asteroid, we prefer to carry several possibilities rather than to make an uncertain unique classification. Note that this philosophy is to be contrasted with one like that of Zellner and Bowell (1977), who attempted to assign the most likely class to each asteroid.

The C, S, M, E, and R classes are broad ones, with significant spread in the range of each parameter within each class. In addition, there is a further spread introduced into parameter plots by noise associated with the observational data on each asteroid. Application of our philosophy of minimizing the number of misclassifications leads us to define the boundaries between classes in parameter space generously—including cases in which the domains in some parameters can have considerable overlap. Thus, while there can be no ambiguity in classifications when all seven parameters have been measured, there frequently are ambiguities when only one or two are known. This is particularly a concern for *UBV* colors, since for nearly half the asteroids considered here only *UBV* data are available. We will discuss this problem in more detail when we address the *UBV* two-color plot below.

[1] Class R is similar but not identical to a provisional class designated "O" by Zellner and Bowell (1977).

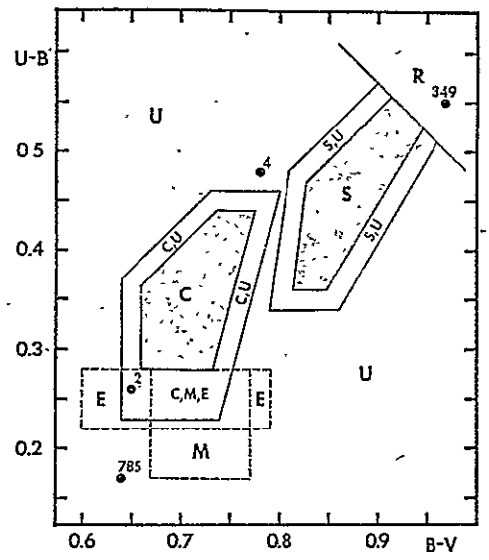

FIG. 7. Adopted domains of types C, S, M, E, and R in *UBV* colors, from Fig. 6. In cases where the only diagnostic parameters available are the *UBV* colors, type U is generated outside the shaded areas for C and S (resulting in classifications CU or SU); when $U-V \geq 1.47$ (resulting classification RU); and when $U-B \leq 0.28$ (classifications MU, EU, CEU, MEU, or CMEU) Numerical coefficients representing the type boundaries are given in Table I. Objects 2, 4, 349, and 785 are identified as in Fig. 6 Corners of the domains, representing limits in $U-V$, are projected in Figs. 1 and 3 above.

Figures 1 and 2 display the albedo p_V as a function of $U-V$ and R/B color indices. Both plots clearly distinguish the C, S, M, and E groups; we can almost invariably make unambiguous type classifications when both color and albedo data are available. We use Figs. 1 and 2 to establish the *albedo* boundaries in subsequent figures. (Note that the dotted line limits in $U-V$ are not definitions of class boundaries; the boundaries in the *UBV* plane are complex, as shown in Figs. 6 and 7, and cannot be described by the single parameter $U-V$. In each figure, solid lines represent parameter limits defined in that figure.) Figure 3 illustrates the albedo-sensitive parameter P_{min} as a function of $U-V$ color index. P_{min} separates the various classes better than any other single parameter, but still

TABLE I

DEFINITION OF CLASSES

Parameter	C	S	M	E	R
Albedo p_V	≤ 0.065	0.065–0.23	0.065–0.23	≥ 0.23	≥ 0.16
P_{min} (%)	1.20–2.15	0.58 –0.96	0.86 –1.35	≤ 0.40	≤ 0.70
R/B	1.00–1.40	1.34 –2.07	1.06 –1.34	0.9 –1.70[a]	≥ 1.70
BEND	0.05–0.26	0.05 –0.25	≤ 0.11	≤ 0.15[a]	≥ 0.25
DEPTH	0.95–1.00	0.80 –1.00	0.90 –1.00	0.90–1.00[a]	≤ 0.90
B–V	≥ 0.64[b]	—[c]	0.67 –0.77	0.60–0.79	—[d]
U–B[e]	0.23–0.46[b]	≥ 0.34[c]	0.17 –0.28	0.22–0.28	—[d]

[a] No examples have been measured.

[b] Additionally $4.60\ (B-V) - 3.17 \leq (U-B) \leq (B-V) - 0.27$. Type U allowed 0^{m}02 inside limits when only *UBV* photometry is available.

[c] Additionally $B-V \geq (U-B)/7.0 + 0.74$; $1.70\ (B-V) - 1.12 \leq (U-B) \leq (B-V) - 0.33$; $(U-V) \leq 1.47$. Type U allowed 0^{m}02 inside limits, except for the last, when only *UBV* photometry is available.

[d] $(U-V) \geq 1.47$.

[e] Type U always allowed for $U-B \leq 0.28$, when only *UBV* photometry is available.

allows slight overlap of the M class with the S and C classes.

Figures 4 and 5 display the spectrophotometric parameters *BEND* and *DEPTH* versus albedo. Generally these parameters are more useful for mineralogical interpretations, and for the identification of exceptional objects as discussed below, than for direct type classification of the general population. *DEPTH*, for example, may be used to distinguish between pyroxene-rich and pyroxene-poor objects of type S.

UBV colors for 464 objects are illustrated in Fig. 6. Objects classifiable on the basis of albedo-sensitive data are denoted by special symbols, and their colors are used to establish the class boundaries illustrated in Fig. 7. The corners of these boundaries are projected as *limits* of *U–V* in Figs. 1 and 3.

Classification by *UBV* photometry alone clearly has limitations. S types may generally be classified unambiguously, except near the somewhat artificial boundary with the poorly defined R type (the boundary is also poorly defined in albedo, and may not represent any physical discontinuity). For small color indices the domains of types C, M, and E are degenerate. This region also contains some of the Trojans (not plotted here) and may contain other, unrecognized types; neutral colors can be produced by any transition-metal-free silicate, or by any material with sufficient opaque content to suppress spectral features. Thus we always allow the description U when classification is based on *UBV* data alone and $U-B \leq 0.28$.

Due to noise in the data for the fainter objects in Fig. 6, the C and S domains are drawn considerably broader than initially defined by Zellner *et al.* (1975, 1977b), and may contain unusual objects. For example, we have quite a few asteroids near $B-V = 0.77$, $U-B = 0.33$, none of which are independently classifiable from other data at present. Hence, when only *UBV* data are available, we generate the designations CU or SU when the colors fall within 0^{m}02 of the outer type boundaries, and allow the unambiguous types C or S only within the shaded areas in Fig. 7.

The M and especially the E domains are still poorly defined in color, and no spectrophotometry has been published for any proven E object. Thus, we always generate the designation EU for putative E objects in the absence of albedo or P_{min}. In Fig. 7 we extend the E domain to $B-V = 0.60$ to include several small objects in the Nysa dynamical family in the expectation that they are also of type E. Domains of type E

in Figs. 2, 4, and 5 are drawn on the expectation of a flat, featureless spectrum. Such a spectrum, not yet included in TRIAD, has been observed by Chapman and coworkers for 750 Oskar in the Nysa family.

IV. ADOPTED TYPES AND DIAMETERS

Table II lists computer-generated type classifications for 521 objects. The second column lists the type(s) allowed according to Table I. The four digits in the final column indicate the total observational weights of radiometric, polarimetric, *UBV*, and spectrophotometric data; code zero indicates no data. (Weights can total as much as 6 or 9 for *UBV* and spectral data because there are multiple parameters for those categories.) Assigned types should be considered provisional unless both albedo-sensitive data (first two digits) and spectral data of some kind (last two digits) are available. For less completely observed asteroids, more than one type may be allowed. The designation "CMEU," for instance, means the asteroid could be of type C, M, or E, and the "U" indicates its *UBV* colors fall in an ambiguous portion of the *UBV* plane, as described in Section III. When multiple types are allowed, they are listed in the order CSMERU (roughly, common to uncommon types).

The third column of Table II lists diameters derived from

$$2 \log D = 6.244 - 0.4[B(1, 0) - (B - V)] - \log p_V,$$

where D is the diameter in kilometers (Zellner *et al.*, 1974). $B(1, 0)$ is taken from the TRIAD magnitude file (maintained by T. Gehrels) and B–V from the TRIAD color file or else assumed from the type in the relatively few cases for which the color is unknown. Diameters listed without qualification are generated from measured polarimetric or radiometric albedos, or the weighted average of the two, if the total weight is 2 or higher. Values followed by an asterisk (*) are generated on the basis of unambiguous C, M, or S classifications with assumed visual albedos of 0.037, 0.12, or 0.14, which are typical of those respective classes, or on the basis of the classifications CU, SU, and SM which are sufficiently unambiguous so that assigned albedos of 0.037 for CU and 0.14 for SU and SM are probably close to their true values. Such diameters are probably more reliable than a single noisy radiometric or polarimetric determination, and are quite adequate for statistical purposes (Zellner and Bowell, 1977). Diameters followed by a question mark are based on the following albedo assumptions, which give only a very rough indication of size. Multiple classifications that begin with "C" are assigned $p_v = 0.037$ as the most probable albedo; those that begin with "M", $p_v = 0.12$; those that begin with "S," $p_v = 0.14$. Classifications EU and RU are assigned $p_v = 0.14$ and classification U, $p_v = 0.1$. Diameters listed with question marks are unlikely to be in error by more than a factor of three, but they should be treated as only crude guesses.

In the fourth column of Table II, we list orbital element zones similar to those of Kresak (1977) and defined in Table III. Note that, while the Hildas and Trojans were not used to define our classes, they are nevertheless classified in Table II. Well-observed Trojans are usually rejected from the main-belt compositional classes and hence designated U. If observed by only one or two techniques, they may be listed as C, MEU, CMEU, etc. The available evidence (Cruikshank, 1976; Degewij *et al.*, 1978) argues for a rather high degree of homogeneity among the Trojans.

V. APPLICATION OF TAXONOMY: EXAMPLES AND DISCUSSIONS

Examples

Several examples serve to illustrate the application of our classification procedure. We begin with a typical, thoroughly observed C asteroid, 19 Fortuna; the observa-

TABLE II

ASTEROID CLASSIFICATIONS AND DIAMETERS[a]

ASTEROID	TYPE	DIAMETER		ZONE	DATA	ASTEROID	TYPE	DIAMETER		ZONE	DATA
1	U	1020		II	3367	53	C	97	*	II	0056
2	U	630		Z	3257	54	C	177		II	2340
3	S	248		II	2659	55	CMEU	172	?	II	0040
4	U	549		I	3549	56	C	143		II	2240
5	S	122		II	2559	57	S	109	*	III	0120
6	S	195		I	2359	58	C	97	*	II	0147
7	S	210		I	3647	59	CMEU	166	?	II	0020
8	S	153		I	2549	60	S	51		I	2046
9	S	153		I	3457	61	S	87	*	III	0060
10	C	450		III	3256	62	C	104	*	III	0040
11	S	152		I	2547	63	S	89		I	3469
12	S	135		I	2267	64	E	57		II	2550
13	C	241		II	3267	65	C	308		IV	2250
14	S	154		II	3469	66	C	76	*	II	1040
15	S	246		II	2149	67	S	62	*	I	1040
16	M	252		III	3267	68	S	125		II	3157
17	S	97		I	2247	69	U	134	?	III	0127
18	S	152		I	2647	70	C	154		II	2240
19	C	221		I	3253	71	S	115	*	II	0130
20	S	137		I	2450	72	C	92	*	I	1050
21	M	112		I	3367	75	CMEU	94	?	II	0040
22	M	178		III	2367	76	CMEU	143	?	IV	0060
23	S	115		II	2156	77	M	62	*	II	1040
24	C	210	*	III	0157	78	C	140	*	II	0060
25	S	65		I	2069	79	S	75		I	2069
26	S	91	*	II	0020	80	U	86		I	2147
27	S	116		I	2169	81	C	112	*	III	0040
28	S	122	*	II	1107	82	S	65		II	2067
29	S	194		II	2359	83	C	106	*	I	0120
30	S	91		I	2447	84	C	82		I	2236
31	CM	333	?	III	0100	85	U	146		II	2149
32	S	93	*	II	0266	86	C	108	*	III	0040
33	S	56	*	III	0020	87	CMEU	225	?	IV	0040
34	C	114	*	II	1050	88	C	207		II	2157
36	C	103	*	II	1020	89	S	169		II	2229
37	S	93		II	2150	90	C	124	*	III	0040
39	S	164		II	1349	91	C	105		II	2060
40	S	121		I	2449	92	U	151	?	III	0240
41	C	177		II	2160	93	C	168		II	2206
42	S	97		I	2460	94	C	190		III	2040
43	S	77	*	I	1040	95	C	166	*	III	1140
44	E	72		I	2360	97	M	94		II	2056
45	C	228		II	2060	100	SU	80	*	III	0020
46	C	134		II	3160	101	S	67	*	II	0050
47	C	135	*	III	1000	102	C	84	*	II	0020
48	U	148	?	III	0047	103	S	90	*	II	1060
49	C	179	*	III	0040	104	C	122	*	III	0040
51	U	158		I	2247	105	C	124	*	I	1000
52	C	290		III	2057	106	C	169	*	III	1030

[a] Asteroid diameters listed with question marks (?) could be in error by a factor of 3. They are crude guesses and should be treated as such (see text).

TABLE II—*Continued*

Asteroid	Type	Diameter		Zone	Data
107	C	210	*	IV	1040
108	S	60	*	III	0046
109	C	75		II	2000
110	C	170	*	II	0060
111	C	143	*	II	0060
113	S	47		I	2040
114	C	122	*	II	0120
115	S	93		I	2247
116	SR	80		II	2100
117	CMEU	139	?	III	0040
119	S	57	*	II	0057
120	C	175		III	2040
121	C	197	*	IV	0130
122	CU	140	*	III	0020
123	S	49	*	II	1040
124	S	68		II	2040
125	U	64	?	II	0020
126	S	40	*	I	0040
129	M	115		III	2260
130	U	121	?	III	1047
131	SM	35		I	2000
133	S	79	*	III	0040
134	C	116	*	II	0040
135	M	79		I	2140
136	CMEU	65	?	I	0020
137	C	143	*	III	1040
139	C	140	*	II	1207
140	C	102		II	3027
141	C	115	*	II	0307
144	C	133		II	2040
145	C	175	*	II	0207
146	C	131	*	II	1040
147	CMEU	102	?	III	0020
148	S	106	*	II	0040
149	U	25	?	I	0040
150	CMEU	129	?	III	0020
151	S	41	*	II	0030
152	S	64	*	III	0030
153	U	100	?	III	0120
155	CMEU	30	?	II	0030
156	C	103	*	II	0050
158	S	36	*	III	0040
159	C	134		III	2040
160	C	90	*	II	0030
161	CMEU	79	?	I	0040
162	C	97	*	III	0040
163	C	66	*	I	0047
164	C	102	*	II	0060
165	C	203	*	III	0030
166	U	38	?	II	0047
168	C	134	*	IV	0040
170	U	41	?	II	0007
171	C	123	*	III	0040
172	S	67		I	2050
173	C	163	*	II	0040
175	C	113	*	III	0040
176	U	72	?	III	0007
177	C	67	*	II	0020
178	S	39	*	I	0040
179	S	72	*	III	0040
181	S	79	*	III	0037
182	S	48	*	I	1240
183	S	33	*	II	0040
184	U	72	?	III	0020
185	C	168	*	II	0040
186	U	46		I	2020
187	C	117	*	II	0020
189	S	42		I	2020
192	S	94		I	3569
194	C	193		II	2047
195	C	92	*	III	0040
196	S	160		III	2067
197	S	36	*	II	0020
198	S	66	*	I	0030
200	CME	121	?	II	0006
201	CMEU	133	?	II	0020
202	S	79	*	III	0020
203	C	92	*	II	0030
204	S	51	*	II	1020
205	C	97	*	II	0020
206	C	101	*	II	0040
207	C	58	*	I	0040
208	S	43		III	2020
209	CMEU	121	?	III	0040
210	C	77	*	II	0006
211	C	167		III	2060
213	EU	46	?	II	0007
214	MU	44	?	II	0040
216	CMEU	219	?	II	0050
218	S	53	*	II	0020
219	SM	38	*	I	1000
221	U	97	?	III	0049
224	M	59	*	II	1060
230	S	114		I	3559
233	SU	62	*	II	0020
234	S	44	*	I	0020
235	S	59	*	III	0040
236	S	65	*	II	0040
238	C	153		III	2020
240	C	99	*	II	0040
241	C	179	*	III	1060
245	S	72	*	III	0040
246	RU	51	?	II	0020
247	C	143		II	3040
250	CMEU	192	?	III	0060
258	S	66	*	II	0040

TABLE II—*Continued*

Asteroid	Type	Diameter		Zone	Data	Asteroid	Type	Diameter		Zone	Data
259	CMEU	152	?	III	0020	374	S	51	*	II	0120
260	C	81	*	IV	0020	375	C	183	*	III	0040
262	U	15	?	II	0020	376	S	39	*	I	0040
264	S	64		II	2040	377	CMEU	95	?	II	0040
268	C	106	*	III	0020	378	S	30	*	II	0020
270	S	50		I	2100	381	C	127		III	2020
271	C	59	*	III	0030	383	C	61	*	III	0020
275	C	94	*	II	0040	384	S	36	*	II	0040
276	CMEU	107	?	III	0050	386	C	174		III	2020
279	MEU	60	?	Z	0030	387	S	113		II	2050
281	U	15	?	I	0040	388	CMEU	120	?	III	0040
284	C	53	*	I	0050	389	S	70	*	II	0140
286	C	85	*	III	0020	390	U	30	?	II	0020
293	C	59	*	III	0050	393	C	121		II	2050
295	S	27	*	II	0040	395	C	49	*	II	0040
302	CMEU	38	?	I	0040	397	S	50		II	2050
305	S	46	*	III	0040	402	S	46	*	II	0026
306	S	53	*	I	0140	404	C	94	*	II	1040
308	U	137		II	2060	405	C	102	*	II	0040
312	SU	47	*	II	0020	407	C	83	*	II	0040
313	C	92	*	I	1040	409	C	208	*	II	0047
324	C	251		II	3256	410	C	124	*	II	1240
325	CMEU	105	?	III	0020	413	CEU	52	?	II	0020
326	C	82	*	I	1046	415	C	74	*	II	1120
329	C	66	*	I	0020	416	S	76	*	II	0150
333	C	77	*	III	0020	418	CMEU	61	?	II	0040
334	C	180	*	HI	0220	419	EU	62	?	II	0020
335	EU	49	?	I	0057	422	CMEU	41	?	I	0040
336	MEU	34	?	I	0020	423	C	174	*	III	0140
337	CS	100	?	I	0007	426	C	104	*	III	0020
338	M	58	*	III	0100	432	S	45	*	I	0040
342	C	53	*	II	0040	433	S	16		A	3669
344	C	146	*	II	0040	434	E	11		HU	2150
345	C	90	*	I	0240	435	CMEU	52	?	I	0050
346	S	87	*	II	0040	439	CMEU	65	?	III	0020
349	R	145		III	2249	441	M	61		II	2050
350	C	122	*	III	0040	444	C	143	*	II	1050
351	S	45	*	II	0040	446	R	48	*	II	0007
352	S	26	*	I	0040	447	U	47	?	III	0020
354	U	169		II	2247	451	C	327		III	3150
356	C	150		II	2166	454	C	84	*	II	0030
357	C	105	*	III	0040	455	C	101	*	II	1000
359	C	75	*	II	0020	462	U	41	?	III	0037
360	C	130		III	2020	471	S	149		III	2260
361	CU	112	*	HI	0020	472	S	45	*	II	0040
362	C	90	*	II	0040	476	C	103	*	II	1000
363	C	95	*	II	0040	478	S	75	*	III	0040
364	SMR	32	?	I	1000	480	S	52	*	II	0040
365	C	100		II	2060	481	C	101	*	II	0007
367	S	20	*	I	0100	487	S	68	*	II	0020
369	CMEU	114	?	II	0040	489	C	119	*	III	0030
370	C	43	*	I	0020	490	C	127	*	III	0030
373	CU	83	*	III	0020	497	M	38	*	III	1020

TABLE II—*Continued*

Asteroid	Type	Diameter		Zone	Data	Asteroid	Type	Diameter		Zone	Data
498	C	73		II	2040	679	S	43		II	2020
505	ME	50	?	II	0009	680	CMEU	69	?	III	0040
506	C	109	*	III	0020	686	S	35	*	II	0020
508	C	126	*	III	0040	689	C	21	*	I	0020
509	S	60	*	III	0060	690	CEU	160	?	III	0040
510	CMEU	62	?	II	0040	691	C	73	*	III	0020
511	C	341		III	3347	692	S	46	*	IV	0040
516	M	64		II	2060	694	C	90	*	II	1000
517	C	79	*	III	0050	697	C	65	*	III	0020
521	C	104	*	II	0020	702	C	205	*	III	0050
522	CEU	92	?	IV	0020	704	C	339		III	2167
524	C	61	*	II	0040	705	CMEU	117	?	III	0040
525	RU	8.4	?	I	0020	712	C	133	*	II	0060
530	CMEU	81	?	III	0030	714	S	46	*	II	0046
532	S	230		II	3349	716	U	23	?	II	0030
533	S	34	*	III	0030	727	U	35	?	II	0020
535	C	72	*	II	0030	729	U	45	?	II	0020
537	C	98	*	III	1000	731	C	73	*	III	0040
540	S	19	*	I	0020	733	CMEU	87	?	IV	0020
545	C	108	*	III	0030	735	C	68	*	II	0040
546	CU	63	*	II	0040	737	S	54	*	II	1200
550	S	41	*	II	1020	739	U	64	?	II	0057
554	C	103	*	I	1037	744	U	33	?	III	0020
558	SM	66		III	2000	747	C	205		III	2240
563	S	53	*	II	1156	750	EU	12	?	I	0020
566	CMEU	140	?	IV	0040	751	C	105	*	II	0030
569	C	54	*	II	0030	754	C	81	*	III	0040
570	CU	90	*	IV	0030	755	MEU	37	?	III	0040
572	C	41	*	I	0040	760	SU	61	*	III	0030
584	S	55		I	2446	762	CEU	109	?	III	0030
588	MEU	61	?	I	0050	764	C	71	*	III	0040
589	C	95	*	III	0040	770	SU	21	*	I	0040
591	MU	23	?	II	0040	776	C	174	*	III	0050
596	U	134		III	2020	778	EU	36	?	III	0040
602	C	138		III	2160	782	SM	15	*	I	1000
613	U	35	?	III	0020	785	U	45		II	2050
616	S	23	*	II	0030	790	C	177		IV	2040
617	U	89	?	I	1030	796	C	88	*	II	0020
618	C	126	*	III	0040	804	C	162	*	III	1060
623	C	35	*	I	0030	824	S	29	*	II	0020
624	U	111	?	I	1146	825	S	13	*	I	0050
626	C	84	*	II	0020	830	S	41	*	III	0020
628	U	49	?	II	0020	847	S	26	*	II	0020
631	S	49	*	II	0040	849	M	73	*	III	0140
635	CU	81	*	III	0020	853	C	29	*	I	0030
642	SU	29	*	III	0030	857	U	19	?	I	0020
643	CU	64	*	IV	0040	860	SM	36	*	II	1000
645	S	33	*	III	0030	863	R	50	*	III	1030
647	CMEU	28	?	I	0040	883	S	8.5	*	I	0020
654	U	72	?	I	0137	884	MU	52	?	I	0020
658	SU	24	*	III	0020	887	U	5.2		A	2327
660	SM	40	*	II	1000	888	S	36	*	II	0060
674	S	97	*	III	1147	899	CEU	54	?	III	0040

TABLE II—*Continued*

Asteroid	Type	Diameter	Zone	Data	Asteroid	Type	Diameter	Zone	Data
911	U	94 ?	I	0066	1326	U	22 ?	II	0020
924	C	77 *	III	0020	1329	SU	19 *	II	0030
925	S	61 *	II	0030	1330	MU	28 ?	III	0020
927	C	78 *	III	0020	1341	CMEU	42 ?	II	0040
932	C	56 *	I	0040	1359	C	43 *	III	0020
944	CMEU	39 ?	Z	0020	1362	C	31 *	IV	0040
946	C	46 *	III	0060	1390	MU	47 ?	IV	0040
963	S	9.2*	I	0030	1391	RU	9.8?	II	0030
966	S	30 *	II	0020	1392	MEU	14 ?	II	0020
969	EU	9.1?	I	0040	1401	S	10 *	I	0040
976	CMEU	75 ?	III	0020	1437	CMEU	126 ?	I	0040
977	C	67 *	III	0020	1453	RU	8.4?	HU	0040
978	CMEU	67 ?	III	0030	1456	C	36 *	III	0020
980	S	77 *	II	0030	1461	MEU	35 ?	III	0020
991	C	39 *	III	0020	1467	C	116 *	IV	0040
1001	MEU	38 ?	III	0040	1474	EU	8.2?	A	0040
1004	U	40 ?	IV	0020	1493	EU	16 ?	I	0020
1011	S	7.2	I	2040	1500	S	6.8*	I	0020
1013	CU	60 *	II	0020	1504	S	13 *	I	0020
0115	C	90 *	III	0040	1512	U	45 ?	HI	0020
1019	U	9.6?	HU	0040	1529	MU	30 ?	HI	0020
1023	U	38 ?	III	0040	1547	U	24 ?	II	0040
1031	C	70 *	III	0040	1566	U	1.7?	A	0120
1036	S	39 *	A	0060	1567	C	76	III	2020
1043	S	34 *	III	0020	1580	C	6.5*	A	0240
1048	C	70 *	II	0060	1583	MEU	61 ?	I	0030
1052	S	12 *	I	0120	1595	U	14 ?	II	0020
1058	SR	13 ?	I	0100	1602	RU	8.8?	I	0020
1079	SU	20 *	III	0030	1620	S	2.4*	A	0140
1088	RU	16 ?	I	0030	1621	S	14 *	I	0020
1093	C	95 *	III	0020	1627	S	7.0*	A	0040
1102	C	77 *	III	0020	1639	C	37 *	II	0040
1127	C	37 *	II	0030	1658	RU	14 ?	II	0030
1140	S	26 *	II	0040	1669	CU	36 *	III	0020
1143	EU	62 ?	I	0030	1681	S	14 *	II	0030
1162	SU	40 *	HI	0020	1685	U	7.6?	A	0049
1171	CMEU	65 ?	III	0040	1693	U	22 ?	II	0030
1172	C	128 *	I	1000	1694	C	17 *	I	0040
1173	C	87 *	I	1000	1702	MU	19 ?	III	0020
1178	C	24 *	II	1000	1707	SU	8.7*	I	0020
1212	CMEU	239 ?	HI	0040	1755	S	20 *	III	0020
1224	SU	14 *	I	0020	1765	CMEU	58 ?	III	0020
1235	CU	15 *	HU	0020	1792	C	22 *	II	0020
1241	CU	74 *	III	0020	1830	S	8.9*	I	0020
1245	U	36 ?	III	0020	1864	U	3.3?	A	0040
1251	U	26 ?	II	0020	1867	CMEU	117 ?	I	0020
1252	SU	18 *	Z	0020	1916	S	2.9*	A	0020
1263	C	42 *	II	0020	1931	C	12 *	II	0020
1266	C	78 *	IV	0020	1952	C	49 *	III	0020
1268	CMEU	92 ?	HI	0020	2000	S	15 *	I	0040
1275	C	40 *	II	0020	2061	CU	9.5*	A	0020
1306	S	36 *	III	0020	2062	U	0.9	A	2020
1314	S	8.5*	I	0020	1977RA	SU	2.4*	A	0040
1317	C	58 *	III	0020					

tional parameters are given in Table IV. The *UBV* colors fall within the C domain of Fig. 6, and the albedo of 0.030 and the P_{min} of 1.72 also clearly place Fortuna in the low-albedo C class. Of the spectrophotometric parameters, *BEND* allows either C or S, *R/B* allows C, M, or E, and the absence of the pyroxene absorption band (*DEPTH* = 1.00) serves only to exclude membership in class R. Thus the classification would be ambiguous if only the spectrophotometric parameters were available, but is clearly tied down by both *UBV* colors and the albedo-sensitive observations.

As an example of an S object, Table IV also lists the parameters for 5 Astraea. This classification could be made unambiguously from *UBV* colors alone or from *R/B* alone. The other parameters are consistent with the S classification, but none considered alone is sufficient; the albedo allows types S or M, P_{min} and *DEPTH* allow S or R, and *BEND* any type except R. For the S asteroids, *UBV* colors are particularly diagnostic.

Asteroid 44 Nysa in Table IV is a prototype E object. The high albedo and small P_{min} suggest E but by themselves are also consistent with our limits for class R. The *UBV* colors fall within the ambiguous domain allowing C, M, E, or U but not S or R. Thus both color and albedo data are required to place an object uniquely in class E, and the only proven E objects are 44 Nysa, 64 Angelina, and 434 Hungaria.

Perhaps the most prominent example of an unclassifiable asteroid is 4 Vesta. In Table IV the relatively high albedo allows classes R or (just barely) S or M, but the very unusual P_{min} of 0.55 excludes types S and M. The spectrophotometric parameters *BEND* and *R/B* exclude type R, however, and the *UBV* colors fall outside the domains of any of the recognized classes. Thus Vesta can be classified only as U.

Summary of Results

In Table II we identify 190 C objects, 141 of the S type, 13 of type M, 3 of type E, and 3 of type R. The classification U is obtained for 55 objects or 11% of the sample, while 118, or 23%, receive ambiguous classifications. The latter are principally of three types: designations CMEU, CEU, MEU, EU, MU, or RU for 80 objects, from *UBV* data or incomplete spectrophotometry alone; SU or CU from *UBV* results on the fringes of the S and C domains (26 objects) and SM or SMR from albedo data without accompanying colors or spec-

TABLE III

ORBITAL ELEMENT ZONES

Zone	Description	Criteria[a]	Number in TRIAD	Number classified
A	Apollo–Amor	$q = a(1 - e) \leq 1.65$	48	13
HU	Hungarias	$1.82 \leq a \leq 2.00$ $e \leq 0.15$ $i \geq 16°$	16	4
I	Main belt	$2.06 \leq a < 2.50$ $e \leq 0.35$ $i \leq 30°$	532	105
II	Main belt	$2.50 \leq a < 2.82$ $e \leq 0.35$ $i \leq 30°$	572	200
III	Main belt	$2.82 \leq a < 3.27$ $e \leq 0.35$ $i \leq 30°$	769	159
IV	Main belt	$3.27 \leq a \leq 3.65$ $e \leq 0.35$ $i \leq 30°$	46	19
HI	Hildas	$3.80 \leq a \leq 4.20$ $e \leq 0.35$ $i \leq 30°$	27	8
T	Trojans	$5.06 \leq a < 5.30$ no test no test	21	11
Z	Exceptional	——None of the above——	16	4

[a] Tests are made for zone membership in the order indicated, using the osculating elements semimajor axis a, eccentricity e, and inclination i. Divisions in the main belt correspond to Kirkwood gaps at the $\frac{1}{3}$, $\frac{2}{5}$, and $\frac{1}{2}$ resonances with respect to the motion of Jupiter.

TABLE IV

FOUR EXAMPLES OF CLASSIFICATION

Asteroid	Type	Parameters							
		B–V	*U–B*	*BEND*	*R/B*	*DEPTH*	p_V	P_{min}	Type
19 Fortuna	C	0.75	0.38	0.21	1.09	1.00	0.03	1.72	√
	S			0.21		1.00			
	M				1.09	1.00			
	E				1.09	1.00			
	R								
5 Astraea	C			0.10					
	S	0.83	0.38	0.10	1.63	0.84	0.144	0.70	√
	M			0.10			0.144		
	E			0.10					
	R					0.84		0.70	
44 Nysa	C	0.71	0.26						
	S								
	M	0.71	0.26						
	E	0.71	0.26				0.467	0.31	√
	R						0.467	0.31	
4 Vesta	C			0.14	1.33				
	S			0.14			0.226		
	M				1.33		0.226		
	E			0.14	1.33				
	R					0.74	0.226	0.55	
	(U)	0.78	0.48				——		√

trophotometry (7 objects). In each case future observations by a complementary technique will usually suffice to permit an unambiguous classification.

The soundness of our classification approach is demonstrated by the fact that, of 163 asteroids observed by both albedo-sensitive and spectrally sensitive techniques, no ambiguous classifications are returned, and only 21 objects are classified U. However, we should note that we are subject to a limitation common to any classification scheme applied to inhomogeneous data: Objects are likely to be assigned to familiar types (C, S, M) when relatively few parameters are available, but subsequently recognized as unusual after more complete study. For example, the U objects 51 Nemausa, 85 Io, and 654 Zelinda would be allowed as C types, and 80 Sappho, 887 Alinda, and 1685 Toro as S objects, except for the spectrophotometric parameter *BEND*. Since *BEND* is available for only 20% of the asteroids classified here, there are certain to be additional such examples among the apparently secure classifications.

In the above statistics the C objects are much underrepresented, of course, because of their low albedos and generally larger semimajor axes. The E and R types, however, must be genuinely quite rare. Zellner and Bowell (1977) have noted that in the whole main belt there appear to be only two E objects with diameters >50 km. Additional candidates in Table II are asteroids 59, 87, 216, 250, 259, and 690, all observed by *UBV* photometry alone. Most of them are probably of types C or M, but all should be prime candidates for future polarimetry or thermal radiometry.

Unusual Asteroids

Several unusual objects deserve special comment. Objects 4 Vesta, 349 Dembowska, 69 Hesperia, 785 Zwetana, and 863 Benkoela are truly exceptional, and recognizable as such by almost any technique. For the latter three, the mineralogy remains to be inferred, and they may ultimately serve as prototypes for new classes. In our sample, asteroids 149 Medusa, 1023 Thomana, and 1326 Losaka may possibly be of the Vesta type, in which case all three would have diameters <25 km; the tiny Apollo object 1566 Icarus, not observed since 1968 (Gehrels *et al.*, 1970), also shows some similarities to Vesta.

Pallas is C-like in some respects and M-like in others, but clearly unclassifiable. Asteroid 1 Ceres is loosely describable as a C-type, but has a rather high albedo (0.054, versus 0.03–0.04 for typical C objects) and an unusual spectrum with uncommonly reddish $U-B$ and uncommonly neutral R/B colors. Thus Ceres is now formally designated as a U object, and should not in any case be thought of as a prototype for the C class. Among the six largest asteroids (Morrison, 1977b), Ceres, Pallas, and Vesta are unclassifiable, 704 Interamnia has unique polarimetric properties not reflected in our classification parameters (Zellner and Gradie, 1976), and 31 Euphrosyne has been observed only in $P_{\min}$, with Pallas-like results. Thus the true C-dominated asteroid population may be regarded as involving asteroids of about 300 km and smaller.

An extensive survey of faint asteroids in the Hirayama families 2 (Eos) and 3 (Koronis) by UBV and radiometric techniques is in progress (Gradie and Zellner, 1977; Gradie *et al.*, 1977). The data are for the most part not yet in TRIAD, hence not included in our figures and tables.[2] The Koronis objects seem to belong mostly, if not exclusively, to a subset of the S type. The Eos asteroids are more problematical, and form a distinct population for which our taxonomic system seems poorly designed. In albedo and color they range from the C to the S domains, though generally outside the main body of either, as shown by the ellipse in Fig. 1. The spectrum of 221 Eos itself observed by McCord and Chapman (1975b) is unusual and leads to a U or "unclassifiable" designation.

V. COMPARISON OF ASTEROID CLASSIFICATION SYSTEMS

Taxonomy—or classification based upon observational criteria—is an important phase of many young sciences. Classification schemes aid our understanding of the physical processes that give rise to observed differences. As in any taxonomy, the number of classes and subclasses into which the entire sample is divided is largely arbitrary. Biologists still debate the widely used biological taxonomy. Sometimes, when there is partial understanding of the nature and origin of different classes, it is difficult to keep taxonomy from being influenced by physical hypotheses; while an "intelligent" taxonomy based upon the best available models can be particularly helpful for elucidating those models, it can also be misleading if the models are incorrect. In this section we discuss relations to other classification systems and some of the problems related to interpretation of asteroid mineralogical assemblages.

It has been recognized for some years (e.g., Hapke, 1971) that there are several clumps in plots for asteroids of $U-B$ versus $B-V$. The first extensive asteroid taxonomy was based on narrowband spectrophotometry by Chapman (1971) and Chapman *et al.* (1973). That work not only preceded

[2] Several Eos and Koronis objects omitted in this paper are included in Table I of Zellner and Bowell (1977). They also listed data for asteroids 154, 372, 560, 579, 675, 779, 801, and 1636, which are still in a preliminary stage of reduction and are not yet in TRIAD or this paper.

any substantial progress in understanding the mineralogical implications of the spectra, but also preceded recognition of the common occurrence of the dark asteroids now called "C-types." Three broad groups were defined, primarily in terms of overall color such as the R/B parameter used in the present paper. The R-class asteroids (R for "reddish," not related to our present, much redder R type) were divided into four groups, two of which were further subdivided into five subgroups; all asteroids formerly designated "R" fall into the present broad S class. Two other classes (M for medium or intermediate color and F for flat or neutral-colored spectrum) were each subdivided into four groups; into these sparsely populated groups were placed the several known examples of what we now call C and M asteroids, and a couple of anomalous objects such as Vesta. This system has not been used subsequently and is now of purely historical interest.

In subsequent papers, McCord and Chapman (1975a,b) attempted to recognize all "significantly different" spectral types among the 93 good quality spectra from their sample of 98 asteroids. Within the observational errors, 34 different spectra were recognized. Some of the differences are quite minor and could be due to slightly different proportions of the same suite of major minerals (e.g., iron, pyroxene, and olivine).

More recently, there have been two attempts to classify asteroid spectra by considering the mineralogically significant elements of the spectra, that is, by explicitly incorporating the compositional interpretations. Chapman (1976) grouped the 34 distinct spectral types distinguished by McCord and Chapman (1975a,b) into 13 broader groups, most of which have a high degree of interpreted mineralogical commonality. For instance, two of the McCord–Chapman spectral types are interpreted as being due chiefly to the signatures of nickel–iron plus olivine while another two were grouped as both suggesting a C2 (CM) carbonaceous chondritic composition. Several of the 13 groups could not be readily interpreted by Chapman, so they were described with other descriptive terms, such as "Trojans," "intermediate," or "lunar-soil-like" (the latter, shown in Table V merely by "?," does not necessarily indicate a compositional similarity with the Moon).

Even more recently, Gaffey and McCord (1977a,b) have developed a separate classification for 62 of the McCord–Chapman spectra, emphasizing interpretations of mineralogical assemblages. Fifteen groups were defined, mostly consisting of subdivisions of several broader groups symbolized by R (for moderately reddish spectra, both with and without prominent 1.0-μm absorption features), T (for transition), and F (for flat).

We will now compare the Chapman and Gaffey–McCord classification schemes with each other and with the CSM taxonomy of the present paper. Thereby we may gain an appreciation for the present state of the art of asteroid mineralogical interpretation and for the strengths and weaknesses of the CSM taxonomy. Reference is made to Table V, which is arranged, very roughly, from neutral spectra to very red spectra. The first column lists type asteroids for each of the 34 McCord–Chapman spectral types (those sampled early in the observing program were first classified by Chapman *et al.*, 1973, by the letters shown in quotes to the left). The brackets group the 34 spectral types into the 13 mineralogical groupings of Chapman (1976) (column 2). Corresponding groups of Gaffey and McCord (1977a,b) are shown in parentheses. Column 3 illustrates the correspondence between the groupings of column 2 and the CSM taxonomy of the present paper. The final columns give the mean R/B, $B-V$, and geometric albedos for each of the 34 types represented in the TRIAD file by at least two asteroids or, if in parentheses, by one asteroid.

TABLE V

COMPARISON OF TAXONOMIES

	Type Example	Mineralogical class	This paper	N	Average parameters		
					R/B	*B–V*	p_V
	213	C* (F + TB)	mostly C	1	(1.04)	—	—
	2			2	1.01	0.64	(0.08)
	10			3	1.09	0.67	0.04
"F"	88			1	(1.14)	(0.67)	(0.045)
	511			2	1.19	(0.71)	0.03
	1			2	1.03	0.74	0.04
"M2"	324	C2 (TA + TC)		16	1.13	0.71	0.04
	51			6	1.25	0.75	(0.05)
"M1"	16	Metal or enstatite chon. (RR)	M	1	(1.21)	(0.70)	(0.09)
	21			3	1.10	0.71	0.11
	22			2	1.27	0.71	0.09
	43	Intermediate (various T)	(U)	1	(1.20)	(0 73)	—
	166			3	1.41	0.74	(0.03)
"M3"	4	Achondrite (eucrite)	(U)	1	(1.33)	(0.78)	(0.23)
	69 (?)			1	(1.31)	(0.69)	—
	624	Trojan		2	1.45	0.77	0.04
	9	Metal-rich [plus silicate?] (RF)		8	1.57	0.85	0.13
"R1"	12			4	1.63	0.87	0.13
"R2"	7	Metal + olivine (RA-1)		3	1.58	0.83	0.15
	39			2	1.82	0.92	0.15
"R3C"	29	Metal plus pyroxene (RA-2 + TE)	mostly S	1	(1.41)	(0.84)	(0.14)
"R3A, B"	6			3	1.47	0.83	(0.16)
	3			10	1.62	0.85	0.14
	230			1	(1.51)	(0.87)	(0.10)
	25			2	1.79	0.91	0.15
	89	Pyroxene-rich plus metal (RA-3)		3	1.51	0.85	0.12
	5			1	(1.63)	(0.83)	(0.14)
	63			1	(2.07)	(0.91)	(0.13)
	446			1	(2.64)	—	—
	8	Metal-poor, opaque-poor (various)	(U)	1	(1.79)	(0.88)	(0.14)
	1685			1	(1.70)	(0.88)	—
	349			1	(1.72)	(0.97)	(0.26)
	170	?		1	(1.70)	—	—
	80	[carb. ?] chon. 3 (TD)	(U)	2	1.84	0.90	0.10

In general there is an excellent agreement between the Chapman and Gaffey–McCord groupings. Usually the rather minor differences are due to somewhat noisy data or to spectra falling near the boundaries of the defined groups. Several of the classifications require discussion, however. First, Gaffey and McCord have placed four of the asteroids in Chapman's 3 Juno group in a "TE" group, whereas the remainder are called "RA." Chapman can perceive little detectable differences between the "TE" and "RA" asteroids and interprets all to be metal plus pyroxene assemblages. Gaffey agrees that the "RA" group consists of metal plus pyroxene (with perhaps minor olivine), but has a radically different interpretation for the "TE" group: type 3 carbonaceous chondrites. The distinction, if valid, would be especially important cosmochemically inasmuch as the metal–pyroxene assemblages imply geochemical differentiation whereas the C3 meteorites are deemed to be unaltered primitive condensates. We are doubtful about the validity of the "TE" designation for two reasons: first, there appears to be no distinction among other measured parameters (e.g., albedo) for the four "TE" asteroids and other S-type asteroids, in our taxonomy. Second, several "TE" asteroids are known to have polarimetric properties quite different from C3 chondrites (Zellner *et al.*, 1977c). This example provides a general warning about the subtleties of interpreting asteroid spectra in terms of mineralogy and about the insensitivity of even reasonably precise classification schemes, not to mention broader schemes such as our own, to the possibility of distinctions of major geochemical importance.

Another potential problem concerns asteroids of possible metallic composition. Our M-type is interpreted by both Chapman and by Gaffey–McCord as being *either* metal *or* metal plus neutral silicate (e.g., enstatite chondrites). For both interpretations, nickel–iron is the spectrally dominant component, but there is a great geochemical difference between the two. Nickel–iron asteroids almost certainly result from thermal processes and extensive geochemical separation, whereas enstatite chondrites are unaltered nebular condensates. A complicating factor is that Gaffey interprets another group of asteroids (those typified by 9 Metis in Chapman's classification, and included as S objects herein) as of iron or enstatite-chondritic composition. The spectra of these asteroids are clearly dominated by the signature of nickel–iron, but there is a pronounced flattening in the infrared. Chapman interprets the flattening as being caused by a broad, weak absorption feature due to either olivine or olivine-plus-pyroxene. Gaffey and McCord prefer interpretations avoiding olivine or pyroxene. If Gaffey and McCord are right, then asteroids of nickel–iron or enstatite-chondrite composition are distributed among both our M and S types, in spite of a wide gap in *UBV* colors between M and S objects.

A final question concerns the composition of the several distinct types of C asteroids. Among the asteroids classified C in this paper, Gaffey–McCord distinguish four types and Chapman distinguishes two (Chapman's C2-type comprises Gaffey–McCord's types TA and TC while Chapman's C*-type comprises Gaffey–McCord's types F and TB). Gaffey and McCord interpret their three types TA, TB, and TC as being analogous to C2 (CM) carbonaceous chondritic meteorites, among the most primitive of meteorites. But the F-type (most of Chapman's C*-type) is interpreted as a thermally evolved mineral assemblage—either a carbonaceous chondrite of high metamorphic grade (C4, like the meteorite Karoonda) or even as an opaque-rich basalt. Interpretation of C*-type spectra in terms of thermal evolution has been dealt a blow by Lebofsky (1977) who has measured a substantial absorption band near 3 μm due to water of hydration

in the spectrum of Ceres; this seems inconsistent with both C4 meteorites and basalts. It remains an open question what is responsible for the significant spectral differences between the C*- and C2-type spectra.

The foregoing discussion indicates the potential difficulties with using the CSM taxonomy carelessly. It remains possible that the straightforward interpretation of C-types as carbonaceous chondrites, M-types as metallic objects, and S-types as stony-irons is basically correct. But in the worst possible case, it may turn out that there is substantial heterogeneity in the cosmochemically important characteristics within the broad C, S, and M groups and that the mnemonics associated with the letters C, S, and M may be misleading.

The CSM taxonomy has certain strengths, however, which might be incorporated into subsequent attempts to classify asteroids mineralogically. The CSM taxonomy is strongly constrained by albedo, a parameter given great weight neither by Chapman nor by Gaffey and McCord. The albedos tabulated in the right-hand column of Table V indicate the consistency of the CSM taxonomy. Individual albedos among asteroids belonging to each one of the 34 groups distinguished by McCord and Chapman are generally self-consistent. But Gaffey and McCord's separation of groups RA2 (mean albedo 0.14) and TE (mean albedo 0.13) is not independently suggested by the albedo data. Furthermore the similar compositional interpretations by Gaffey and McCord for the RF type (mean albedo 0.12) and RR type (mean albedo 0.07) is perhaps rendered questionable by the significant albedo difference.

For one purpose, the CSM taxonomy is much superior to that employed by other authors. An end-product of any attempt at classifying asteroids is an examination of the differences in the size distributions and orbital distributions for the separate classes. Some of the discussions by Chapman (1976) and most of those by Gaffey and McCord (1977a,b) involve raw data, uncorrected for observational selection. Through its strict accounting of albedos, the CSM taxonomy permits a reasonable correction for bias to be applied to the available statistics, such as accomplished by CMZ (1975), Morrison (1977b), and Zellner and Bowell (1977). Through use of the albedos tabulated in Table V, it would be possible to apply such corrections to any of the mineralogical classes of McCord and Chapman, Chapman, or Gaffey and McCord.

Observational data on asteroids are continuing to accumulate. Moreover spectrophotometric measurements made during several previous years are being reduced, which will remove much of the present imbalance in the number of asteroids for which *R/B*, *BEND*, and *DEPTH* are available compared with other parameters. In about a year, sufficient data should be available to warrant a major analysis using the full power of multivariate, cluster analysis techniques, the utility of which has already been demonstrated for a subset of the CMZ asteroid sample by Pike (1978).

ACKNOWLEDGMENTS

This work has been supported by NASA grants to the University of Arizona and Lowell Observatory and by NASA Contract NASW-3134 to Planetary Science Institute. The TRIAD data file is supported at the University of Arizona by NASA Grant NSG-7249. This is Planetary Science Institute Contribution No. 91. We thank numerous colleagues for helpful criticisms of earlier versions of this paper.

REFERENCES

BENDER, D., BOWELL, E., CHAPMAN, C., GAFFEY, M., GEHRELS, T., ZELLNER, B., MORRISON, D., AND TEDESCO, E. (1978). The Tucson Revised Index of Asteroid Data. *Icarus* 33, 630–631.

CHAPMAN, C. R. (1971). Surface properties of asteroids. Ph.D. thesis, Massachusetts Institute of Technology, Cambridge, Mass.

CHAPMAN, C. R. (1976). Asteroids as meteorite parent-bodies: The astronomical perspective. *Geochim. Cosmochim. Acta* 40, 701–719.

CHAPMAN, C R., MCCORD, T. B , AND JOHNSON, T. V. (1973). Asteroid spectral reflectivities. *Astron. J.* 78, 126–140.

CHAPMAN, C. R., MORRISON, D., AND ZELLNER, B. (1975). Surface properties of asteroids: a synthesis of polarimetry, radiometry, and spectrophotometry. *Icarus* 25, 104–130. Herein called CMZ.

CHAPMAN, C. R., AND SALISBURY, J. W. (1973). Comparison of meteorite and asteroid spectral reflectivities. *Icarus* 19, 507–522.

CRUIKSHANK, D. P. (1976). Radii and albedos of Trojan asteroids and Jovian satellites 6 and 7. *Bull. Amer. Astron. Soc.* 8, 463.

CRUIKSHANK, D. P., AND MORRISON, D. (1973). Radii and albedos of asteroids 1, 2, 3, 4, 6, 15, 51, 433, and 511. *Icarus* 20, 477–481.

DEGEWIJ, J., GRADIE, J., AND ZELLNER, B. (1978). Minor planets and related objects. XXV. UBV photometry of 145 faint asteroids. *Astron. J.*, 83, 643–650.

GAFFEY, M. J., AND MCCORD, T. B. (1977a). Asteroid surface materials: mineralogical characterizations and cosmochemical implications. *Proc. 8th Lunar Sci. Conf.* I, 113–143.

GAFFEY, M. J., AND MCCORD, T. B. (1977b). Asteroid surface materials: mineralogical characterizations from reflectance spectra. *Space Sci. Rev.*, in press.

GEHRELS, T., ROEMER, E., TAYLOR, R. C., AND ZELLNER, B. H. (1970). Minor planets and related objects. IV. Asteroid (1566) Icarus. *Astron. J.* 75, 186–195.

GRADIE, J., RIEKE, G., AND ZELLNER, B. (1977). UBV and 10 micron photometric observations of Eos and Coronis family members. *Bull. Amer. Astron. Soc.* 9, 503.

GRADIE, J., AND ZELLNER, B. (1977). Asteroid families: Observational evidence for common origins. *Science* 197, 254–255.

HANSEN, O. L. (1976). Radii and albedos of 84 asteroids from visual and infrared photometry. *Astron. J.* 81, 74–84.

HANSEN, O. L. (1977). An explication of the radiometric method for size and albedo determination. *Icarus* 31, 456–482.

HAPKE, B. (1971). Inferences from optical properties concerning the surface texture and composition of asteroids. In *Physical Studies of Minor Planets* (T. Gehrels, Ed.), pp. 67–77. NASA SP-267.

JOHNSON, T. V., AND FANALE, F. P. (1973). Optical properties of carbonaceous chondrites and their relationship to asteroids. *J. Geophys. Res.* 78, 8507–8518.

JONES, T. J., AND MORRISON, D. (1974). Recalibration of the photometric/radiometric method of determining asteroid sizes. *Astron. J.* 79, 892–895.

KRESAK, L. (1977). Asteroid versus comet discrimination from orbital data. In *Comets, Asteroids, Meteorites—Interrelations, Evolution and Origins* (A. H. Delsemme, Ed.), pp. 313–321. Univ. of Toledo, Ohio.

LARSON, H. P., AND FINK, U. (1975). The infrared spectrum of asteroid 4 Vesta. *Icarus* 26, 420–424.

LEBOFSKY, L. A. (1977). Asteroid 1 Ceres Evidence for water of hydration. Submitted to *Mon. Not. Roy. Astron. Soc.*

MCCORD, T. B., ADAMS, J. B., AND JOHNSON, T. V. (1970). Asteroid Vesta: spectral reflectivity and compositional implications. *Science* 168, 1445–1447.

MCCORD, T. B., AND CHAPMAN, C. R. (1975a). Asteroids: Spectral reflectance and color characteristics. *Astrophys. J.* 195, 553–562.

MCCORD, T B., AND CHAPMAN, C. R. (1975b). Asteroids: Spectral reflectance and color characteristics. II. *Astrophys. J.* 197, 781–790.

MCCORD, T. B., AND GAFFEY, M. J. (1974). Asteroids: Surface compositions from reflection spectroscopy. *Science* 186, 352–355.

MORRISON, D. (1974). Radiometric diameters and albedos of 40 asteroids. *Astrophys J.* 194, 203–212.

MORRISON, D. (1977a). Radiometric diameters of 84 asteroids from observations in 1974–76. *Astrophys. J.* 214, 667–677.

MORRISON, D., (1977b). Asteroid sizes and albedos. *Icarus* 31, 185–220.

MORRISON, D., AND CHAPMAN, C. R. (1976). Radiometric diameters for an additional 22 asteroids. *Astrophys. J.* 204, 934–939.

PIETERS, C., GAFFEY, M. J., CHAPMAN, C. R., AND MCCORD, T. B. (1976). Spectrophotometry (0.33 to 1.07 μm) of 433 Eros and compositional implications. *Icarus* 28, 105–115.

PIKE, R. J. (1978). Statistical classification of asteroids from surface properties. *Lunar and Planetary Science* 9, 901–903.

TAYLOR, R. C. (1971). Photometric observations and reductions of lightcurves of asteroids In *Physical Studies of Minor Planets* (T. Gehrels, Ed.), pp. 117–131. NASA SP-267.

ZELLNER, B. (1975). 44 Nysa: An iron-depleted asteroid. *Astrophys. J.* 198, L45–L47.

ZELLNER, B., AND BOWELL, E. (1977). Asteroid compositional types and their distributions. In *Comets, Asteroids, Meteorites—Interrelations, Evolution and Origins* (A. H. Delsemme, Ed.), pp. 185–197. University of Toledo, Ohio.

ZELLNER, B., GEHRELS, T., AND GRADIE, J. (1974). Minor planets and related objects. XVI. Polarimetric diameters. *Astron. J.* 79, 1100–1110.

ZELLNER, B., WISNIEWSKI, W. Z., ANDERSSON, L., AND BOWELL, E. (1975). Minor planets and related objects. XVIII. UBV photometry and surface composition. *Astron. J.* 80, 986–995.

ZELLNER, B., AND GRADIE, J. (1976). Minor planets and related objects. XX. Polarimetric evidence for the albedos and compositions of 94 asteroids. *Astron. J.* 81, 262–280.

ZELLNER, B., LEAKE, M., MORRISON, D., AND WILLIAMS, J. G. (1977a). The E asteroids and the origin of the enstatite achondrites. *Geochim. Cosmochin. Acta* 41, 1759–1767.

ZELLNER, B., ANDERSSON, L., AND GRADIE, J. (1977b). UBV photometry of small and distant asteroids. *Icarus* 31, 447–455.

ZELLNER, B., LEAKE, M., LEBERTRE, T., DUSEAUX, M., AND DOLLFUS, A. (1977c). The asteroid albedo scale. I. Laboratory polarimetry of meteorites. *Proc. 8th Lunar Sci Conf.* 1091–1110.

ZELLNER, B., LEBERTRE, T., AND DAY, K. (1977d). The asteroid albedo scale. II. Laboratory polarimetry of dark carbon-bearing silicates. *Proc. 8th Lunar Sci. Conf.* 1111–1117.

APPENDIX II

Best Available Average Spectra
For All 250 Asteroids

6 Avg.
7 Avg.
8 Avg.
9 Avg.
10 Avg.
11 Avg.

18 Avg.
19 Avg.
20 Massalia
21 Avg.
22 Avg.

23 Avg.
24 Avg.
25 Avg.
26 Proserpina
27 Avg.

28 Avg.
29 Avg.
30 Avg.
31 Euphrosyne
32 Avg.

34 Circe
37 Fides
39 Avg.
40 Avg.
41 Daphne
42 Isis

43 Ariadne
44 Nysa
45 Eugenia
46 Hestia
48 Avg.

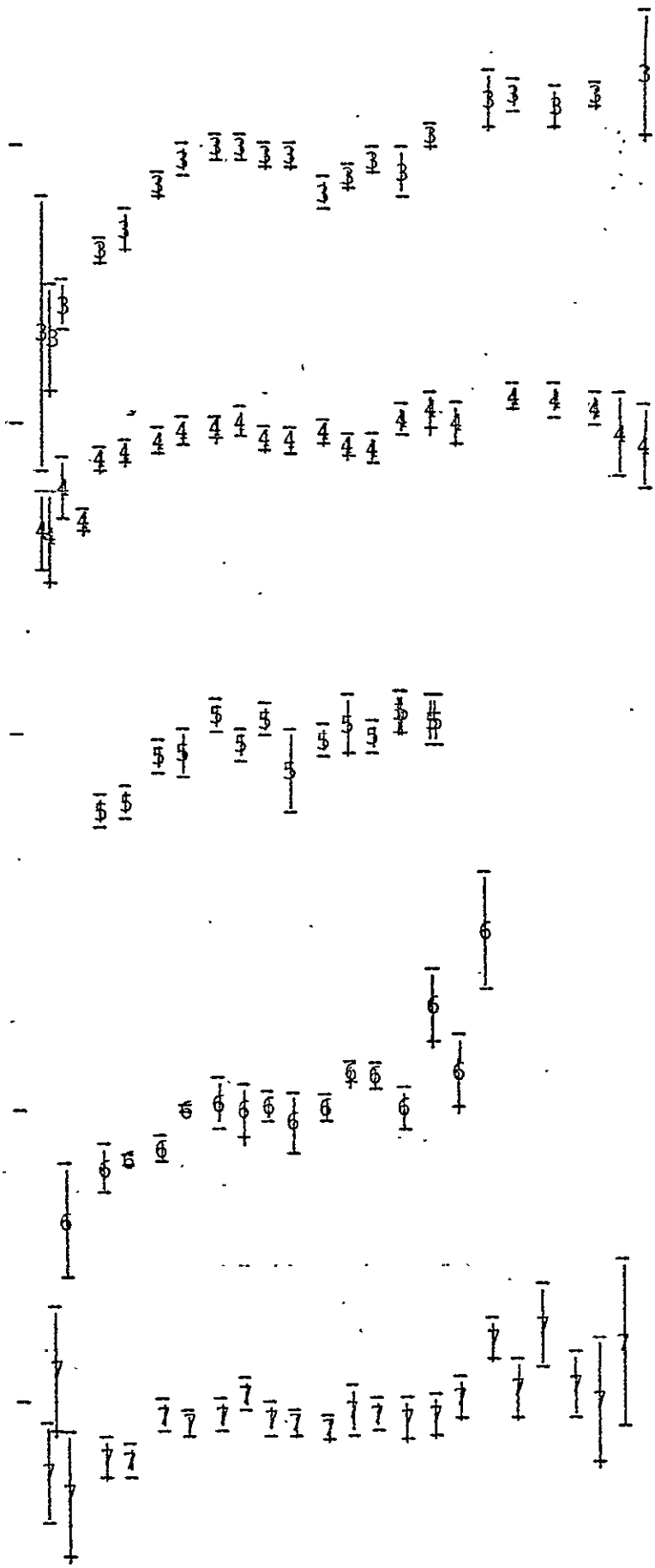

60 Avg.
62 Erato
63 Avg.
64 Angelina
65 Cybele

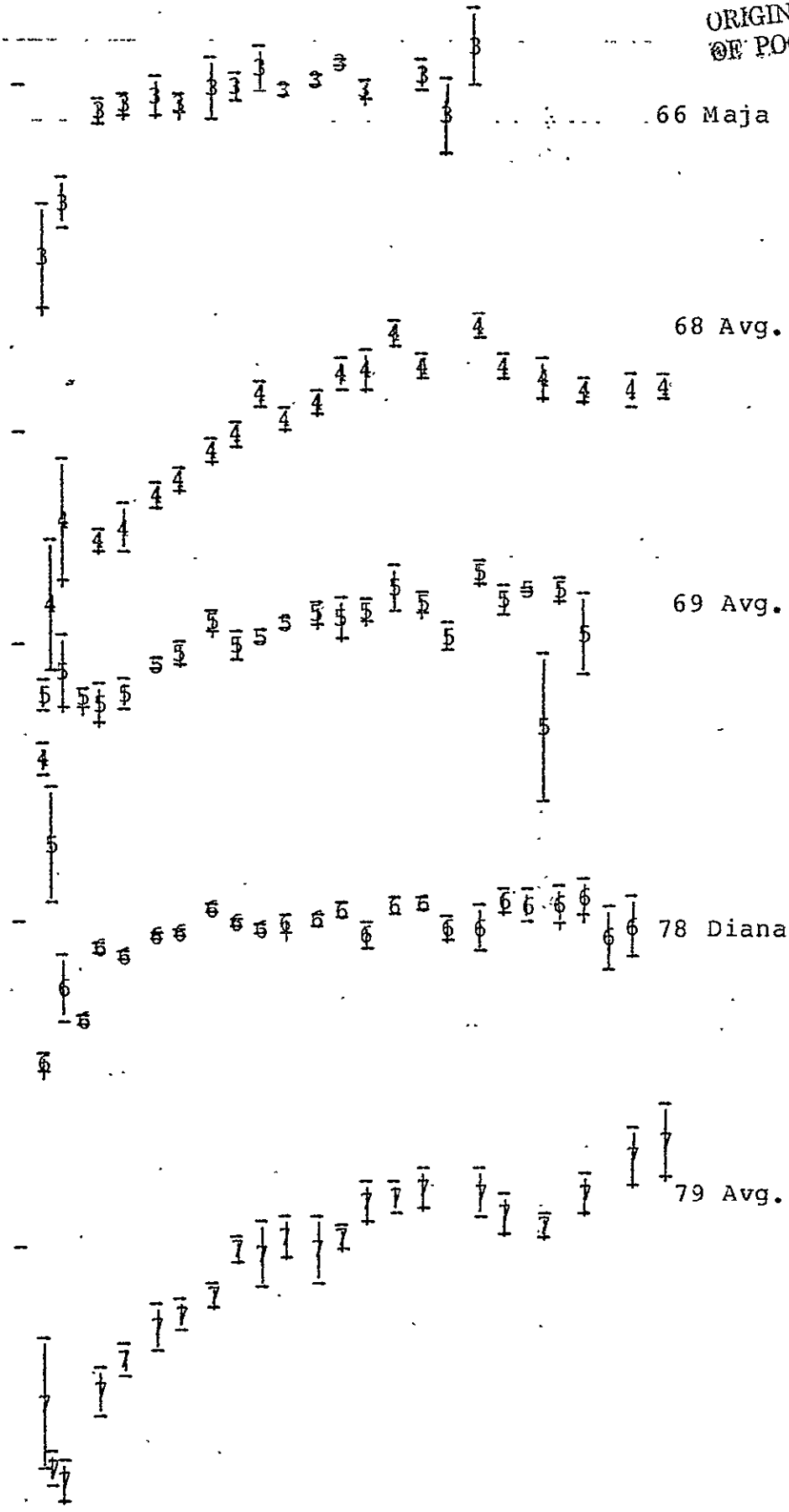

80 Avg.
82 Avg.
83 Beatrix
84 Avg.
85 Avg.

87 Sylvia
88 Avg.
89 Avg.
90 Antiope
92 Undina

93 Avg.
94 Aurora
97 Avg.
105 Artemnis

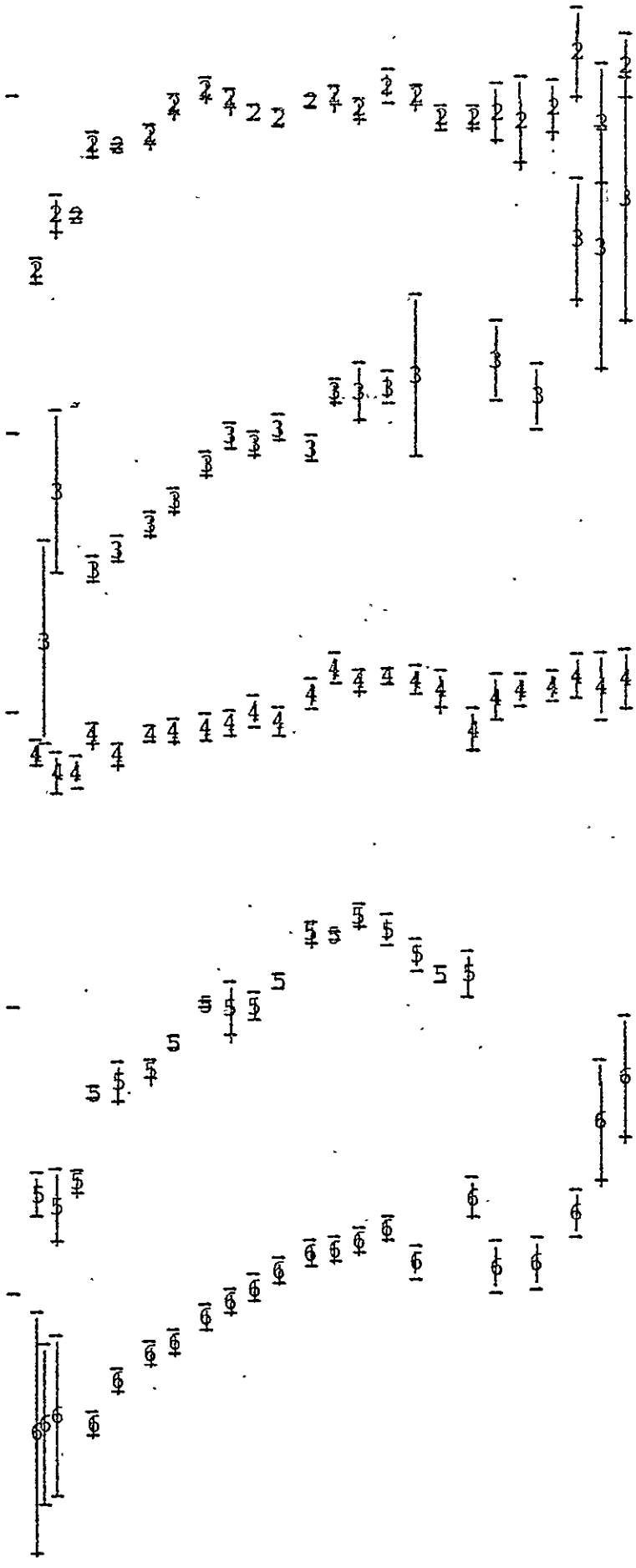

119 Avg.
121 Hermione
122 Gerda
124 Alkeste
128 Nemesis

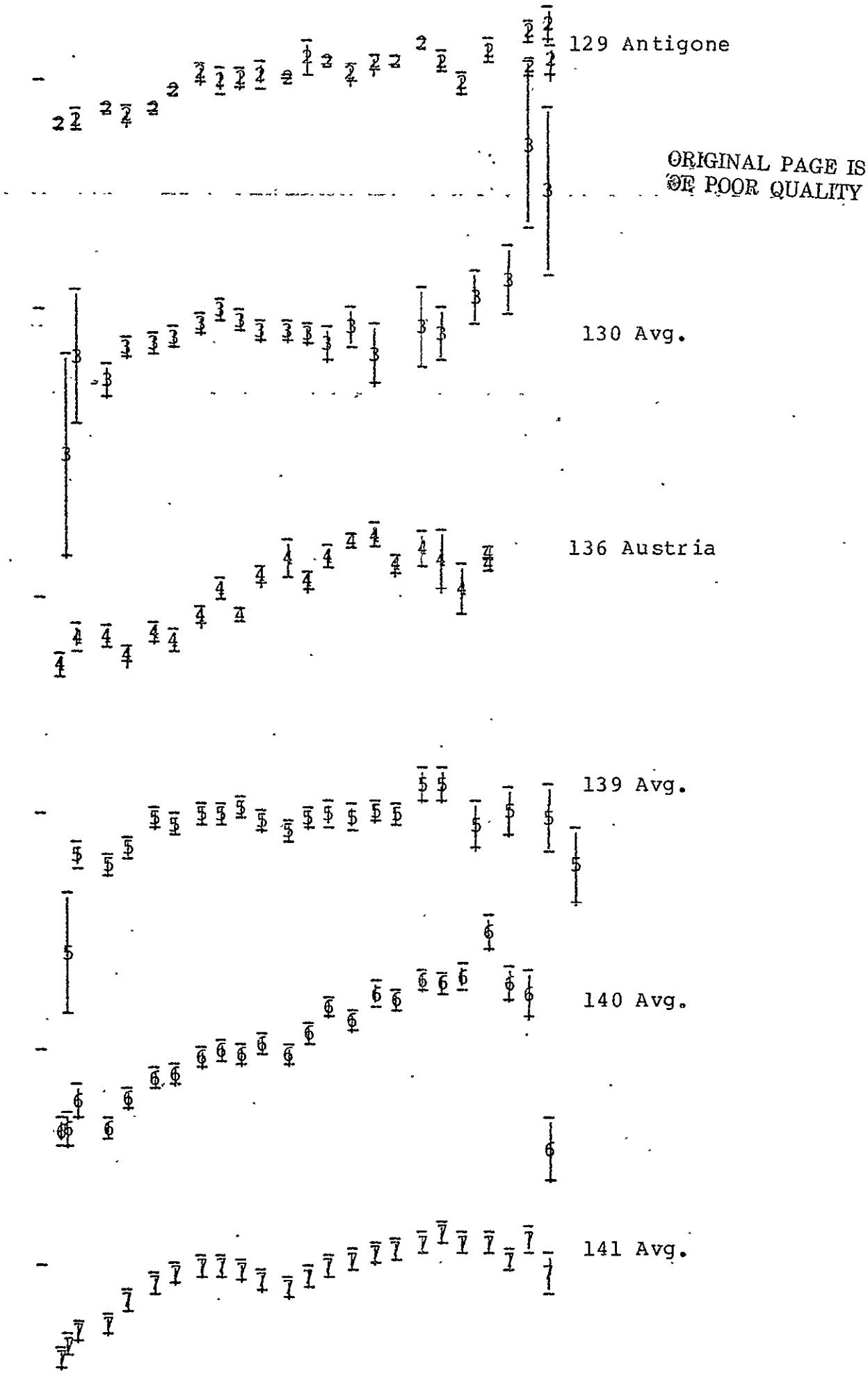

144 Vibilia
145 Avg.
149 Medusa
150 Nuwa
156 Xanthippe
158 Koronis

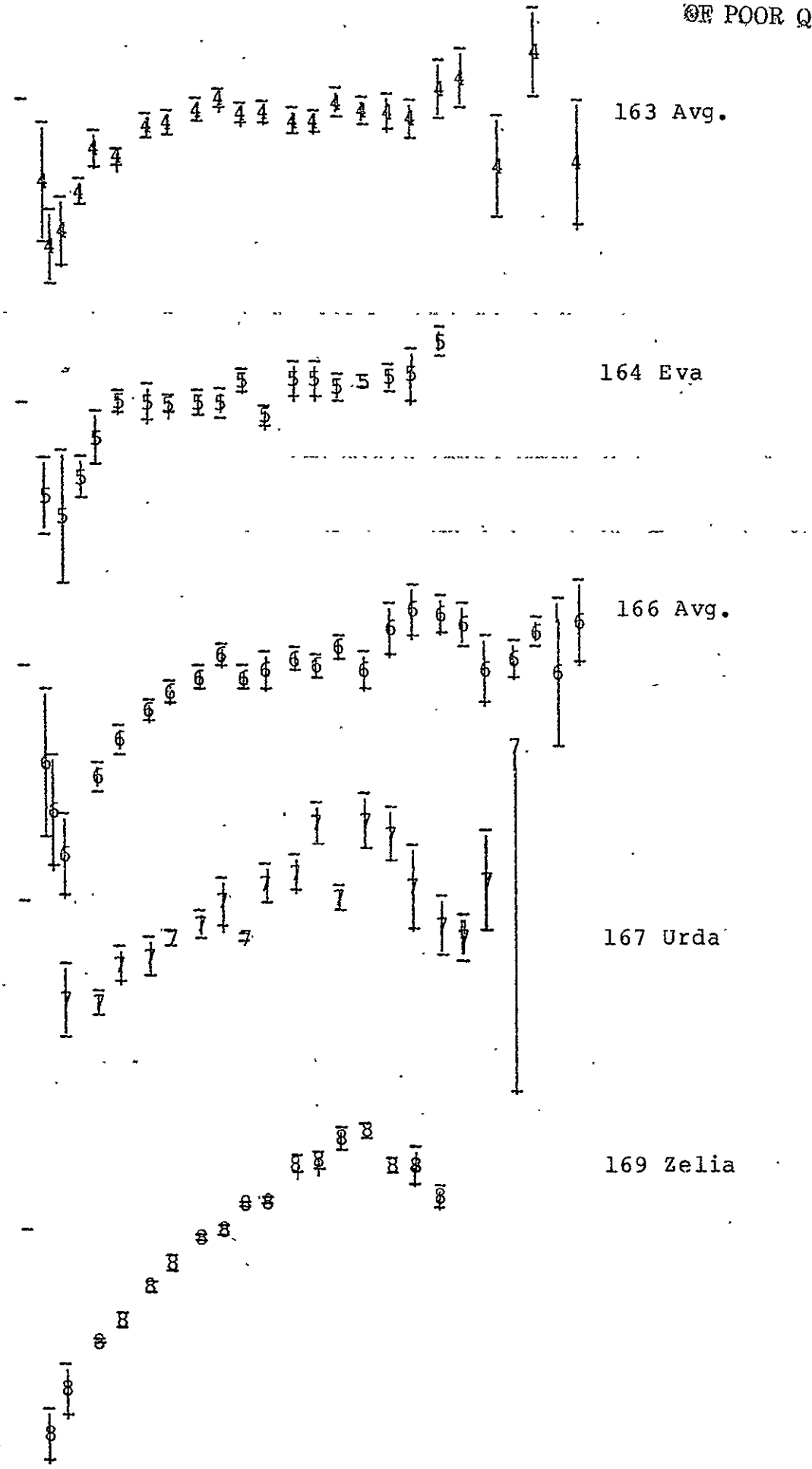

170 Avg.
175 Andromache
176 Avg.
181 Avg.
192 Avg.
194 Avg.

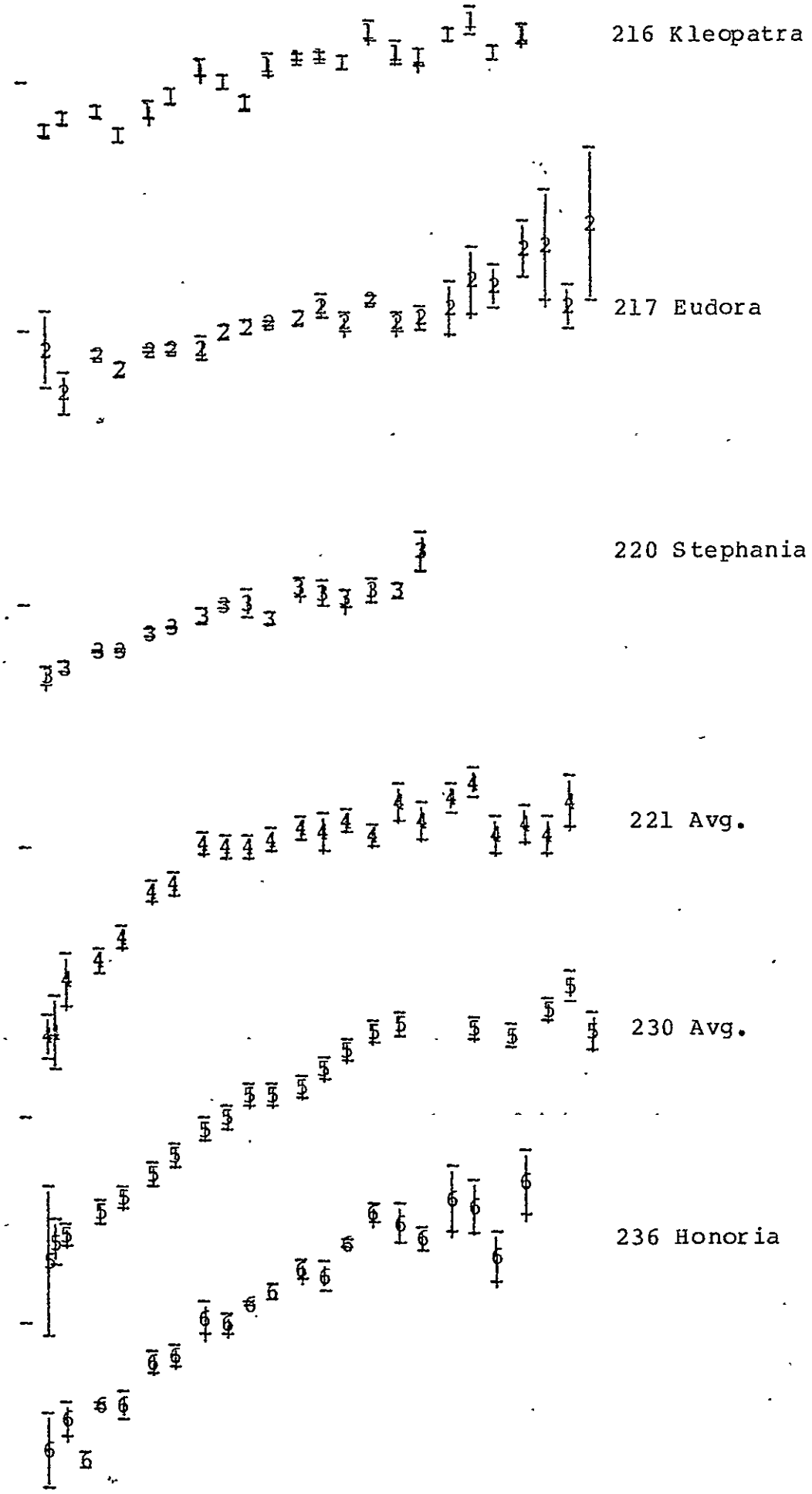
216 Kleopatra
217 Eudora
220 Stephania
221 Avg.
230 Avg.
236 Honoria

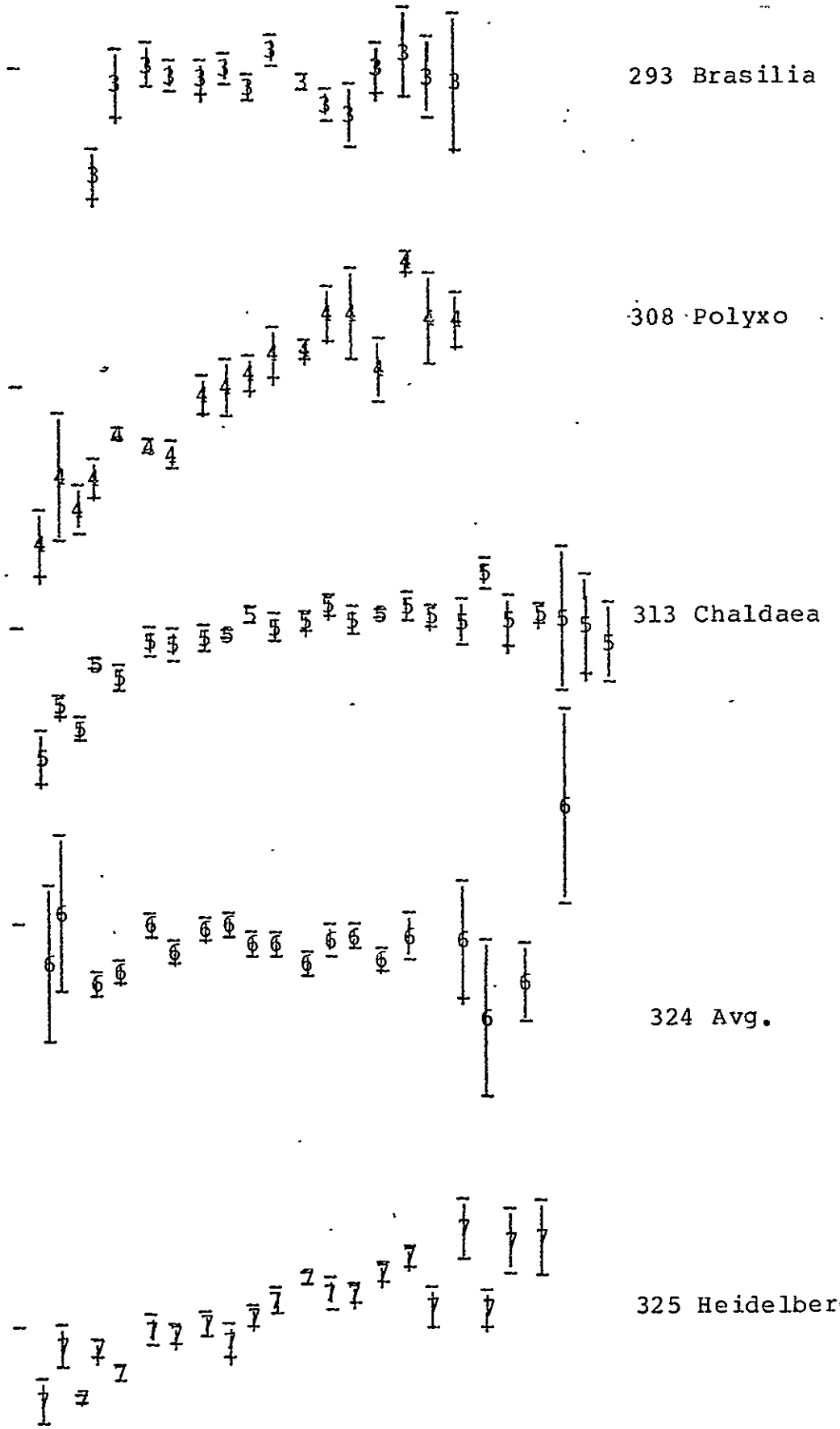
293 Brasilia
308 Polyxo
313 Chaldaea
324 Avg.
325 Heidelberga

326 Avg.

335 Avg.

337 Avg.

338 Budrosa

339 Dorothea

340 Eduarda
341 California
344 Desiderata
345 Tercidina
347 Pariana

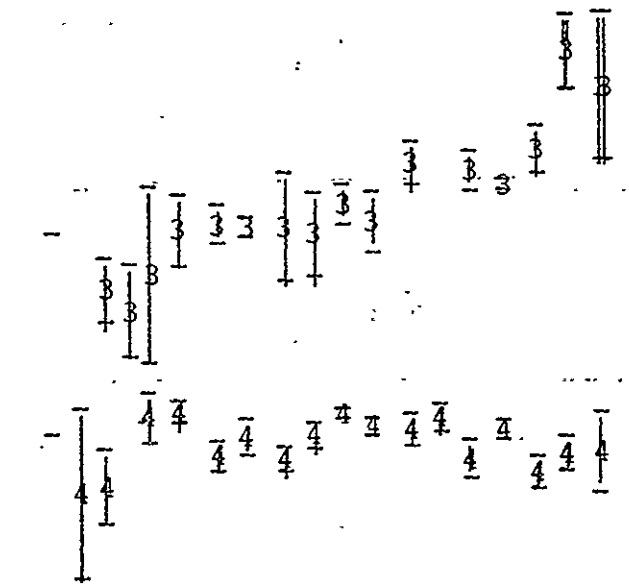

365 Corduba

372 Palma

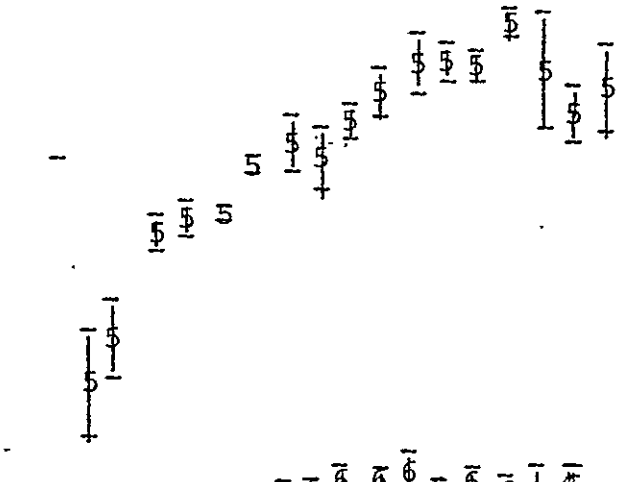

374 Burgundia

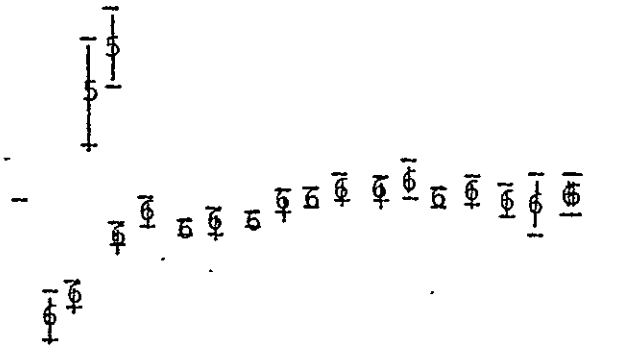

375 Ursula

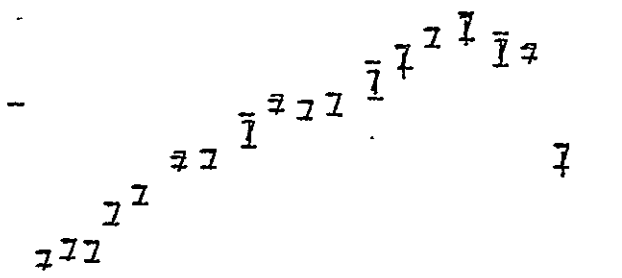

389 Indestria

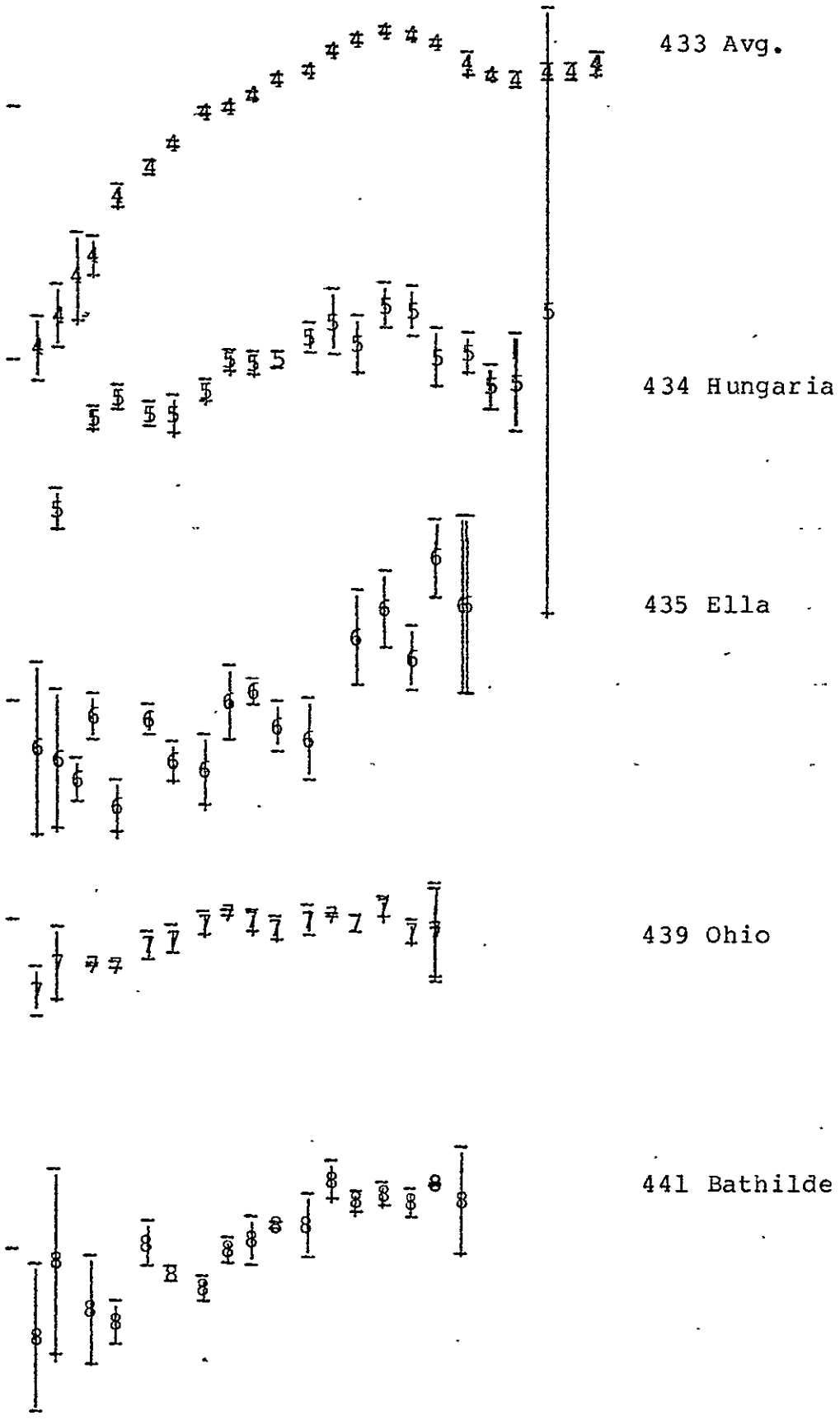
433 Avg.
434 Hungaria
435 Ella
439 Ohio
441 Bathilde

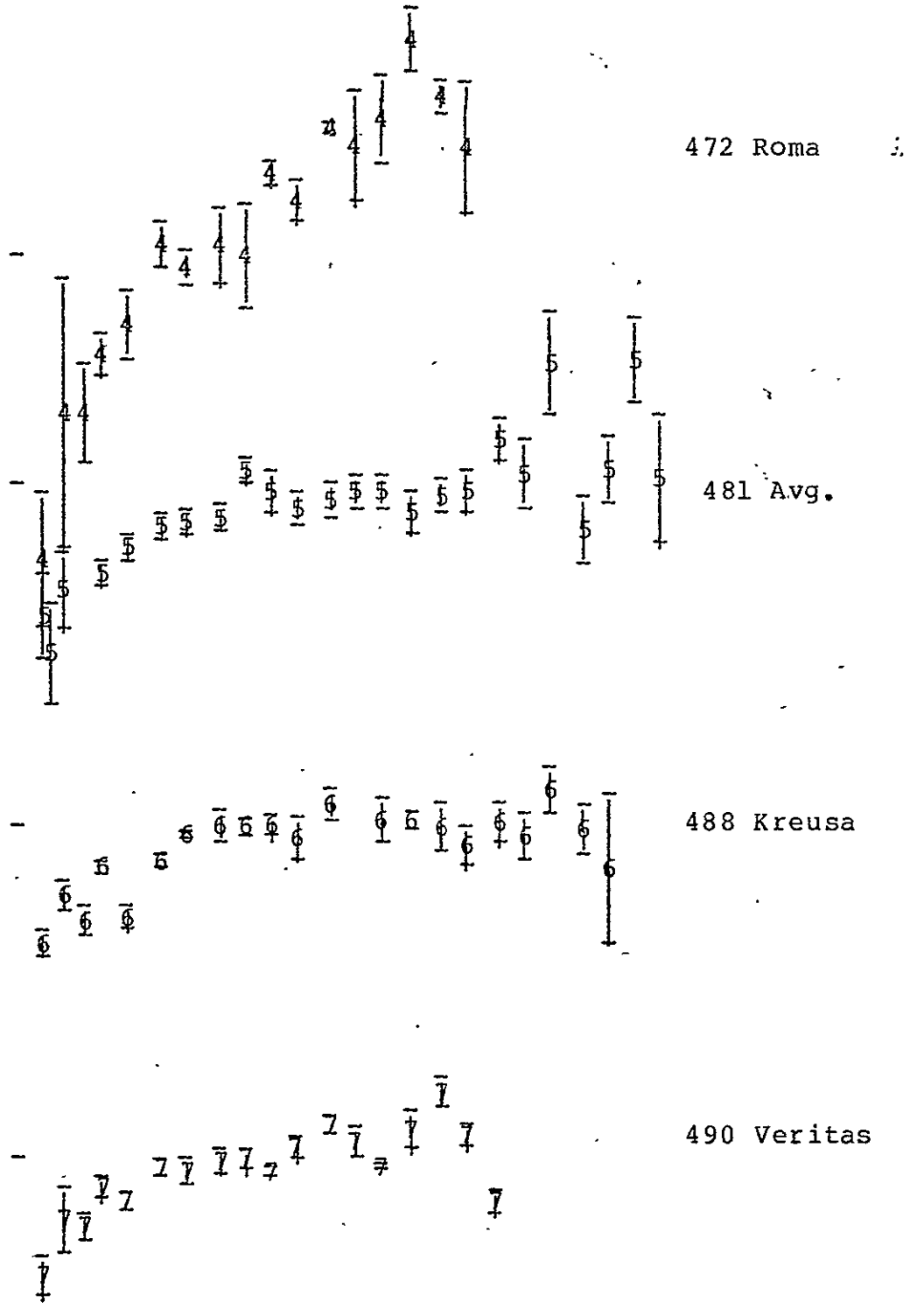
472 Roma
481 Avg.
488 Kreusa
490 Veritas

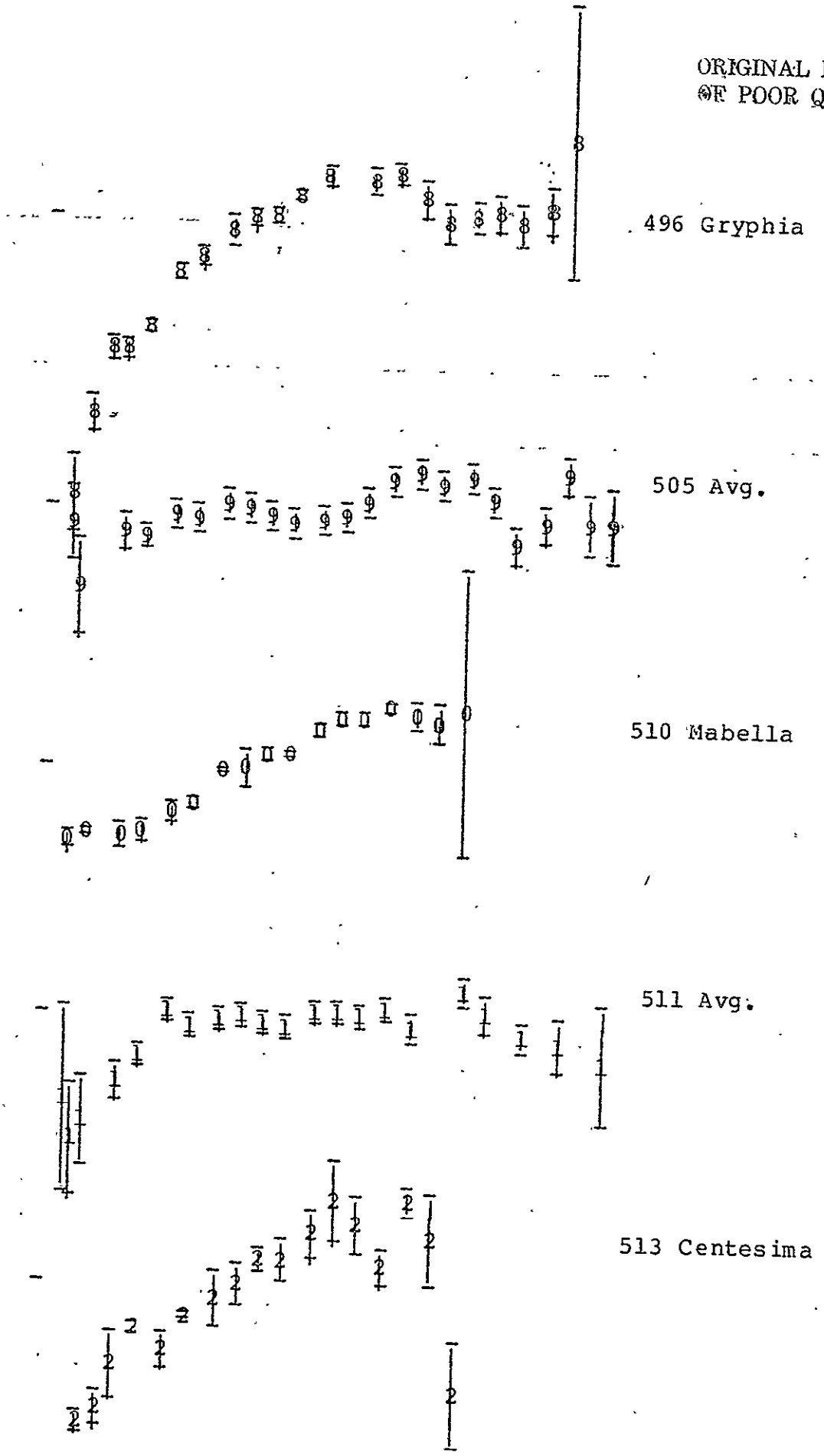

526 Jena

532 Avg.

554 Avg.

558 Carmen

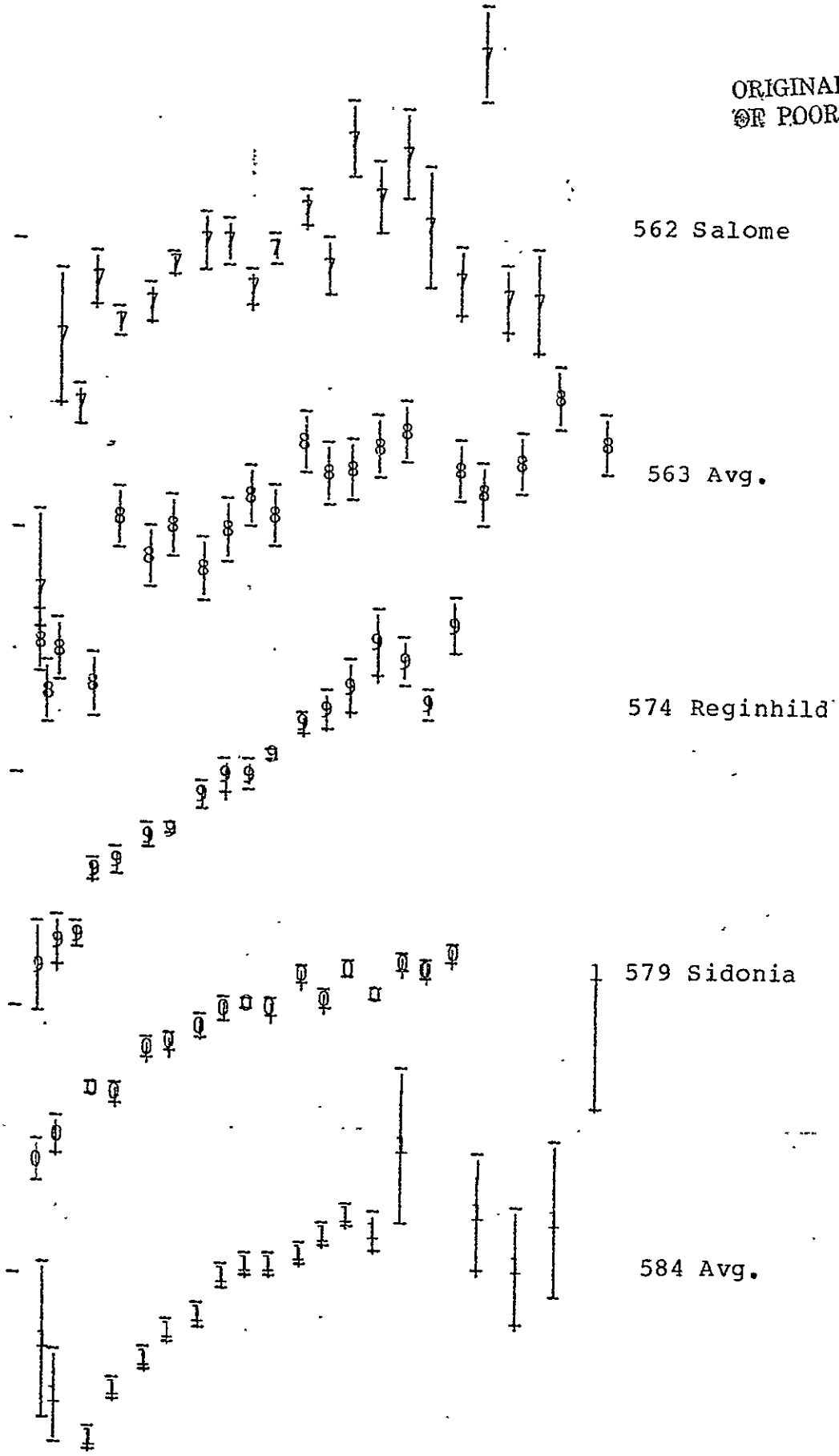

C-2

588 Achilles

599 Luisa

613 Ginevra

617 Patroclus

624 Avg.

628 Christine

648 Pippa

654 Avg.
660 Crescentia
674 Avg.
695 Bella
696 Leonora

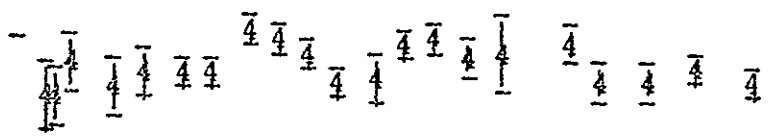

704 Avg.

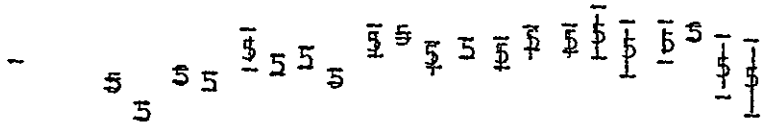

712 Boliviana

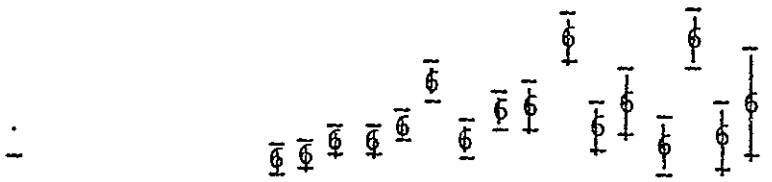

714 Avg.

739 Avg.

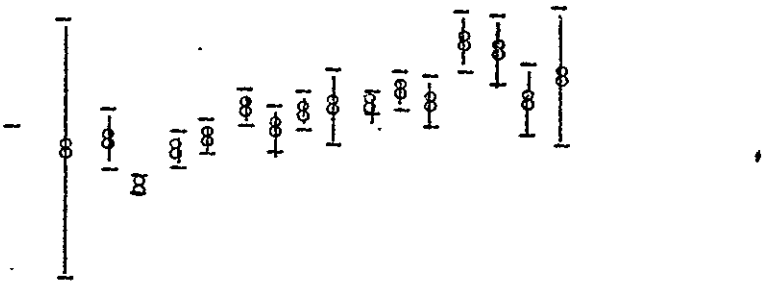

741 Botolphia

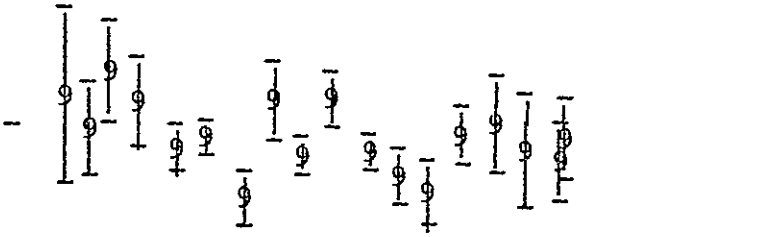

750 Oskar

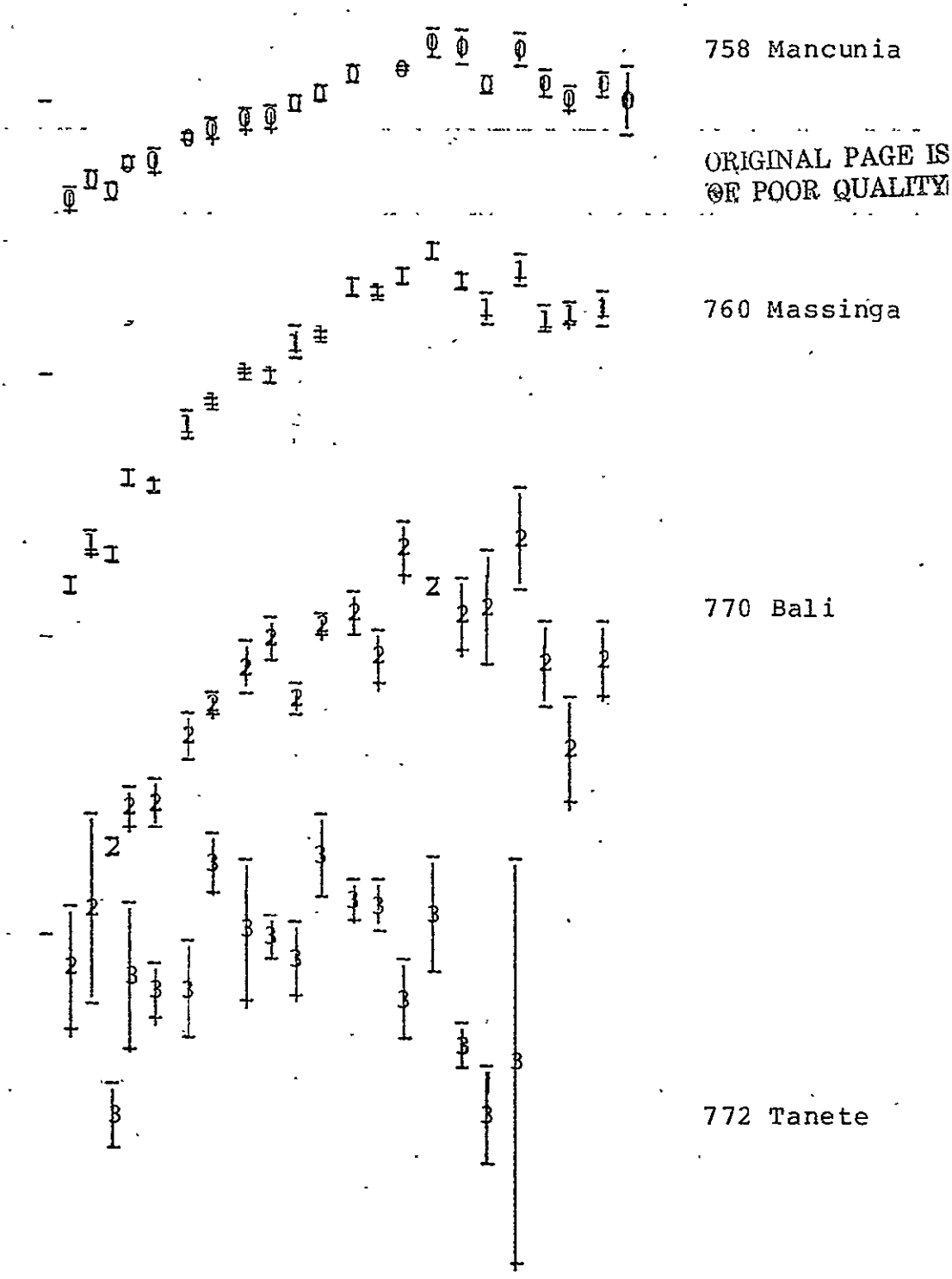

781 Kartvelia
782 Montefiore
783 Nora
785 Zwetana
790 Pretoria

895 Helio
909 Ulla
911 Avg.
925 Alphonsina
944 Hidalgo

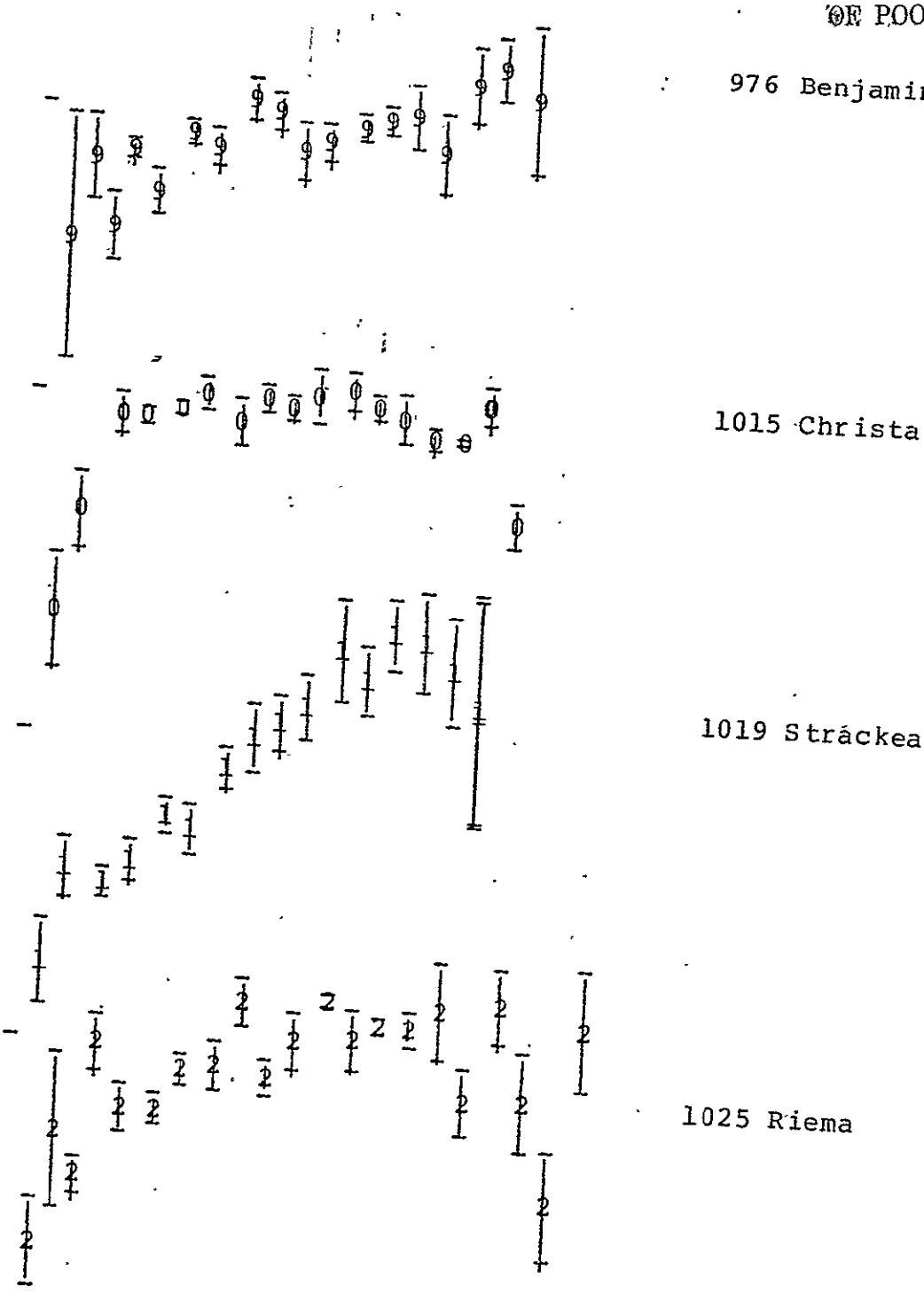

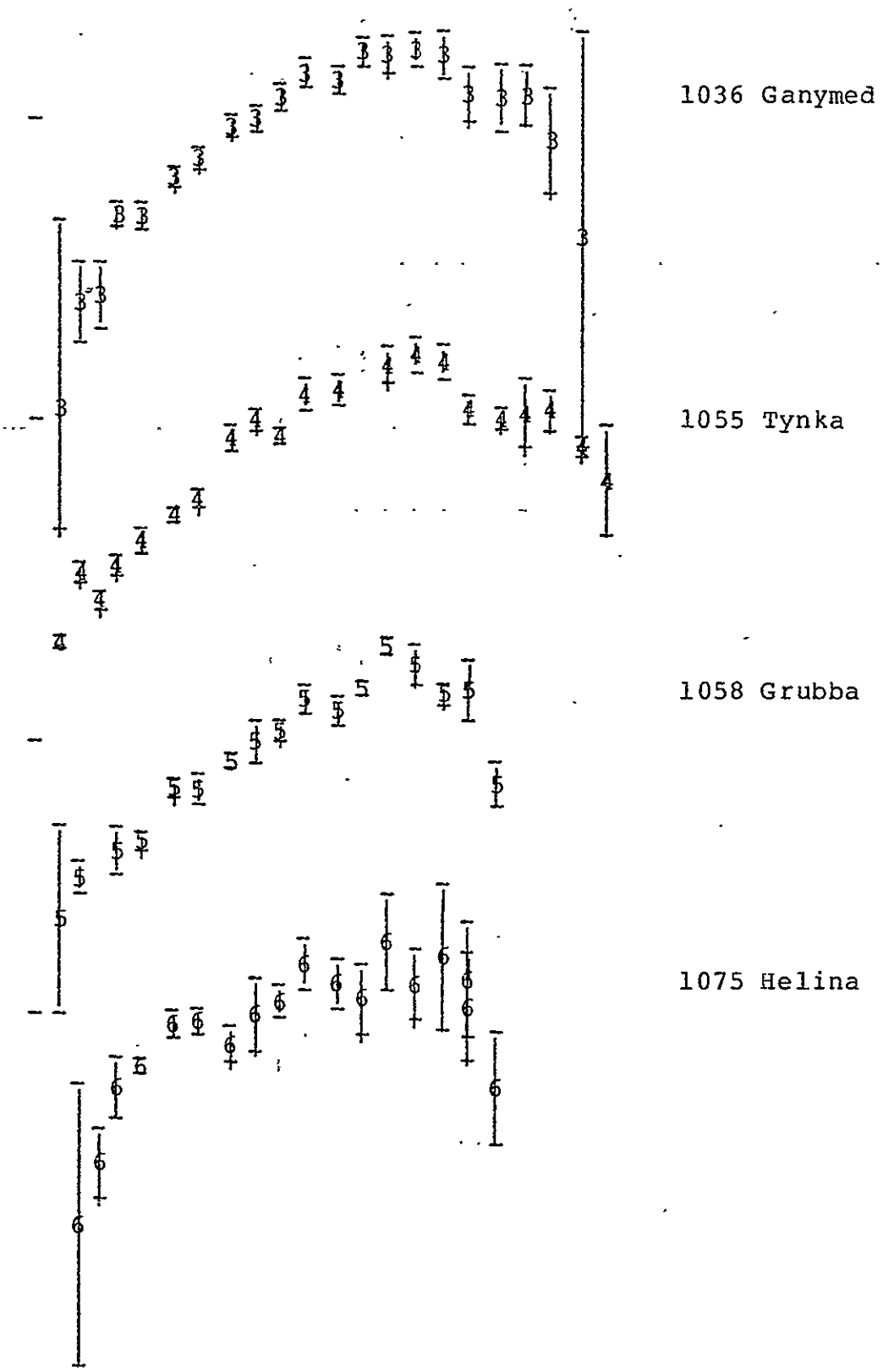
1036 Ganymed
1055 Tynka
1058 Grubba
1075 Helina

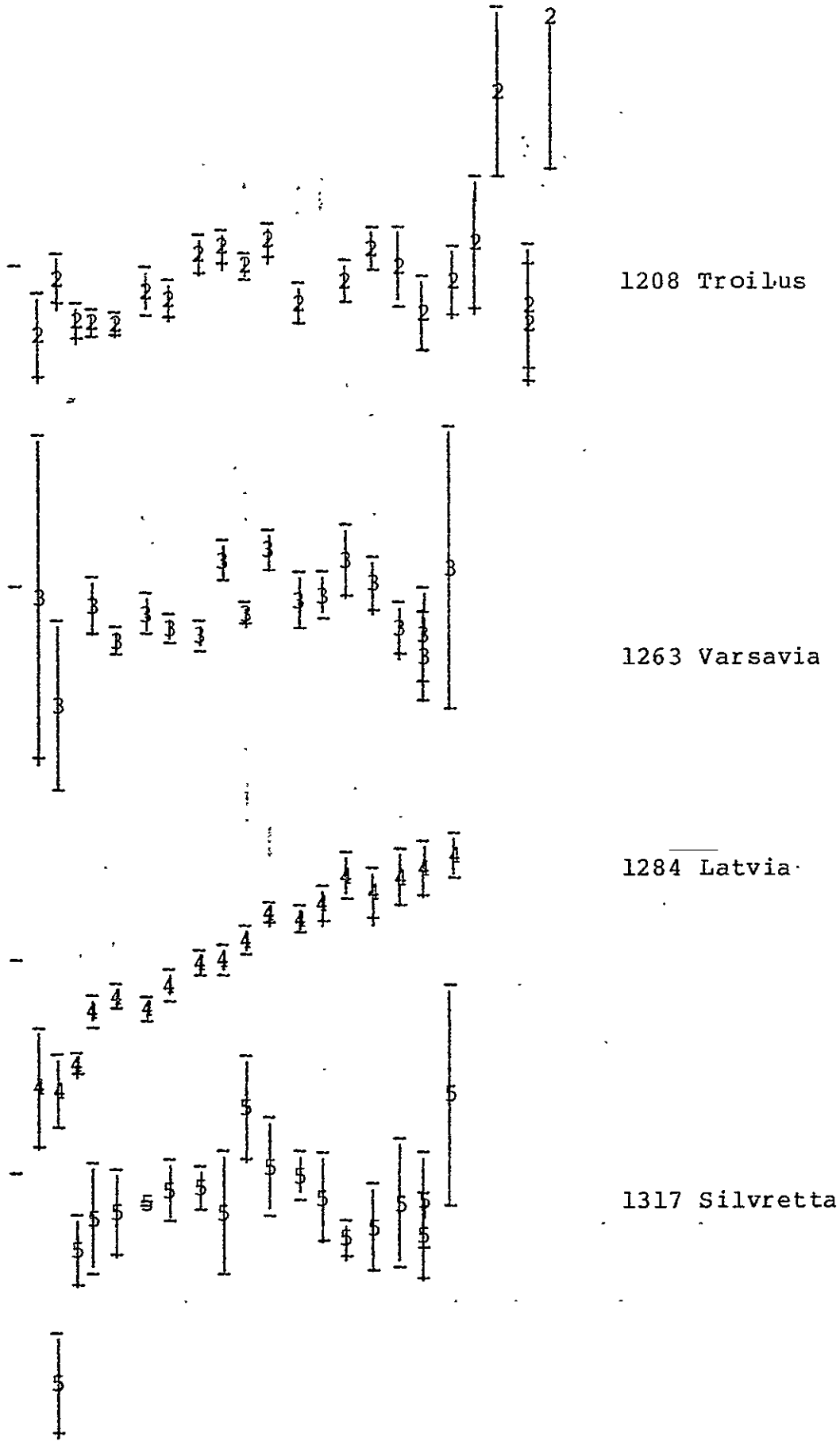
1208 Troilus
1263 Varsavia
1284 Latvia
1317 Silvretta

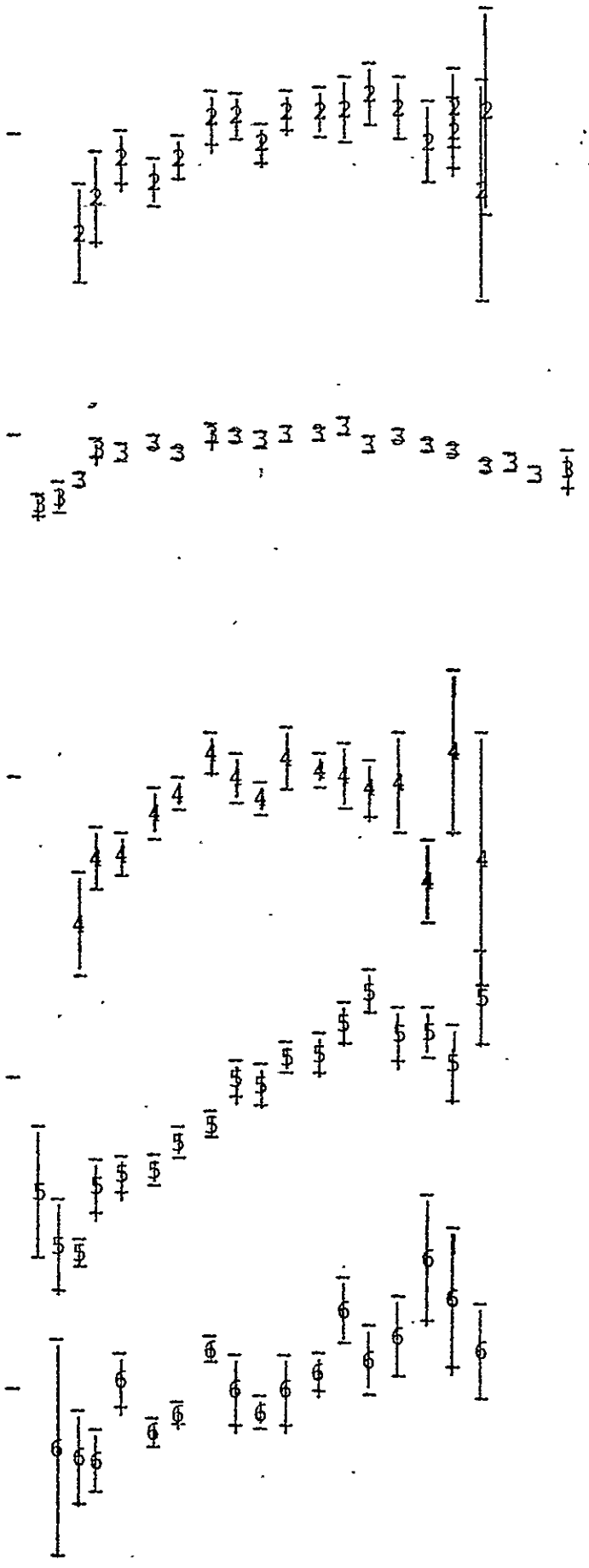

1566 Icarus

1580 Betulia

1595 1930 ME

1620 Geographos

1645 1933 OJ

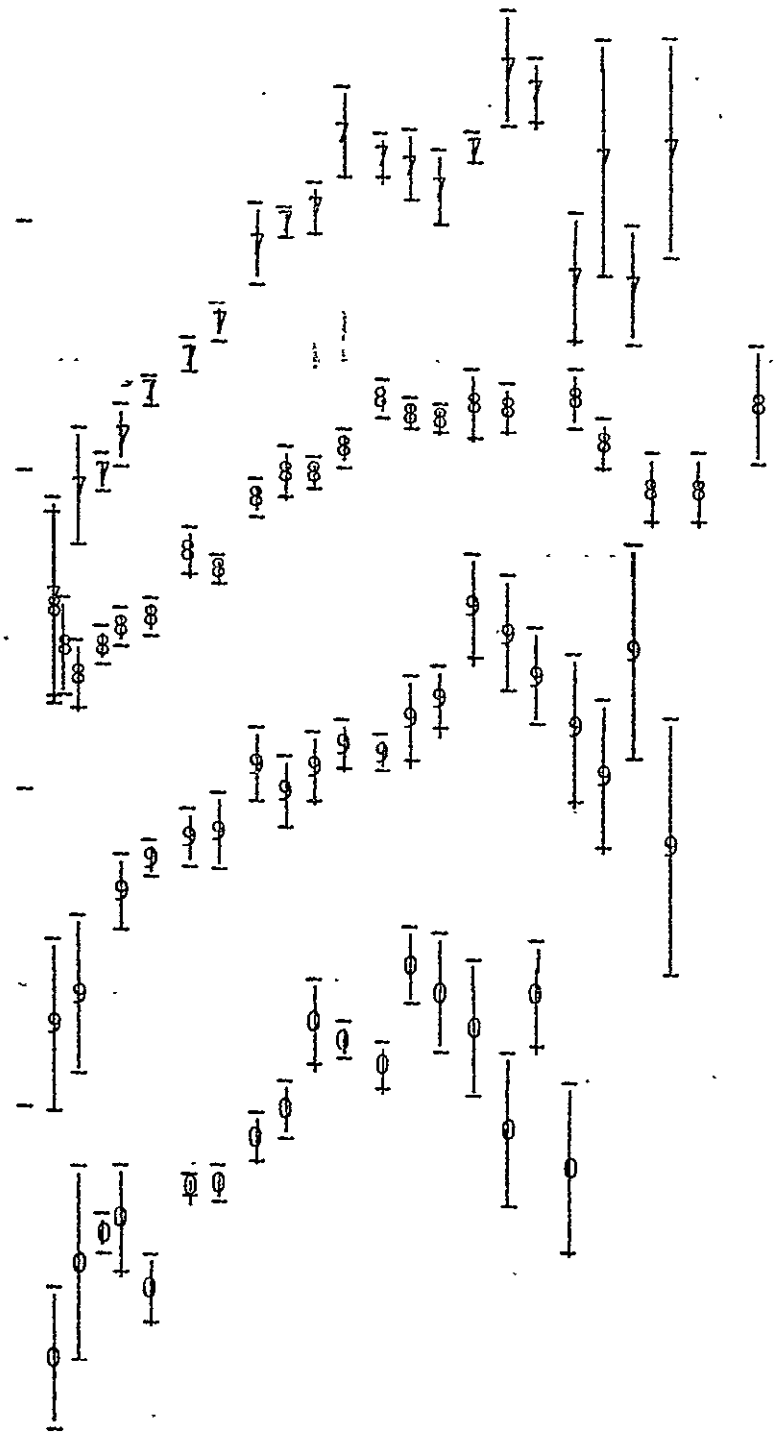

1656 Suomi

1685 Avg.

1727 1965BA

1830 1968 HA

APPENDIX III

"The Nature of Trojan Asteroid 624 Hektor"

by

William K. Hartmann and Dale Cruikshank

Icarus, in press

7686 Icarus 0102
(Vol. 36.3) (pn 2175) (ms 2570)

ICARUS 11, 111–111 (1978)

The Nature of Trojan Asteroid 624 Hektor

WILLIAM K. HARTMANN[1]

Planetary Science Institute, 2030 East Speedway, Suite 201, Tucson, Arizona 85719

AND

DALE P. CRUIKSHANK

Institute for Astronomy, University of Hawaii, 2680 Woodlawn Drive, Honolulu, Hawaii 96822

Received April 28, 1978; revised July 17, 1978

We report new visual and 20-μm photometry obtained when Hektor was seen nearly along its rotation axis. The visual amplitude was near its minimum, only 0.06 mag, confirming the Dunlap–Gehrels (1969) rotation model. The new observations confirm and refine the large size and low albedo assigned by Cruikshank (1977) from observations of the opposite rotation pole. The albedo of this pole is found to be $pv = 0.022 \pm 0.003$, overlapping the uncertainty of Cruikshank's 0.03 value for the opposite pole. The low albedo makes Hektor roughly three times bigger than estimates of a few years ago. The light variations are interpreted as due to elongated shape. If this is correct, Hektor is both the largest and most elongated known Trojan, as well as being the most elongated known asteroid of its size. From considerations of Trojans' peculiar properties, we propose that Hektor is a somewhat dumbbell-shaped object roughly 150×300 km in size, resulting from partial coalescence of two primitive spheroidal planetesimals during a relatively low-speed collision in the Trojan Lagrangian cloud, with energy too low for complete disruption. Calculations supporting this model indicate that Trojans may be less altered by collisions than belt asteroids. Observations in 1979 and 1980 can help test this model. A note added on July 17, 1978 relates our result to recent evidence of possible binary asteroid pairs, which may also arise from early low-velocity asteroid–asteroid interactions.

INTRODUCTION

Study of the visual photometry of Trojan asteroid 624 Hektor by Dunlap and Gehrels (1969) led to a geometric model of this body characterized by a uniform-albedo circular cylinder with hemispherical caps on the ends, rotating about an axis perpendicular to the long axis of the cylinder with a rotation period of $6^h55^m21^s115$, and with the rotational axis only $10° \pm 2°$ off the ecliptic plane. The total length of Hektor derived by Dunlap and Gehrels to fit the lightcurve is 5.3 R, where R is the radius of the cylinder and the hemispherical caps. A model with this extreme shape and unexpected orientation was derived to fit the photometric lightcurves obtained by Dunlap and Gehrels at a number of aspect angles, including pole-on and equator-on aspects. Seen equator-on, the visual brightness varies during the asteroid's rotation by a factor of 3.1 (1.23 mag), while the variation seen when viewing along rotation axis is 0.1 mag or less (Dunlap and Gehrels, Eqs. 11 and 12). By assuming the albedo to be 0.28, Dunlap and Gehrels estimated $R = 21$ km, and deduced a shape 42 km thick and 111 km long.

At Hektor's opposition in 1972, Cruikshank (1977) obtained 10- and 20-μm

[1] Guest Observer, Mauna Kea Observatory.

0019-1035/78/0363-111$02.00/0

radiometry which was combined with earlier visual photometry from other sources (Herget, private communication) to derive the albedo of Hektor, along with albedos of three other Trojans. All four albedos turned out to be much lower than the belt-asteroid values that had been assumed, thus increasing the estimate of Hektor's size. Cruikshank (1977) rederived Hektor's dimensions using the Dunlap–Gehrels model, giving $R = 63$ km, implying an object about 126 km thick and 334 km long (these values being slightly corrected following further reduction by DPC in 1978).

Four factors made us desire new observations. First, the thermal flux detected in 1972 was only at the limit of measurement. Second, near-simultaneous visual and thermal infrared measures of one side of Hektor were desirable to allow the first albedo determination actually derived for a *single polar face* of Hektor. Third, during the 1972 observations, Cruikshank visually monitored Hektor, which was predicted to show only an 0.1-mag variation due to its predicted pole-on aspect, and suspected a larger variation by as much as 0.5 mag raising a possible question about the Dunlap–Gehrels model of Hektor's rotation and pole orientation. Fourth, we hoped to make an unambiguous test of whether the light variations of Hektor are due to irregular shape, in which case the two lightcurves would be correlated, or albedo variation yielding anticorrelated lightcurves.

Regarding items one and two, we improved on the thermal flux measurement and achieved our goal of deriving a consistent albedo for one face of Hektor. Regarding item three, our new observations confirm Dunlap and Gehrels' rotation model and their prediction of a 1977 view along the rotation axis. Consequently, regarding item four, the amplitude was too small to allow accurate detection of the infrared light variations. We thus did not succeed in a true test of albedo patchiness, although we did obtain nearly simultaneous visual and ir data. Thus, the test in item four will have to await the larger amplitude four will have to await the larger amplitudes predicted for 1979 or 1980.

OBSERVATIONS AND REDUCTIONS

The infrared and visible region photometry was obtained with the 224-cm telescope at Mauna Kea Observatory, the former on 11 and 12 February, and the latter on 13 and 14 February 1977. The infrared measurements were made in the way described by Cruikshank (1977) using a broadband filter with effective wavelength of 20 μm. The star α Boo was taken as the primary flux standard for which $m_{20} = 3.32$ (Simon *et al.*, 1972). Both nights when Hektor was measured in the infrared were of good quality, with 20-μm extinction $\sim$0.3 mag/air mass.

The visible region photometry was obtained with an area-scanning photometer on loan from Dr. K. Rakos of Vienna Observatory. We used a standard broadband V filter with the GaAs phototube and a circular aperture of diameter 9.5 arcsec. The photometer aperture scans in a linear pattern from the sky across the object and on to the sky the output being divided into 100 channels which are coadded and stored in a multichannel analyzer. A typical observation consisted of 120 coadded scans. Of the 100 channels, about 30 on the sky and 50 on the asteroid (or comparison star) were averaged to give the signal. In the absence of convenient faint standard stars, we used stars of $m_v = 5.6$ to 6.6 (HR 5165, 5214, and 5343) observed with a calibrated neutral density filter (corresponding to 7.13 mag) as primary standards. A faint field star of brightness about three times that of Hektor was used as a local standard for removal of air-mass and system drift effects, both of which were small. We did not compute transformation coefficients

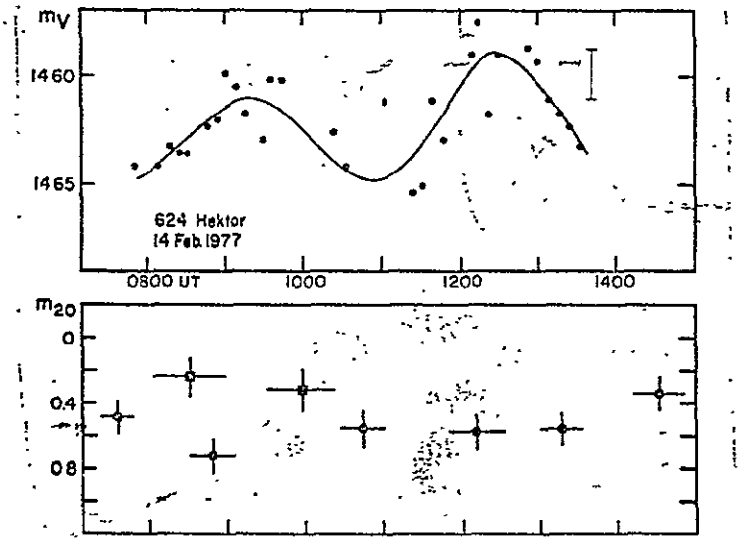

FIG. 1. Comparison of visual (m_v) and thermal infrared (m_{20}) photometry of Trojan asteroid 624 Hektor, reduced to the same epoch. Because the object was seen nearly pole-on, the amplitude was reduced to 0.06 mag, too small to be measured in the infrared. For infrared data, 11 February is represented by squares and 12 February is represented by circles.

for the V filter. Since we used comparison stars for which UBV photometry is accurately known, the system differences are expected to be negligible.

Figure 1 is a comparison of Hektor's visual and infrared lightcurves, reduced to the same epoch. The visible lightcurve is based on the 14 February data only, clearly defining the two maxima. The solid line through these data points was drawn by hand on the assumption that the Dunlap–Gehrels period of 6^h55^m is correct. Because Hektor was viewed nearly pole-on, the amplitude is only about 0.06 mag. The vertical bar represents one sigma uncertainty, about 0.02 mag. From the epoch established by the photometry of 14 February and the Dunlap–Gehrels period, the infrared data were corrected for rotation phase and plotted accordingly. Each 20-μm point corresponds to 40 min of integration, except for two points which represent 30 min each. The error in the infrared points is typically ± 0.1 mag or less.

In computing the radius and geometric albedo of Hektor from the infrared and visible region photometry, we have followed the procedure and assumptions made by Cruikshank (1977); a detailed explanation is found in Jones and Morrison (1974) and Morrison (1976). Unit emissivity was assumed, and the phase integral, q, was taken as 0.6, a value appropriate for dark bodies without atmospheres. In keeping with the earlier reductions, we assumed that the ratio of the bolometric geometric albedo to the visual geometric albedo, $p/p_V = 1.0$. Spectral observations [such as those of McCord and Chapman (1975)] may allow future refinement of the last estimate.

Hektor was very near opposition (7 February 1977) and the solar phase angle at the time of the photometry/radiometry was 2.6 to 3.1°; no correction to m_{20} or m_V was made for phase angle. The distance of Hektor to the Sun was 5.13 AU and to the Earth was 4.07 AU.

The geometric albedo of Hektor computed from m_V and m_{20} is $p_V = 0.022 \pm 0.003$. We used the mean values $m_V = 14.63 \pm 0.03$ and $m_{20} = 0.48 \pm 0.16$, calculated from the range of values for both quantities shown in Fig. 1. The uncertainty

in p_V does not include uncertainties in the visual magnitude of the Sun, which was taken as -26.77, but does include the range of uncertainties in m_V and m_{20}. The radius of a sphere having the same surface area as Hektor is thus $\bar{r} = 108 \pm 10$ km. In the Dunlap–Gehrels model $R = 61$ km and the total length of Hektor is about 325 km.

The sensitivity of the computed albedo and equivalent radius to the assumed or measured values of the various parameters entering into the calculation has been discussed by Morrison (1976). The photometric/radiometric radius given here is not highly sensitive to the assumed values of q and p/p_V because the geometric albedo is very low. The computation does assume a spherical body with the surface temperature distribution corresponding to a spherical geometry in instantaneous thermal equilibrium with the solar insolation, and while thermal equilibrium is virtually assured by the near polar view obtained in 1977, the assumption of sphericity is clearly invalid. We retain the result of this first-order calculation, however, because of the probable greater significance of the effect of the uncertainty of the emissivity phase function.

DISCUSSION OF THE OBSERVATIONS

A feasible alternative to the Dunlap–Gehrels model of Hektor's highly irregular shape is a model in which the large variation in visible brightness at some aspects results from a strongly asymmetric albedo distribution across the surface of a relatively spherical body. A precedent for this proposal exists—Iapetus, an outer satellite of Saturn, is a roughly spherical body having a bright trailing hemisphere and a dark leading hemisphere with a distinct boundary between (Murphy *et al.*, 1972; Morrison *et al.*, 1975). The disparity in albedo of the hemispheres [0.35 and 0.07 (Morrison *et al.*, 1975)] and the synchronism of the rotation and revolution periods of Iapetus lead to

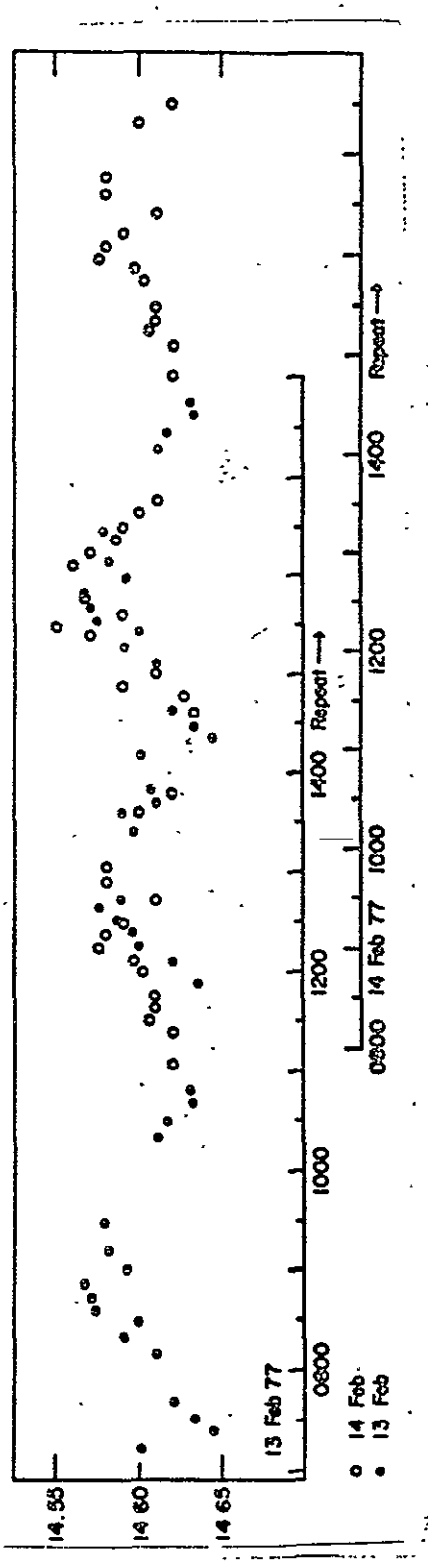

FIG. 2. Visual lightcurve of 624 Hektor from combined photometry of two nights, reduced to common epoch. Because the two maxima were recorded in reverse sequence on the two nights, each night's data are repeated for 0.5 cycle, giving 1.5 cycles for each night and giving one complete cycle of overlapping data in the center of the diagram. Lightcurve is drawn by hand based on Dunlap–Gehrels period of 6^h55^m.

TABLE I

LARGE TROJAN ASTEROIDS IN ORDER OF ESTIMATED SIZE

Name	Radius (km)		Width of angular excursion [max. distance from Jupiter −min. distance] (Chebotarev *et al.*, 1974)
	Measured[a]	Est.[b]	
624 Hektor	105	(81)	34
911 Agamemnon		74	32
1437 Diomedes		64	53
617 Patroclus	60	(64)	9
1172 Aneas	60	(59)	18
588 Achilles		59	11
1143 Odysseus		59	18
659 Nestor		51	18
1208 Troilus		49	21
1583 Antilochus		49	47
884 Priam		47	19
1173 Anchises	40	(45)	46
1404 Ajax		39	35
1749 Telemon		25	24
1647 Menelaus		22	13

[a] Present work and Cruikshank (1977).

[b] Calculated from g magnitudes listed in 1977 Ephemerides of Minor planets, scaled to four measured Trojan asteroids, with scaling coefficient weighted toward three smaller "normal" Trojans. Thus, low albedos of about 0.02 are assumed for all Trojans.

variations in m_V of some 2.1 mag (Morrison *et al.*, 1975).

Murphy *et al.* (1972) and Morrison *et al.* (1975) showed that infrared and visible fluxes of Iapetus are anticorrelated, thus precluding an irregular shape as the cause of the large variation in m_V.

In the case of Hektor, simultaneous visual and thermal infrared lightcurves have not been obtained for similar analysis, to discriminate shape from albedo as the major factor in the brightness variations. As shown in Fig. 1, our own 1977 view was so nearly along the rotation axis that the thermal or infrared variation was below the observational precision which was about ±0.1 mag. Thus, further near-simultaneous infrared and visible observations should be made during the 1979 or 1980 apparitions of Hektor, when the amplitudes will be closer to their 1.2-mag extreme.

In spite of the absence of definitive proof of shape as the main factor in Hektor's light variations, several facts argue in this direction. First, our new pole-on measurements occurred at the pole opposite to the one measured by Cruikshank in 1972, but gave essentially the same values of p_V and R. Second, Gehrels' lightcurves taken nearly perpendicular to the polar axis show strong symmetry in the shape of the two lightcurve lobes. Both these observations preclude strong patchiness. Albedo variations sufficient to explain the light variation would have to be both extreme and surprisingly regular, one hemisphere having several times the albedo of the other with a rather sharp boundary along a longitudinal meridian. Furthermore, the mechanisms suggested to explain the Iapetus case, which rely on Iapetus's synchronous tidal lock with Saturn (Soter, Cornell Satellite Conference, verbal presentation, 1974), are totally inadequate for Hektor. No likely mechanism is known that would make two hemispheres of a spherical Hektor markedly different in albedo, while leaving the polar-view albedos nearly the same. The main cause of Hektor's light variation is thus probably an elongated shape.

Nonetheless, slight albedo variations or surface irregularities on Hektor are not precluded, as shown in Fig. 2. Here, both nights of visual photometry are combined and repeated in 1.5 rotational cycles, so that (after appropriate reduction to the same epoch) a complete lightcurve is built up from data on both nights. Both this curve and the single-night data in Fig. 1 suggest that one maximum is slightly brighter than the other by not more than 0.02 mag. Although this is about the size of the one-sigma error, it is plausible that the

lightcurve of the elongated object is modulated by albedo patchiness or variations in surface topography (such as hilly or inclined flat areas) that might cause variations in reflected light. Similarly, Dunlap and Gehrels (1969) find slight color differences in views of different sides of Hektor, but note that their smallness argues against major albedo variation as an explanation of the lightcurve.

In summary, the new observations reaffirm that 620 Hektor is a highly unusual object. Its light variations can be as great as a factor of 3.1 (Dunlap and Gehrels, 1969), probably because of an extraordinary elongated shape. The amplitude of observed variations can change from the factor of 3.1 to a factor of only 1.06 because the pole of rotation lies close to the p plane of the ecliptic. With its equivalent mean radius $\bar{r}$ of about 108 km, Hektor is considerably larger than the next largest known Trojans, such as 911 Agamemnon, 1437 Diomedes, 617 Patroclus, or 1172 Aneas (radii r = 74, 64, 60, and 60 km, respectively). Further size comparisons are given in Table I. Hektor is also substantially bigger than the neighboring bodies of similar low albedo, Jupiter's outer satellites J6 and J7 (radii r = 85, 40 km, measured by Cruikshank, 1977). It is also much more elongated than other measured Trojans; Dunlap and Gehrels report lightcurve amplitude factors of only 1.2 to 1.4 for 911 Agamemnon and 1437 Diomedes. Degewij (private communication and 1978) reports that five still smaller Trojans exhibit similarly small amplitudes, generally with amplitude factors <1.2. Hektor is also much more irregular than any other belt asteroids of its size; of the first 25 numbered belt asteroids, Degewij (1977) finds none with amplitudes above about 1.5, and about 96% with amplitudes <1.3. Other asteroids known for irregular shape are generally much smaller and in eccentric orbits [e.g., Earth-crossers 433 Eros, ~13 × 15 × 36 km; and 1620 Geographos, 1.5 × 4.0 km (Zellner, 1976; Dunlap, 1971, 1974; Degewij, 1977)]. Hektor's properties are so unusual that their proper interpretation should tell us interesting facts about the nature of planetary bodies.

WORKING HYPOTHESIS ON NATURE AND ORIGIN OF HEKTOR

Irregularly-shaped asteroids in the main belt are often assumed to be fragments of

TABLE II

COMPARISON OF SHAPES: ROCK FRAGMENTS AND 624 HEKTOR

Bodies	Collision velocity	Lightcurve amplitudes (ratio b/a)			Reference
		Average	Percentile		
			10th	1st	
719-cm-scale igneous rock fragments	2.6, 3.7 km/sec	0.73	~0.52	~0.37	Fujiwara *et al.* (1977)
46-cm-scale igneous rock fragments	26 to 50 m/sec	0.71	0.54	<0.33	Hartmann (1977, unpublished experimental data), Fig. 3
Hektor	—			0.32	Dunlap and Gehrels solution for view in equatorial plane

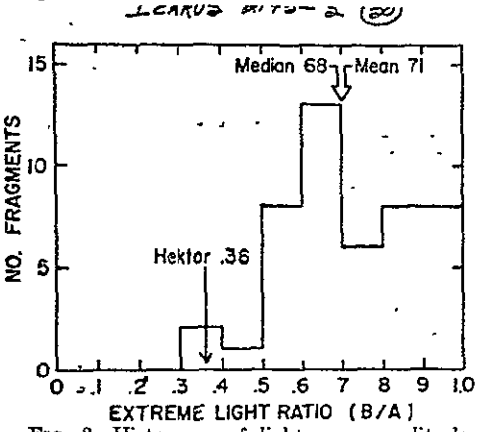

FIG. 3. Histogram of lightcurve amplitudes for stably spinning igneous rock fragments generated by collisional fragmentation (ratio of axes b/a). Data from experiments on centimeter-scale rocks fragmented at velocities 26 to 50 m/sec. Distribution agrees with results by Fujiwara *et al.* (1977), and suggests that shape inferred for Hektor would be extreme for a rocky particle produced by collisional fragmentation (see text and Table II).

larger bodies, but Hektor is so much larger and more irregular than its Trojan companions that it is difficult to picture as one among many fragments of a still larger parent Trojan. Even if Trojans are fragments of some shattered parent, Hektor would be anomalous: a cigar-shaped fragment among a swarm of smaller spheroidal fragments. This statement is supported by two experimental studies of shapes of fragments of igneous rock targets broken by impacts, which show that only of the order of 1% of the fragments have lightcurve amplitudes (defined by b/a axis ratio for stable spin around c axis) as large as Hektor's. As seen in Table II and Fig. 3, the two studies show good agreement and indicate that Hektor (to the extent that can be judged from lab-scale experiments) would make a very unusual fragment. From theoretical models of the accretionary process, one might expect the largest body in a swarm to be the most stable against collisions with other members and perhaps rather spherical, as with Ceres, rather than being a singularly irregular fragment. A fragmental origin of Hektor thus seems unlikely. To attempt a purely geometric explanation of Hektor's lightcurve, Cook (1971) suggested it might be a coorbiting binary pair of asteroids or a contact binary (Fig. 4), arguing that rotational stresses are too great to permit stable rotation in Hektor's period of 6^h55^m with a Dunlap–Gehrels body of meteoritic composition. However, Hartmann (1971) pointed out that Cook had represented meteoritic material by unusually weak meteorites. It now appears that Cook's arguments alone neither rule out nor necessitate a binary pair or contact binary. Also, Cook's binary models, with aspect ratio of only 2.0, fail to match the 3.1 aspect ratio required by Dunlap and Gehrels observations.

On different grounds—a mixture of cosmogonic, observational, and dynamical considerations—we now suggest a new working model resembling Cook's contact binary. We suggest that Hektor could be a partially coalesced pair of Trojan asteroids which collided with energy too low to cause complete fragmentation, forming a dumbbell-shaped object (Fig. 4, bottom). This model pictures the two pre-Hektor

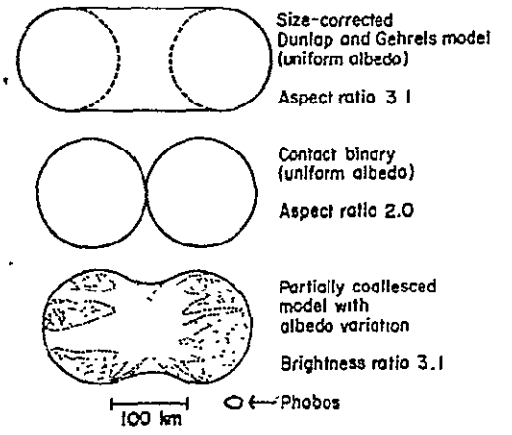

FIG. 4. Three models for Hektor discussed in the literature. Top is geometric model derived by Dunlap and Gehrels to fit lightcurve. Middle is contact binary asteroid discussed by Cook (1971) on dynamical grounds, but not fitting lightcurve. Bottom is model proposed here of partially collisionally coalesced pair of asteroids, with Phobos shown for scale. Albedo brightening in crushed zone allows observed brightness ratio.

bodies as being neighboring relatively large primitive objects in the Trojan cloud. In fact, we argue that a swarm of Goldreich–Ward-like (1973) initial planetesimals, at perhaps 40 to 80-km radii caught in Lagrangian clouds, might very likely produce asteroids with the properties of Trojans, including a dumbbell-shaped object like Hektor.

We next examine in more detail the plausibility of certain aspects of this model and certain observations that are consistent with it.

1. Plausibility of partial coalescence of two Trojans. Unlike bodies circulating in the belt, where average approach velocities are around 5 km/sec, giving about 10^4 times the minimum energy per gram needed to fragment igneous rock (Hartmann, 1978), Trojans circulate around a Lagrangian point which has zero velocity relative to the center of the swarm. This fact, coupled with the lower orbital velocity of the Trojans, increases the probability that a pair of neighboring Trojans might occasionally move with nearly zero relative velocity, thus enabling them to fall together and collide with speed only barely exceeding escape velocity. In this case, any significant energy loss would prevent rebound and reescape of the masses from each other, regardless of whether they fragmented or not. In experiments with rocks and rock powders, Hartmann (1978) showed that at low collision speeds typical of rock rebound (less than about 30 m/sec) about 14% of the collision energy is typically lost (with no fracturing occurring) when nonrotating clean igneous rock spheres collide with flat surfaces; and that larger fractions (typically up to 70%) may be lost in spinning up slow-rotating irregular colliders. Still more energy is lost if crushable materials (such as deep regolith layers or aggregate structures) are involved. At higher collision velocities, average energy per gram is sufficient to fracture large amounts of rock, with still more energy lost to fracturing-and-heating. For impacts at 5 to 30 km/sec, O'Keefe and Ahrens find that typically more than 90% of the projectile kinetic energy is lost to heating and plastic work, with less than 10% surviving as kinetic energy of debris. Details of the fracture process during the collision are difficult to evaluate theoretically or experimentally, though much energy is known to be consumed in widespread fracturing beyond (underneath) the impact site. Most crushing occurs near the impact site; but spalling or fracturing may be pronounced at the antiimpact site (as on Phobos?); and other fractures may permeate the otherwise intact body. The energy losses during collision may thus be sufficient to crush rock locally and at the same time prevent either rebound or complete fracturing of the two colliding bodies.

We note that escape velocity of a 70-km planetesimal is of the order 70 m/sec ($\rho \sim 1.9$ g/cm^3). It thus appears plausible to us that in a certain range of impact speeds just above escape velocity, two 70-km-scale primitive planetesimals could collide expending energy to crush material around the impact site, but without enough energy to disrupt the two bodies into a cloud of debris. Because insufficient energy would remain to separate the two bodies, the result would be a dumbbell-shaped object with a crushed contact zone, as illustrated in the lowest part of Fig. 4.

2. Rotational stability. For two spheres in contact, assuming zero bonding strength, the minimum stable rotation period (the period equal to circular coorbital period) is

$$P = 2(3\pi/G\rho)^{1/2}$$
$$= 6.61/\rho^{1/2} \text{ hr},$$

where ρ is the density of the material. This gives:

ρ	Minimum stable P
0.91	6^{h}92 (observed)
1	6^{h}6
2	4^{h}7
3	3^{h}8

Thus, even if two spheroidal Trojans had lodged together with negligible bonding strength, the observed period would give a stable object for any density greater than $\rho \cong 0.9$. Spectral observations of Hektor (McCord and Chapman, 1975) are consistent with a stony material, resembling many other asteroids in its reflectivity turndown in the ultraviolet; the low albedo of Hektor (Cruikshank, 1977; this paper) are also consistent with stony material. A density exceeding unity is reasonable on these grounds. If the objects had bonded after contact, perhaps by resolidification of melted materials (such as minor ices in a stony matrix?) stability of the object would be even further enhanced. We thus conclude that Hektor is rotationally stable against disruption [thus answering the question raised by Cook (1971)].

3. Lightcurve and aspect ratio. The top drawing in Fig. 4 shows the shape derived by Dunlap and Gehrels from purely geometric considerations, with the length adjusted arbitrarily to match the observed lightcurve, giving aspect ratio of 3.1 for a view in the equatorial plane. The Dunlap–Gehrels object was assumed to have a uniform albedo. The middle drawing in Fig. 4 shows the Cook contact binary model, which, with uniform albedo, would have aspect ratio only 2.0. The lower model illustrates our suggestion, applying the common circumstance that crushed rock impact ejecta is lighter than the impact material, as in lunar rays (or alternatively that the interior exposed material is brighter than the very dark surface). For example, the lightcurve amplitude of 3.1 and the average polar albedo of 0.025 would be given by covering the middle 40% of the polar "side view" with material of albedo about 0.041 (still very dark) and the outer two hemispheres with material of albedo 0.015. This feature of the model could be tested by further infrared comparisons of the "side view" and "end view" during the next few apparitions, since it predicts that the side view should have lower temperature and higher mean albedo than the end views.

4. Plausibility of inter-Trojan collisions. Van Houten *et al.* (1970), counted faint Trojans and established a size distribution down to Trojans of radius r about 7 km (corrected for now-known low albedos). Their published size distribution corresponds to a cumulative frequency proportional to about r^{-2}, similar to that in the main belt, thought to have been established by collisions. Lab studies and field observations (Hartmann, 1969) show similar relations for collisionally fragmented rocks, such as an r^{-2} relationship for rocks after a few collisions and r^{-3} for rocks after much grinding or high energy imput. These results suggest that the smaller Trojans owe their numbers to collisional evolution, but do not establish whether many collisions have occurred, or whether the power-law tail of small fragments is the product of only a few major collisions. For example, fragmentation of a few large objects in an initial Gaussian-like size distribution (as might result from Goldreich–Ward formation of planetesimals) suffices to convert most of the size distribution to the power-law form (Hartmann, 1968).

Thus, we now ask whether it is dynamically plausible that at least a few collisions occurred among initial Trojans. To make a Hektor-sized object, bodies of $r \simeq 74$ km would be needed. From the Van Houten (1970) statistics, we estimate enough material in a Trojan cloud to make a number of these objects of the order $N = 30$. From particle-in-a-box considerations for equal sized objects, the number of collisions per second suffered by one of these objects would be

$$n = 2\pi S^2 v_\infty N/V,$$

where S = gravitational cross section, v_∞ = effective sweeping velocity, and V = volume of cloud. To estimate the volume of the cloud, we note that 80% of

a sample of 15 Trojans with cataloged orbits have inclination less than 22° and eccentricity less than 0.12, with a mean semimajor axis of 5.19 AU. According to Chebotarev *et al.* (1974), who present numerical integrations of Trojan orbits, 80% of a sample of twelve librate over a total angular width of 30° in Jupiter's orbit, or 2.7 AU. From these data, we derive cloud dimensions of 1.25 AU width radial to the Sun, 3.9 AU perpendicular to the solar system plane, and 2.7 AU in length (the "box" of the particle-in-a-box calculation), with volume approximately 3×10^{40} cm^3. The effective relative encounter velocity is difficult to calculate because of the concept of a Lagrangian cloud. The conventional approximation for objects in near-circular orbits (Safronov, 1972, p. 69) is $v_\infty = e V_{circ}$, giving about 1.1 km/sec, using the mean eccentricity of 0.87. However, since the objects are bound in the cloud and circulate around its center, they may spend some time with much slower motions relative to the center of mass of the system. Szebehely (1967, p. 516) reports that the typical cycling time from one end of a cloud to the other for most Trojans is roughly 75 to 85 years, giving a mean motion of about 0.3 km/sec relative to the cloud center. We assume a relative encounter velocity of $v_\infty = 1$ km/sec. Because this is high relative to the escape velocity of the planetesimals ($V_{esc} \sim 70$ m/sec), $S \simeq R = 74$ km. From these values, we derive a value for the two clouds together of the order 0.2 collisions in solar system history. This says that there is a very reasonable chance that one, but not many Hektor-like objects would have been created, taking into account the uncertainties involved in asteroid number, relative motions in the cloud, etc.

A closer examination reveals an interesting property of collisional mechanics in the Trojan cloud, as shown in Fig. 5. The gravitational cross section, S, is given by

$$S^2 = R^2(1 + 2v_{esc}^2/v_\infty^2),$$

where v_∞ is still the relative encounter velocity at very great separation. As noted above, the proper value of v_∞ is uncertain. If it is very large, the collision probability increases as shown in Fig. 5, because the cloud is swept rapidly by the Trojans. If it is very small for a particular comoving Trojan pair, the collision probability also

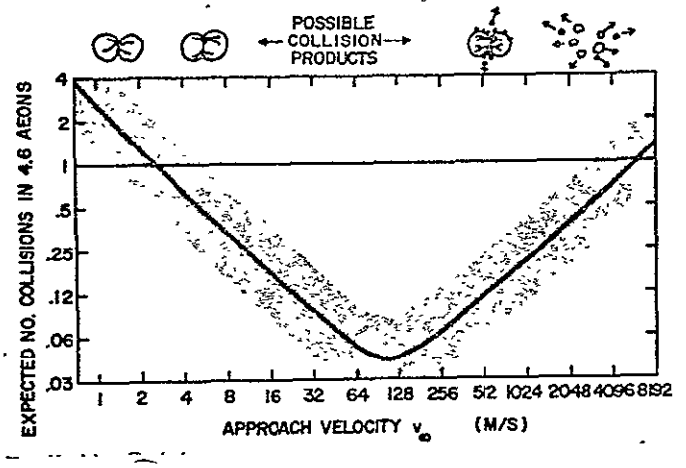

FIG. 5. Estimated numbers of collisions among 60 initial 74-km-diameter planetesimals distributed among two Lagrangian clouds as described in text, plotted as a function of circulation velocity in the clouds. Increases in the numbers of known Trojans per unit volume could shift the v-shaped curve upward. Division of high-probability collisions into fast and slow classes may account for Trojan properties (see text). To show magnitude of uncertainties, stippled band shows range in each direction of a factor 2.

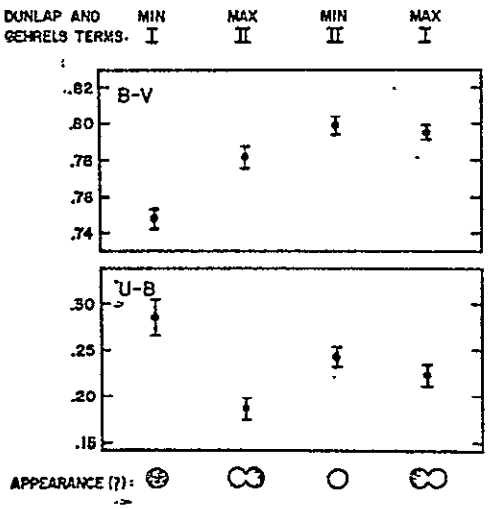

FIG. 6. Comparisons of colors observed on different sides of 624 Hektor, reported by Dunlap and Gehrels (1969). Colors of one end, "Min I," appear significantly different from colors of other faces, possibly supporting the hypothesis that Hektor consists of two distinct planetesimals partially coalesced.

increases, because S increases and objects tend to fall together. Thus, collision probability for a specified number of particles and a specified sweeping velocity passes through a v-shaped minimum shown in Fig. 5. If v_∞ is widely distributed through many values, or if it evolves through different values, there are likely to be two kinds of collision: fast and slow. This effect could contribute to two possible destinies for primeval large Trojans: coalescence into Hektor-like objects at low speed, or fragmentation at high speed. Because of the uncertainty in numbers and velocities, the v-shaped curve has a vertical uncertainty, and the outcome probabilities cannot be definitively evaluated. A Trojan cloud beginning as a number of 74-km spheres might thus consist of a number of primeval cores, a few coalesced pairs, and a large number of fragments, similar to the clouds actually observed.

These results are far from a complete model of Trojan evolution. Increased discoveries of Trojans or a reduced estimate of the effective circulation volume could increase the collision numbers; detailed analysis of the complex circulatory motions of Trojans in a cloud would clarify matters. Furthermore, once one fragmentation occurs among the postulated 74-km bodies, the number of small bodies increases dramatically. Bodies with radii as low as 20 km or perhaps less would have potential for breaking the 74-km bodies. As Chapman and Davis (1974) have pointed out for the main asteroid belt, backward tracing of the collision history reveals that more material may have been originally present than is now seen, with the extra mass removed by Poynting–Robertson and radiation forces as the bodies grind themselves to smaller pieces. Thus, past collisions may have been more frequent than calculated from present conditions. In summary, we conclude that at least a few major collisions among large Trojans have probably occurred.

5. Spectrophotometric tests. If a collision of two primitive objects produced Hektor, and if the Trojans have a certain distribution of different spectrophotometric types, then a possibility (but not a necessity) arises that the two end-on views (showing two originally different bodies) might have different spectrophotometric properties.

The side views would be an average of the two spectrophotometric signatures, or possibly a different signature involving crushed or exposed internal material. This is sketched in the cartoon views in the bottom of Fig. 6. The body of Fig. 6 shows the limited data available on this point. Dunlap and Gehrels (1969) published UBV colors observed when the line of sight was nearly perpendicular to the rotation axis in 1968. Their results show a difference between the two end views, but not quite like that predicted above. One end view (called Minimum I by Dunlap and Gehrels) is more than one sigma (error as estimated by Dunlap and Gehrels) from all other views, with the other three views having nearly overlapping error bars. Dunlap and Gehrels call the color differences "small, if

2. Visual and thermal infrared photometry should indicate a higher albedo on the side faces than end to make the lightcurve amplitude consistent with two partially coalesced spheroidal bodies.

3. Spectrophotometry may possibly, but not necessarily, show differences between the two end-on views if Hektor is composed of two planetesimals slightly different in composition.

4. Further dynamical understanding of motions in the Trojan clouds is necessary to test whether the necessary low-velocity collision is likely. Strongest support would come from a result showing that the required low-speed collision is not highly probable among many objects, but has a marginal probability such that one coalesced body, but not many, might be produced.

Asteroid 624 Hektor holds forth the likelihood that the Trojans are relatively primitive objects, perhaps less altered by collision than belt asteroids, and that 624 Hektor may be a unique product of, and evidence for, collisional evolution.

Note added July 17, 1978: Recent reports of dual dips in lightcurves during occultations of stars by asteroids have created a growing suspicion of binary pairs among asteroids. Pluto is also recently reported to be a small binary planet. If these remarkable findings are correct, they might seem to support Cook's (1971) original suggestion of Hektor as a binary. But we have argued that the 3.1 amplitude factor is very difficult to explain by this assumption, which would predict a factor 2.0 for equal-sized uniform objects, or less if the objects had different size. Instead, we argue that Hektor is a result of partial coalescence and that our model of asteroid–asteroid encounters may shed light on other possible associated asteroid pairs. Most asteroid collision histories have assumed that collisions produce either a single, cratered target or a complete fragmented swarm with fragments escaping at greater than escape velocity. However, there are little-studied intermediate cases where small objects have impact velocity low enough simply to rebound (Hartmann, 1978) or where larger comparable-size objects have energy too low for blowing all fragments away at escape velocity. For example, our model assumes approach at near-zero velocity, collision near escape velocity with the two bodies fractured, but not fragmented, and sufficient energy loss that the bodies cannot subsequently escape from each other. Other cases might lead to binary pairs or asteroids with slowly collapsing debris swarms. A low velocity collision could lead to a rebound of two main bodies with a swarm of small fragments, the interaction of which might lead to a short-lived or long-lived binary pair. A higher-velocity collision could leave the larger (target) body surrounded by a debris cloud with insufficient energy to dissipate, or could totally disrupt both bodies into a rotating debris cloud with insufficient energy to dissipate, but enough angular momentum to cause recollapse into a binary pair. Further calculations are needed to evaluate the lifetimes of such configurations. Hektor may thus serve as a clue leading us toward a variety of asteroid-asteroid encounters that could produce products more varied and interesting than hitherto imagined.

ACKNOWLEDGMENTS

The authors acknowledge discussion with Richard Greenberg on the rotation dynamics. We also acknowledge helpful comments from C. R. Chapman, D. R. Davis, and T. Gehrels, and assistance in reduction of the observations and manuscript preparation by Joanne Metcalfe. Hartmann was supported by NASA contracts NASW 2983 and 3134, and Cruikshank in part by NASA grant NGL 12-001-057. This is Planetary Science Institute contribution No. 101.

REFERENCES

CHAPMAN, C. R., AND DAVIS, D. R. (1975). Asteroid collisional evolution: Evidence for a much larger early population, *Science* 190, 553–556.

COOK, A. F. (1971). 624 Hektor: A binary asteroid? In *Physical Studies of Minor Planets* (T. Gehrels, Ed.). NASA, Washington.

CHEBOTAREV, G. A., BELYAEV, N., AND EREMENKO, R. (1974). Orbits of Trojan Asteroids. In *The Stability of the Solar System and of Small Stellar Systems* (Y. Kozai, Ed.), pp. 63–69. I.A.U.

CRUIKSHANK, D. (1977). Radii and albedos of four Trojan asteroids and Jovian satellites 6 and 7. *Icarus* 30, 224–230.

DEGEWIJ, J. (1977). Lightcurve analyses of 170 small asteroids. *Proc. 8th Lunar Sci. Conf.* 1, 145.

DEGEWIJ, J. (1978). Ph.D. dissertation, Leiden University.

DUNLAP, J. L. (1971). Laboratory work on the shapes of asteroids. In *Physical Studies of Minor Planets* (T. Gehrels, Ed.). NASA, Washington.

DUNLAP, J. L. (1974). Minor planets and related objects. XV. Asteroid 1620 Geographos. *Astron. J.* 79, 324–332.

DUNLAP, J. L., AND GEHRELS, T. (1969). Minor planets. III. Lightcurves of a Trojan asteroid. *Astron. J.* 74, 797–803.

FUJIWARA, A., KAMINOTO, G., AND TSUKAMOTO, A. (1977). Destruction of basaltic bodies by high-velocity impact. *Icarus* 31, 277–288.

GEHRELS, T. (1977). Some Interrelations of asteroids, Trojans and satellites. In *Comets, Asteroids, Meteorites* (A. Delsemme, Ed.). University of Toledo, Ohio.

GOLDREICH, P., AND WARD, W. (1973). The formation of planetesimals. *Astrophys. J.* 183, 1051–1061.

HARTMANN, W. K. (1969). Terrestrial, lunar and interplanetary rock fragmentation. *Icarus* 10, 201–213.

HARTMANN, W. K. (1971). Comment in *Physical Studies of Minor Planets* (T. Gehrels, Ed.), p. 162. NASA, Washington.

HARTMANN, W. K. (1978). Planet formation: Mechanism of early growth. *Icarus* 33, 81–92.

HARTMANN, W. K., AND HARTMANN, A. C. (1968). Asteroid collisions and evolution of asteroidal mass distribution and meteoritic flux. *Icarus* 8, 361–381.

JONES, T. J., AND MORRISON, D. (1974). A recalibration of the photometric/radiometric method of determining asteroid sizes. *Astron. J.* 79, 892–895.

MCCORD, T. R., AND CHAPMAN, C. R. (1975). Asteroids: Spectral reflectance and color characteristics II. *Astrophys. J.* 197, 781–790.

MORRISON, D. (1976). Asteroid sizes and albedos. *Icarus* 31, 185–220.

MORRISON, D., JONES, T. J., CRUIKSHANK, D. P., AND MURPHY, R. E. (1975). The two faces of Iapetus. *Icarus* 24, 157–171.

MURPHY, R. E., CRUIKSHANK, D. P., AND MORRISON, D. (1972). Radii albedos, and 20-micron brightness temperatures of Iapetus and Rhea. *Astrophys. J.* 177, L93–L96.

SAFRONOV, V. S. (1972). Evolution of the Protoplanetary Cloud and the Formation of the Earth and Planets. NASA Technical Translation.

SIMON, T., MORRISON, D., AND CRUIKSHANK, D. (1972). Twenty-micron fluxes of bright stellar standards. *Astrophys. J.* 177, L17–L20.

SZEBEHELY, V. (1967). *Theory of Orbits*. Academic Press, New York.

VAN HOUTEN, C. S., VAN HOUTEN-GROENVELD, I., AND GEHRELS, T. (1970). Minor planets and related objects. V. The density of Trojans near the preceding Lagrangian point. *Astron. J.* 75, 659–662.

ZELLNER, BEN (1976). Physical properties of asteroid 433 Eros, *Icarus* 28, 149–153.

APPENDIX IV.

"Uranus: The Disk Profile in the
7300 Angstrom Methane Band"

by

Michael J. Price and Otto G. Franz

submitted to Icarus

APPENDIX IV

URANUS: THE DISK PROFILE IN THE 7300 ANGSTROM METHANE BAND

Michael J. Price
Planetary Science Institute
2030 E. Speedway Blvd., Suite 201
Tucson, Arizona 85719

and

Otto G. Franz
Lowell Observatory
P.O. Box 1269
Flagstaff, Arizona 86002

Received _____

No. of Copies: 4
No. of MS Pages: 16
No. of Figures: 4
No. of Tables: 0

ABSTRACT

Photoelectric slit-scan photometry of Uranus has been used to determine the radial intensity profile of the planet within the $\lambda 7300\text{Å}$ methane band. Measurements of the point spread function have been used to partially remove the effects of atmospheric seeing. Numerical restoration of the Uranus image, for an entirely arbitrary radial intensity distribution, has been carried out. Significant polar and limb brightening are confirmed to be present on the Uranus disk.

PROPOSED RUNNING HEAD:

THE URANUS DISK

PERSON TO WHOM PROOFS SHOULD BE SENT:

Dr. Michael J. Price
Science Applications, Inc.
5055 E. Broadway, Suite A-214
Tucson, Arizona 85711

1. INTRODUCTION

Limb and polar brightening on Uranus have been detected within several deep CH_4 bands. Brief studies of these phenomena have been carried out by Westphal (1972), Sinton (1972) and Smith (1977) at 8900Å, by Franz and Price (1977) at 7300Å, and by Avis et al. (1977) at 6190Å. These studies have indicated the presence of aerosol particles in the upper regions of the atmosphere.

More extensive investigations have been carried out by Price and Franz (1976, 1978). Their observations were concentrated on the two strong CH_4 bands at 6190Å and 7300Å. Coarse estimates of the shape of each disk profile were obtained from direct predictions for arbitrary theoretical models smeared by known atmospheric and instrumental effects. For the 6190Å band, the planet was found to exhibit a disk of nearly uniform intensity. For the 7300Å band, moderate limb-brightening was apparent. Specifically, the true intensities at the center and limb of the planetary disk were approximately in the proportion 1:2. Extreme limb-brightening, with a corresponding intensity ratio greater than 1:4, was not permitted. The results for the 7300Å band were used by Price (1978) to derive a lower limit to the CH_4/H_2 mixing ratio in the atmosphere below the aerosol haze. Compared with the solar value, methane appeared to be over abundant by a factor of three or greater. The optical thickness of the aerosol region was estimated to lie in the range 0.1 to 0.3.

Improved narrow-band (100Å) photoelectric slit scan photometer of Uranus, in the spectral region 6000 - 8500Å, was carried out by Price and Franz (1979). In each waveband of interest, the disk profile was obtained directly from the photometric data by an image restoration technique. Measurements of the point spread function were used to partially remove the effects of atmospheric seeing by means of analytical Fourier-Bessel inversion. Both limb and polar brightening were confirmed to be present within the 7300Å CH_4 band. In addition, weak polar brightening may be present at 6190Å. Surprisingly, however, not all strong CH_4 bands were found to exhibit

limb-brightening. Specifically, the CH_4 bands at 8000Å and 8500Å showed pronounced apparent limb-darkening. Polar brightening may be responsible for the effect. If so, an aerosol haze with a local optical thickness $\sim$0.5 or greater would be required. Visibility of a dense cloud layer located deep in the atmosphere might also cause apparent limb-darkening. If so, the maximum permitted CH_4/H_2 mixing ratio in the visible atmosphere would correspond to $\sim$3 times the solar value. Which explanation is correct remains an open question.

A major limitation of the Price and Franz (1979) restoration technique was the assumption that the Uranus image could be accurately described by the summation of two Gaussian curves. In this paper, our basic restoration theory is modified to handle entirely arbitrary radial distributions of intensity across the Uranus disk. It is then applied to part of the observational data obtained by Price and Franz (1979). Significant polar and limb brightening are confirmed to be present on the Uranus disk within the λ7300Å CH_4 band.

2. NUMERICAL RESTORATION

Our numerical restoration of the Uranus image, though partial removal of both atmospheric and instrumental smear, is based on an extension to the Fourier transform inversion technique developed by Price and Franz (1979). In polar co-ordinate notation, let us define the true intensity distribution over the Uranus disk, $g(r,\theta)$, the point spread function, $f(r,\theta)$, and the observed intensity distribution within the Uranus image, $h(r,\theta)$. Current observational limitations necessitate the adoption of a point spread function which is invariant both in space and in time. Using the notation of Goodman (1968), we can write the Fourier transform convolution theorem in the form

$$H(\rho,\psi) = F(\rho,\psi)\, G(\rho,\psi) \tag{1}$$

where capitalization of the functions indicates their Fourier transforms, and the variables ρ,ψ are polar co-ordinates in the spatial frequency domain.

By adopting circular symmetry both for the Uranus disk and for the point spread function, we can write

$$G(\rho) = H(\rho)/F(\rho) \tag{2}$$

where the two-dimensional Fourier transforms reduce to zeroth order Hankel transforms. In principle, the original distribution, $g(r)$, can be recovered by taking the relevant inverse Hankel transform. Explicitly, we have

$$g(r) = 2\pi \int_0^\infty \rho \, \frac{H(\rho)}{F(\rho)} \, J_0(2\pi r\rho) d\rho \tag{3}$$

where

$$H(\rho) = 2\pi \int_0^\infty r h(r) \, J_0(2\pi r\rho) dr \tag{4}$$

and

$$F(\rho) = 2\pi \int_0^{\infty} r f(r)\, J_0(2\pi r\rho)\, dr \qquad (5)$$

where $J_0(2\pi r\rho)$ is the zeroth order Bessel function.

Naive application of the Fourier transform inversion technique to the Uranus problem gives poor results. Steep gradients in the distribution of intensity over the disk, caused either by high contrast detail or by the limb of the planet itself, are especially difficult to recover. Noise in the photometry, which has a particularly adverse effect on the high spatial frequencies in the image, is at the root of the difficulty. Definition of the amplitudes of the higher frequencies is necessarily quite uncertain. Moreover, the uncertainty is amplified during the process of restoration. Indeed, attempting to restore the very highest spatial frequencies leads to nonsensical results. Due to the ill-conditioned nature of restoration, complete removal of atmospheric and instrumental smear is not feasible. But partial removal, representing a major improvement in spatial resolution of the Uranus disk, can be achieved. Two significant modifications of the basic Fourier transform inversion technique are required.

First, oscillations produced during restoration by the discontinuity at the edge of the planet can be eliminated if the true intensity distribution, $g(r)$, is treated as a perturbation on a uniform disk. Both Uranus and the flat disk are assumed to be of equal angular extent, and to be smeared by identical point spread functions. Using the Fourier transform linearity theorem, together with an obvious subscript notation, we can rewrite equation (3) in the form

$$g_u(r) = g_F(r) + 2\pi \int_0^{\infty} \rho \frac{K(\rho)}{F(\rho)} J_0\,(2\pi r\rho)\, d\rho \qquad (6)$$

where

$$K(\rho) = 2\pi \int_0^\infty r \left\{ h_u(r) - h_F(r) \right\} J_o(2\pi r\rho) dr \qquad (7)$$

and

$$g_F(r) = \begin{cases} 1 \text{ for } r \leq R_u \\ 0 \text{ for } r > R_u \end{cases} \qquad (8)$$

where R_u is the angular radius of Uranus at the time of observation. Both $h_u(r)$ and $h_F(r)$ must be normalized so that

$$2\pi \int_0^\infty r h_u(r) dr = 2\pi \int_0^\infty r h_F(r) dr = \pi R_u^2 . \qquad (9)$$

Smearing of the flat disk is conveniently described by the mathematical statement

$$h_F(r) = g_F(r) \;**\; f(r) \qquad (10)$$

where the double asterisk denotes two-dimensional convolution in signal space.

Second, filtering in the spatial frequency domain is required to optimize the restoration process. By application of a suitable weighting function, the amplitude must be progressively reduced from unity at zero frequency to zero at infinite frequency. But, multiplication in frequency space is equivalent to convolution in signal space. Consequently, the restored image must necessarily contain a residual smear. Suppose we denote the weighting function $S(\rho)$, and its Hankel transform $s(r)$. Making use of the Fourier transform linearity theorem, we can write equation (6) in the form

$$\bar{g}_u(r) = \bar{g}_F(r) + 2\pi \int_0^\infty \rho \, \frac{S(\rho)}{F(\rho)} \, K(\rho) \, J_o(2\pi r\rho) d\rho \qquad (11)$$

where

$$\bar{g}_u(r) = g_u(r) \;**\; s(r) \tag{12}$$

and

$$\bar{g}_F(r) = g_F(r) \;**\; s(r) \tag{13}$$

so that

$$2\pi \int_0^\infty r\bar{g}_F(r)dr = \pi R_u^2 \tag{14}$$

by appropriate normalization of the weighting function $S(\rho)$. Equation (11) will serve as the basis of our restoration technique.

Practical restoration is concerned with the numerical evaluation of the ensemble of functions in equation (11). Making use of the Fourier transform convolution theorem, we can write

$$\bar{g}_F(r) = 2\pi \int_0^\infty \rho\, D(\rho)\, S(\rho)\, J_o(2\pi r\rho)d\rho \tag{15}$$

where the Hankel transform of the uniform disk, $D(\rho)$, is given by

$$D(\rho) = \frac{R_u}{\rho}\; J_1(2\pi\rho R_u) \tag{16}$$

where $J_1(2\pi\rho R_u)$ is the first order Bessel function. Substituting equation (15) into equation (11), we obtain

$$\bar{g}_u(r) = 2\pi \int_0^\infty \rho\, S(\rho)\, W(\rho)\, J_o(2\pi r\rho)\, d\rho \tag{17}$$

where

$$W(\rho) = D(\rho) + \frac{K(\rho)}{F(\rho)} \tag{18}$$

To evaluate the optical transfer function, we adopt the analytical expression for the point spread function given by

$$f(r) = \frac{1}{\pi\left[A_p\sigma_{1p}^2 + B_p\sigma_{2p}^2\right]}\left\{A_p \exp\left[-r^2/\sigma_{1p}^2\right] + B_p \exp\left[-r^2/\sigma_{2p}^2\right]\right\} \tag{19}$$

where the parameters, obtained by Price and Franz (1979), are $A_p = 1$, $B_p = 0.125$, $\sigma_{1p} = 0".763$ arc, and $\sigma_{2p} = 1".569$ arc. The point spread function is illustrated in Figure 1. The corresponding optical transfer function, $F(\rho)$, takes the analytical form

$$F(\rho) = \frac{1}{(A_p\sigma_{1p}^2 + B_p\sigma_{2p}^2)}\left\{A_p\sigma_{1p}^2 \exp\left[-\pi^2\sigma_{1p}^2\rho^2\right] + B_p\sigma_{2p}^2 \exp\left[-\pi^2\sigma_{2p}^2\rho^2\right]\right\} \tag{20}$$

For simplicity, we adopt "Top-Hot" filtering in frequency space such that

$$S(\rho) = \begin{cases} 1 \text{ for } \rho \leq \Omega \\ 0 \text{ for } \rho \leq \Omega \end{cases} \tag{21}$$

where we introduce the "cut-off" frequency Ω. If we adopt an arbitrary maximum restoration factor, M, we may obtain Ω by solving the equation

$$\left[F(\Omega)\right]^{-1} = M \tag{22}$$

Based on equation (21), the residual smear function takes the form

$$s(r) = \frac{\Omega}{r} J_1(2\pi r\Omega). \qquad (23)$$

To evaluate $K(\rho)$, we rewrite equation (7) in the form

$$K(\rho) = H_u(\rho) - H_F(\rho) \qquad (24)$$

where $H_u(\rho)$ and $H_F(\rho)$ are the respective Hankel transforms of the radial distributions of intensity for the Uranus image and for the correspondingly smeared flat disk. Making use of the Fourier transform projection-slice theorem, in the manner discussed by Oppenheim, Frisk, and Martinez (1978), we may rewrite equation (24) in the form

$$K(\rho) = \int_{-\infty}^{+\infty} p_u(x) \exp\left[-2\pi j\rho x\right]dx - \int_{-\infty}^{+\infty} p_F(x) \exp\left[-2\pi j\rho x\right]dx \qquad (25)$$

or

$$K(\rho) = \int_{-\infty}^{+\infty} \left\{p_u(x) - p_F(x)\right\} \exp\left[-2\pi j\rho x\right]dx \qquad (26)$$

where $p_u(x)$ and $p_F(x)$ are the respective one-dimensional projections of the Uranus disk and of the correspondingly smeared flat disk.

The Uranus slit scan at 7300Å, published by Price and Franz (1979), was used to derive $p_u(x)$. An iterative Bayesian estimation technique developed by Lucy (1974), was used to simultaneously remove slit broadening and high frequency noise. A maximum of three iterations provided the optimum Bayesian solution. The resultant Uranus projection, $p_u(x)$, is shown in Figure 2. The flat disk projection, $p_F(x)$, was calculated by the technique developed by Price and Franz (1978). Both one-dimensional projections were sampled at an interval of 0.032"arc, giving 30 points per second of arc.

Written in the form of a discrete Fourier transform, equation (26) can be readily evaluated by the Cooley-Tukey (1965) algorithm. We used a 512 point Fast Fourier Transform (FFT). Numerical evaluation of the integral in equation (11) required information concerning the behavior of $K(\rho)$ between the FFT values computed for discrete spatial frequencies. Interpolation was carried out by means of the sampling theorem, for a band limited function, given by

$$K(\rho) = \frac{1}{2T} \sum_{n=-\infty}^{+\infty} K\left(\frac{n}{2T}\right) \sin \frac{[2\pi T(\rho - n/2T)]}{\pi[\rho - n/2T]} \qquad (27)$$

where 2T is the band width in signal space. The summation was carried out over all discrete values of the FFT.

4. RESULTS

Four restorations of the Uranus image are illustrated in Figure 3. Each example corresponds to a selected maximum restoration factor in the range $25 \leq M \leq 100$. Restoration factors greater than 100 lead to unstable solutions due to the enhancement of residual photometric noise ($\sim$1 percent) in the Uranus line projection. Residual smear functions, corresponding to each restoration, are shown in Figure 4. For comparison purposes, uniform disks convolved with each residual smear function are also shown in Figure 3.

Although extraneous ripple in the restored profiles, beyond the edge of the planet, suggests that the solution is becomming unstable for maximum restoration factors greater than 75, there is no doubt that significant polar- and limb-brightening are present on the Uranus disk at 7300Å. If polar brightening were absent, the center-to-limb intensity ratio might reach 1:4, the maximum values discussed by Price and Franz (1978). Evidently, more detailed study of the Uranus profile in this waveband requires the separation of the polar and limb brightening phenomena.

Spatial resolution within the restored profiles can be defined in a manner analogous to the Rayleigh limit in optical systems. Specifically, the resolution can be taken equal to the radius of the first zero of the residual smear function. If we adopt a maximum restoration factor of 75, the corresponding spatial resolution is 0." 72 arc. Since the point spread function has a half 1/e-width $\sim$0".8, we have obtained an improvement in resolution of at least a factor of two.

ACKNOWLEDGMENTS

Special thanks go to J. Zelenka for valuable discussions during the course of the analysis. This research was supported by the National Aeronautics and Space Administration under contract NASW-3134 and grant NGR-03-003-001.

REFERENCES

Avis, C.A., Smith, H.J., Bergstralh, J.T., and Sandmann, W.H. (1977), "Photometric Determination of the Rotation Period of Uranus," Paper presented at the Eighth Annual Meeting of the American Astronomical Society, Division for Planetary Sciences, Honolulu, Hawaii, 1977 January 19-22.

Cooley, J.W. and Tukey, J.W. (1965), "An Algorithm for the Machine Calculation of Complex Fourier Series," Math. of Computation 19, 297-301.

Franz, O.G. and Price, M.J. (1977), "Uranus: Limb and Polar Brightening at λ7300A," Astrophys. J. 214, L145-L146.

Goodman, J.W. (1968), "Introduction to Fourier Optics," McGraw-Hill, New York.

Lucy, L.B. (1974), "An Iterative Technique for the Rectification of Observed Distributions," Astron. J. 79, 745-754.

Oppenheim, A.V., Frisk, G.V., and Martinez, D.R. (1978), "An Algorithm for the Numerical Evaluation of the Hankel Transform," Proc. IEEE 66, 264-265.

Price, M.J. (1978), "Limb Brightening on Uranus: An Interpretation of the λ7300A Methane Band, Icarus (in press).

Price, M.J. and Franz, O.G. (1976), "Limb Brightening on Uranus: The Visibl Spectrum," Icarus 29, 125-136.

Price, M.J. and Franz, O.G. (1978), "Limb Brightening on Uranus: The Visible Spectrum, II," Icarus 34, 355-373.

Price, M.J. and Franz, O.G. (1979), "Uranus: Narrow-Waveband Disk Profiles in the Spectral Region 6000 - 8500 Angstroms," Icarus (in press).

Sinton, W.M. (1972), "Limb and Polar Brightening of Uranus at 8870Å," Astrophys. J. 176, L131-L133.

Smith, B.A. (1977), "Uranus Photography in the 890-nm Absorption Band of Methane," Paper presented at the Eighth Annual Meeting of the American Astronomical Society, Division for Planetary Sciences, Honolulu, Hawaii, 1977 January 19-22.

Westphal, J.A. (1972), Comment at the Third Annual Meeting of the American Astronomical Society, Division for Planetary Sciences, Kona, Hawaii, 1972 March 21-24.

FIGURE CAPTIONS

Figure 1. The Point Spread Function. Radial intensity is plotted as a function of angular distance from the center of the image. Intensities are normalized at the center of the image.

Figure 2. The Uranus image line-projection, $p_U(x)$, at 7300Å. Relative intensities, in arbitrary units, are plotted as a function of angular distance from the center of the image.

Figure 3. Restorations of the Uranus image. Within each panel, the solid curve illustrates the radial intensity distribution of the Uranus disk for a selected maximum restoration factor M. The broken curve illustrates the radial distribution of intensity for a flat disk subjected to the corresponding residual smear function.

Figure 4. Residual smear functions appropriate for selected maximum restoration factors, M.

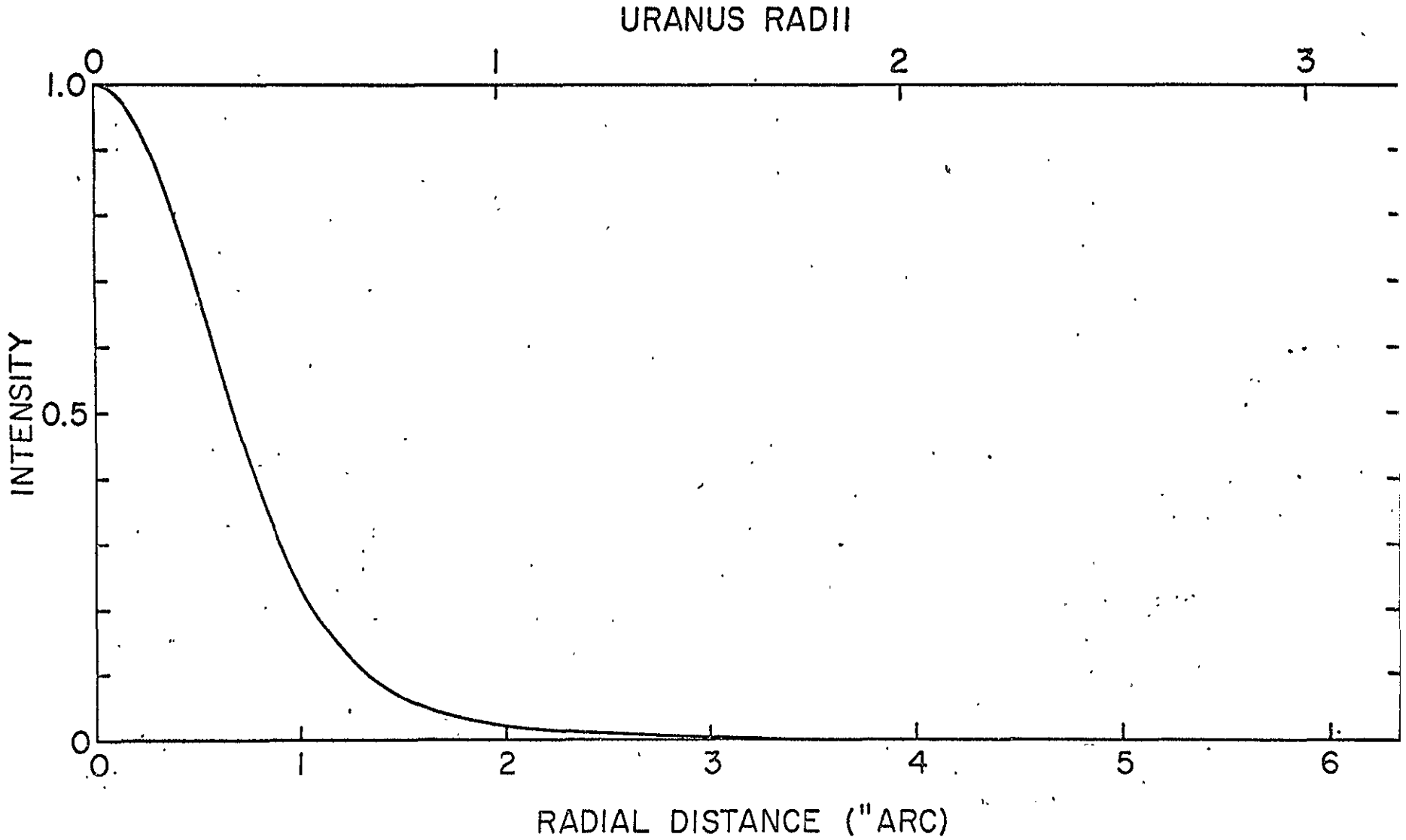
URANUS RADII
0
1
2
3
1.0
0.5
0
INTENSITY
0
1
2
3
4
5
6
RADIAL DISTANCE ("ARC)

Fig. 1

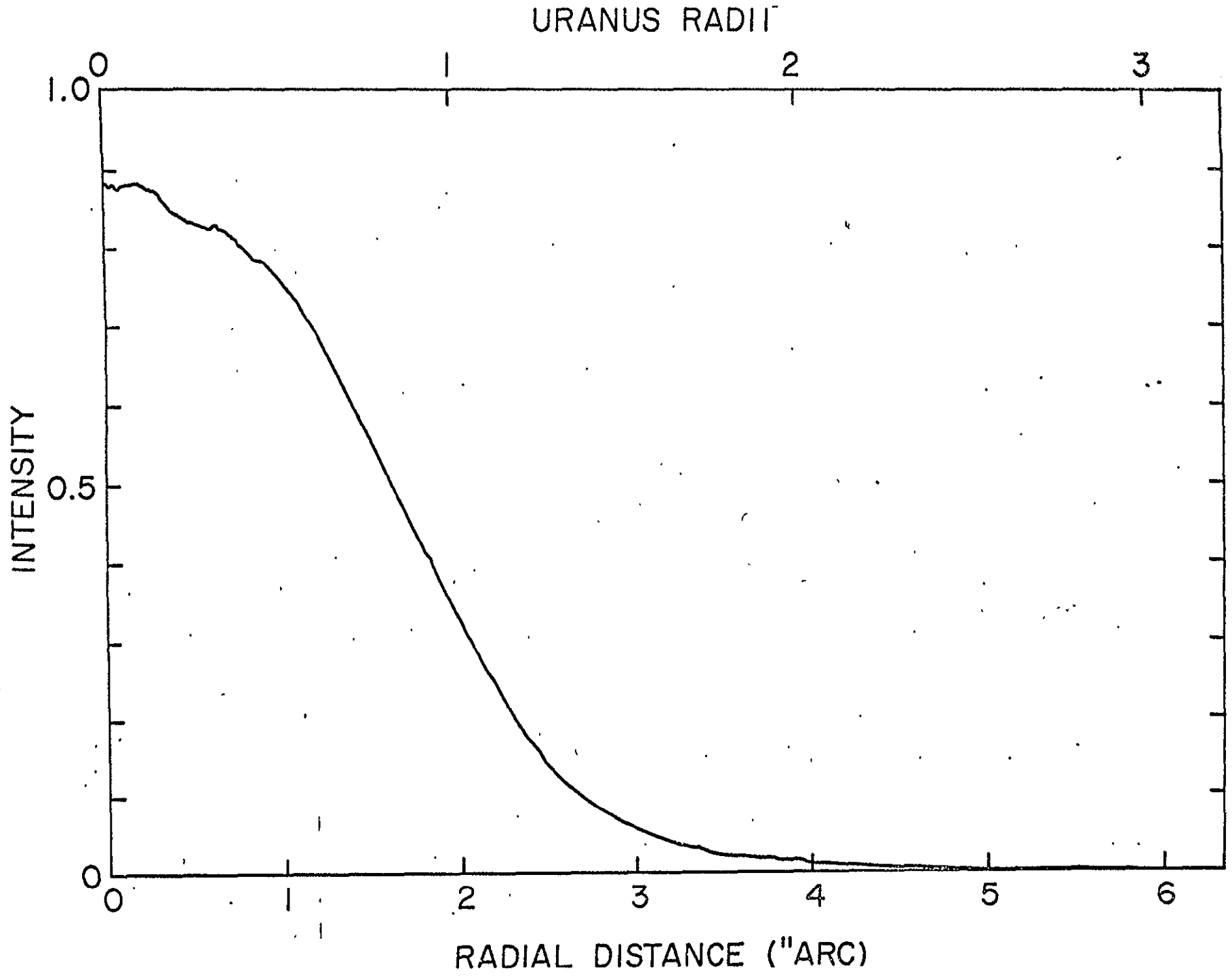
URANUS RADII
0
1
2
3
1.0
0.5
0
INTENSITY
0
1
2
3
4
5
6
RADIAL DISTANCE ("ARC)

Fig. 2

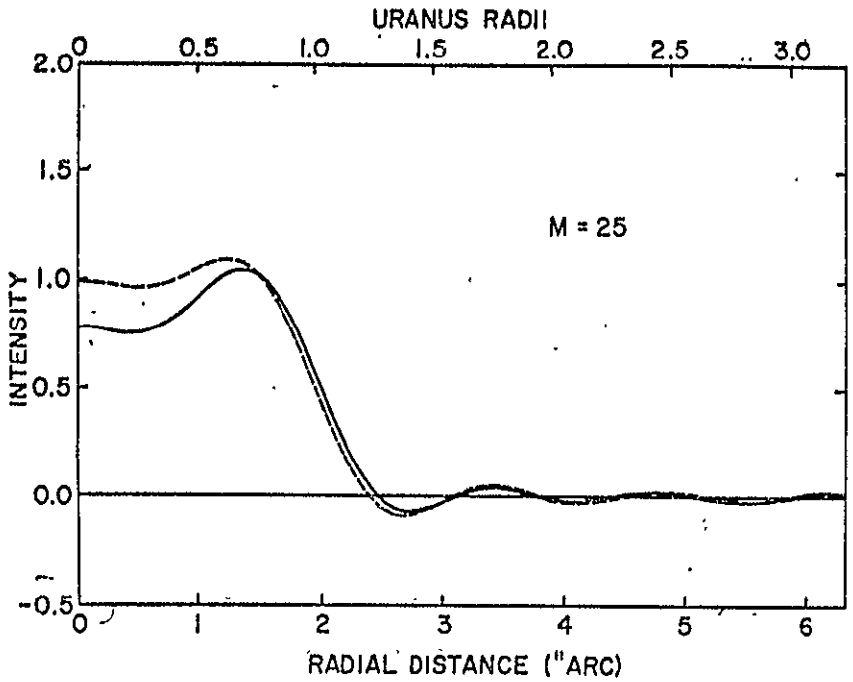
URANUS RADII
0
0.5
1.0
1.5
2.0
2.5
3.0
M = 25
INTENSITY
2.0
1.5
1.0
0.5
0.0
-0.5
0
1
2
3
4
5
6
RADIAL DISTANCE ("ARC)

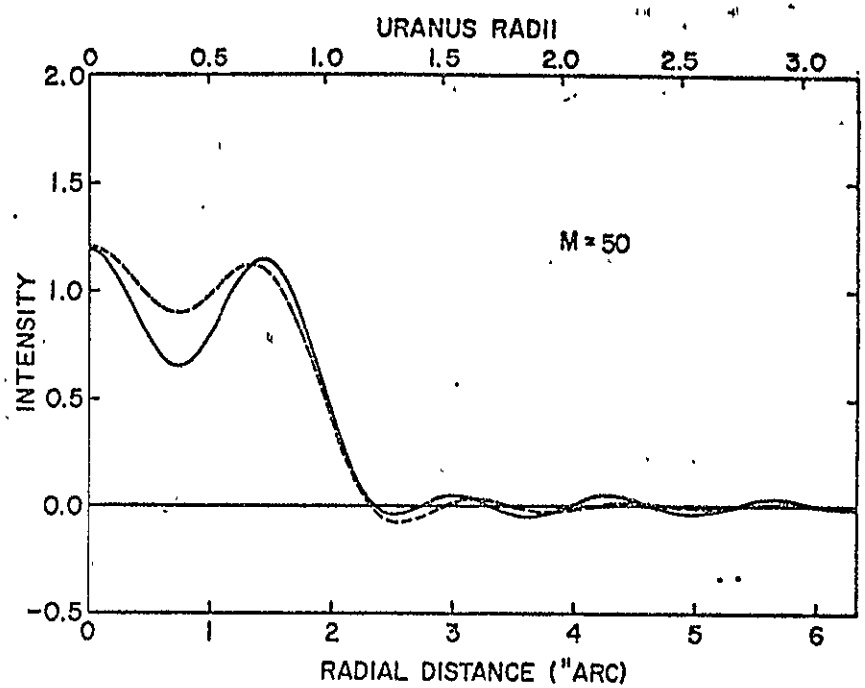
URANUS RADII
0
0.5
1.0
1.5
2.0
2.5
3.0
M = 50
INTENSITY
2.0
1.5
1.0
0.5
0.0
-0.5
0
1
2
3
4
5
6
RADIAL DISTANCE ("ARC)

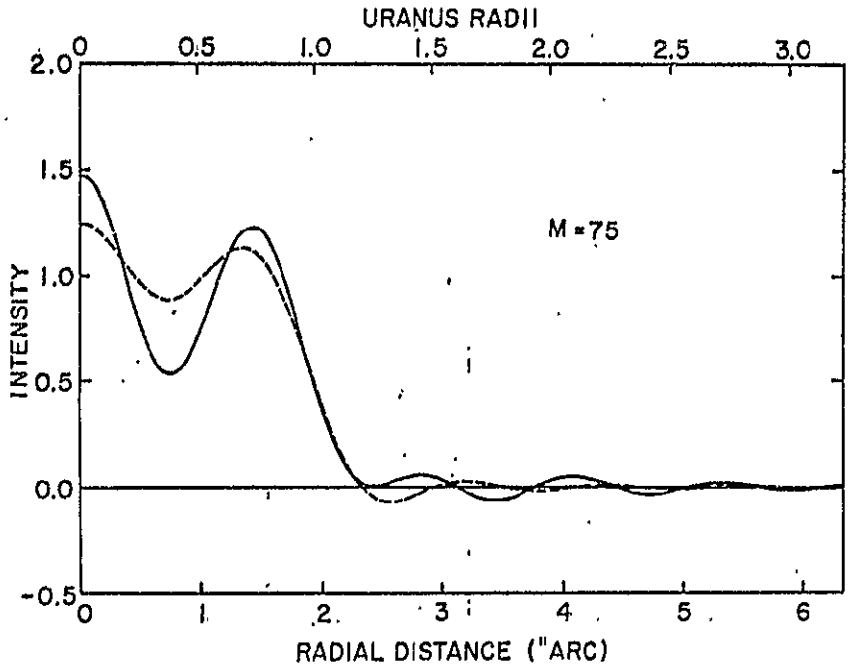
URANUS RADII
0
0.5
1.0
1.5
2.0
2.5
3.0
M = 75
INTENSITY
2.0
1.5
1.0
0.5
0.0
-0.5
0
1
2
3
4
5
6
RADIAL DISTANCE ("ARC)

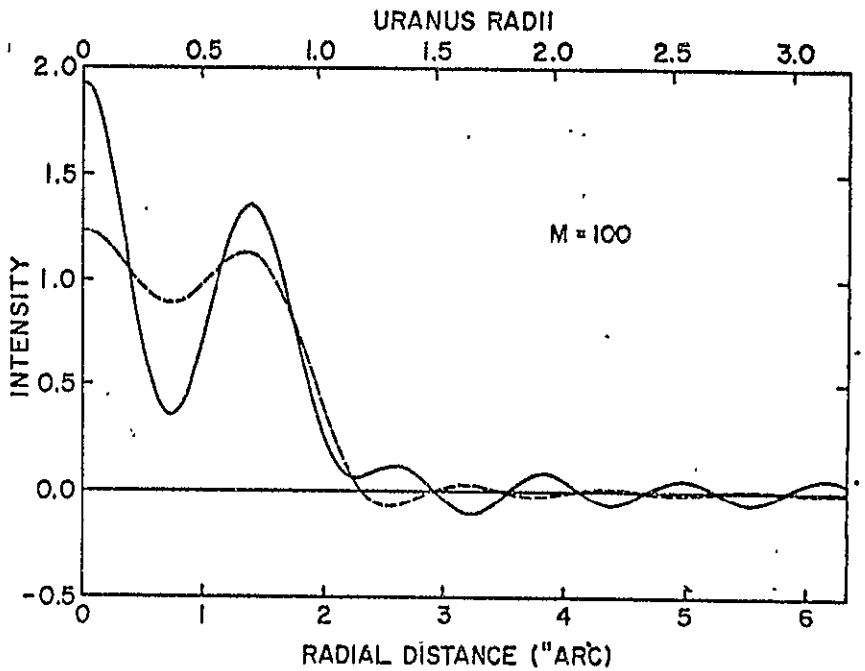
URANUS RADII
0
0.5
1.0
1.5
2.0
2.5
3.0
M = 100
INTENSITY
2.0
1.5
1.0
0.5
0.0
-0.5
0
1
2
3
4
5
6
RADIAL DISTANCE ("ARC)

Fig. 3

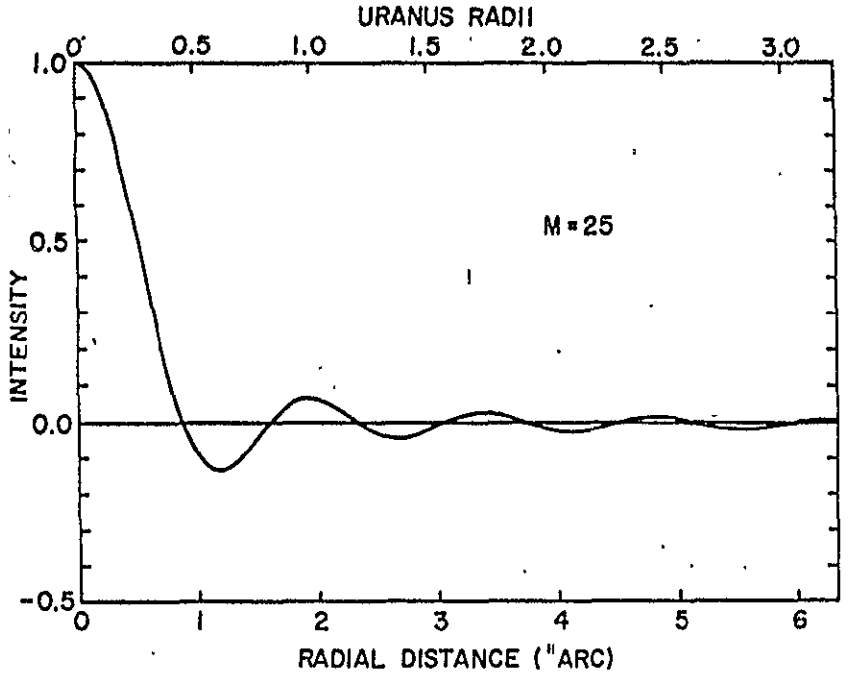
URANUS RADII
0
0.5
1.0
1.5
2.0
2.5
3.0
1.0
0.5
0.0
-0.5
INTENSITY
M = 25
0
1
2
3
4
5
6
RADIAL DISTANCE ("ARC)

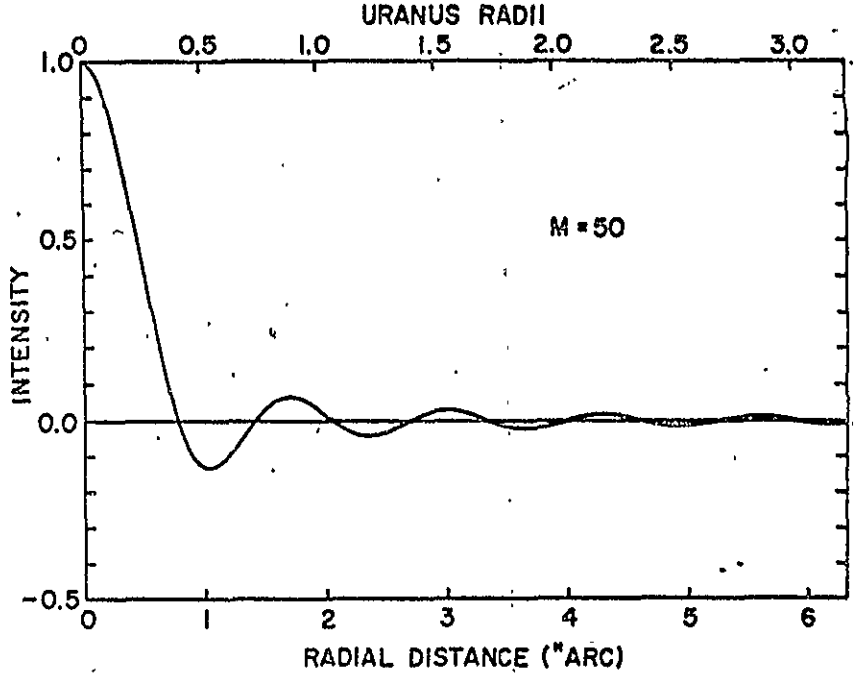
URANUS RADII
0
0.5
1.0
1.5
2.0
2.5
3.0
1.0
0.5
0.0
-0.5
INTENSITY
M = 50
0
1
2
3
4
5
6
RADIAL DISTANCE ("ARC)

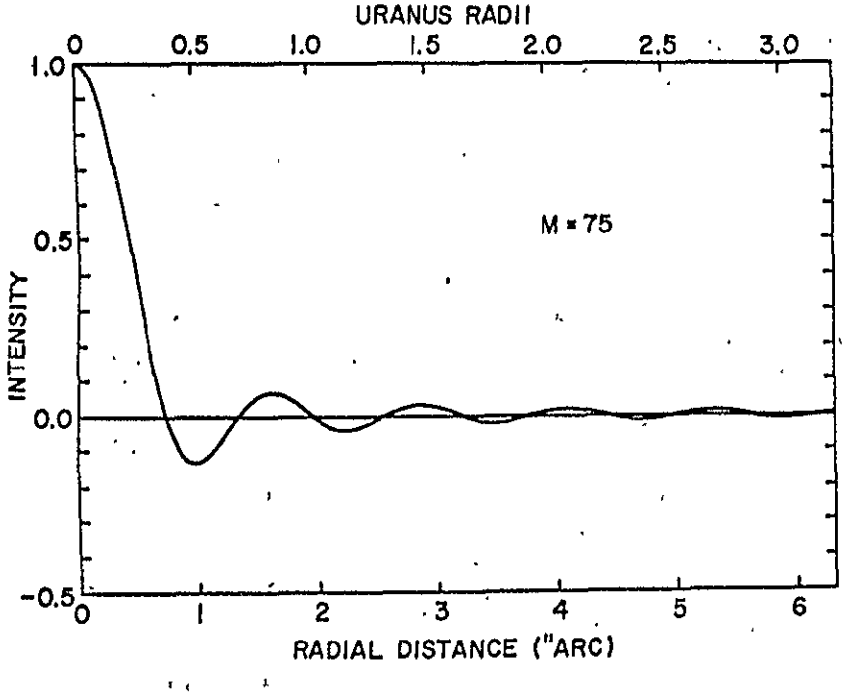
URANUS RADII
0
0.5
1.0
1.5
2.0
2.5
3.0
1.0
0.5
0.0
-0.5
INTENSITY
M = 75
0
1
2
3
4
5
6
RADIAL DISTANCE ("ARC)

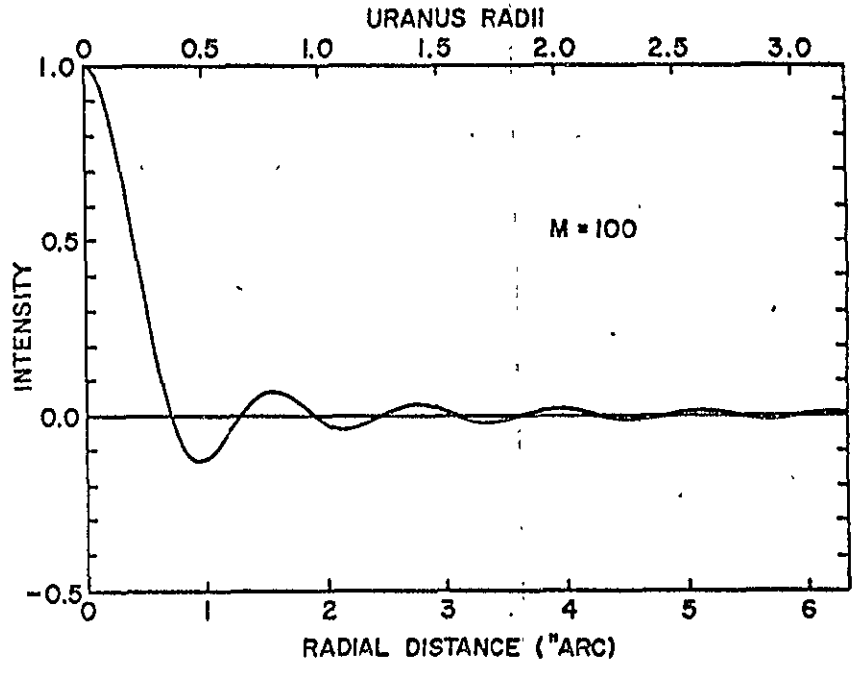
URANUS RADII
0
0.5
1.0
1.5
2.0
2.5
3.0
1.0
0.5
0.0
-0.5
INTENSITY
M = 100
0
1
2
3
4
5
6
RADIAL DISTANCE ("ARC)

Fig. 4